Topology Optimization of Multifunctional Nanocomposite Structures

David Ryan Seifert

Dissertation submitted to the Faculty of the
Virginia Polytechnic Institute and State University
in partial fulfillment of the requirements for the degree of

Doctor of Philosophy
in
Aerospace Engineering

Mayuresh J. Patil, Chair
Gary D. Seidel, Co-Chair
Robert A. Canfield
Gregory W. Reich

October 24th, 2018
Blacksburg, Virginia

Keywords: Topology Optimization, Carbon Nanotubes, Multifunctional Materials, Micromechanics

Topology Optimization of Multifunctional Nanocomposite Structures

David Ryan Seifert

ABSTRACT

This dissertation presents the design of multifunctional structures through the optimal placement of nanomaterial additives. Varying the concentration of Carbon Nanotubes (CNTs) in a polymer matrix affects its local effective properties, including mechanical stiffness, electrical conductivity, and piezoresistivity. These local properties in turn drive global multifunctional performance objectives. A topology optimization algorithm determines the optimal distribution of CNTs within an epoxy matrix in an effort to design a set of structures that are capable of performing some combination of mechanical, electrical, or peizoresistive functions. A Pareto-Based Restart Method is introduced and may be used within a multi-start gradient based optimization to obtain well defined multiobjective Pareto Fronts. A linear design variable filter is used to limit the influence of checkerboarding. The algorithm is presented and applied to the design of beam cross-sections and 2D plane stress structures. It is shown that tailoring the location of even a small amount of CNT (as low as 2 percent and as high as 10 percent, by volume) can have significant impact on stiffness, electrical conductivity, and strain-sensing performance. Stiffness is maximized by placing high concentrations of CNT in locations that either maximize the bending rigidity or minimize stress concentrations. Electrical conductivity is maximized by the formation of highly conductive paths between electrodes. Strain-sensing is maximized via location of percolation volume fractions of CNTs in high strain areas, manipulation of the strain field to increase the strain magnitude in these areas, and by avoiding negative contributions of piezoresistivity from areas with differing net signed strains. It is shown that the location of the electrodes can affect sensing performance. A surrogate model for simultaneous optimization of electrode and topology is introduced and used to optimize a 2D plane stress structure. This results in a significant increase in sensing performance when compared to the fixed-electrode topology optimization.

That this work received support from the Air Force Research Laboratory (AFRL) under agreement number FA8650-09-2-3938.

Topology Optimization of Multifunctional Nanocomposite Structures

David Ryan Seifert

GENERAL AUDIENCE ABSTRACT

This dissertation presents a method that allows for the best placement of a limited amount of filler material within a base matrix material to form an optimal composite structure. Adding filler material, in this case Carbon Nanotubes, can change the effective behavior of the composite structure, enhancing the capabilities of the base matrix material by adding structural stiffness, electrical conductivity, and even the ability for the structure to measure its own strains. The degree to which these changes occur is dependent on the amount of filler material present in any given subsection of the structure. The method then is focused on determining how much of the filler to place in different subsections of the structure to maximize several measures of performance. These measures pertain to structural performance, electrical conductivity, and the structure's ability to sense strains. Steps are taken within the method to remove non-physical designs and also to find the overall best design, called the global minima. The method is applied to several test structures of varying complexity, and it is shown that the optimization method can heavily influence performance by tailoring the filler material distribution. Further electrical and sensing performance gains can be obtained by properly selecting where the electrodes are located on the structure. This is demonstrated by including electrode placement in the design method along with the filler distribution.

Acknowledgments

I would first like to thank Dr. Patil and Dr. Seidel for their unending support of this work. It is rare that a student is lucky enough to have one advisor of their quality. I had two. I would specifically like to acknowledge Dr. Patil's mastery of sensitivity analysis and finite elements, for without his insight this project would not have reached the level it is at now. Dr. Seidel's knowledge of micromechanics and multifunctional materials was also invaluable, for he was always able to gauge whether the optimization algorithm was producing sensible designs, and his intuition about which behaviors were optimal was often proven correct.

I'd also like to thank my committee members, Dr. Canfield and Dr. Reich. Dr. Canfield, for allowing me to take pretty much every optimization course he offered during my time at Virginia Tech, and Dr. Reich for his continued insight throughout the crucial developmental stages of this research. I'd also like to thank Dr. Reich and AFRL as a whole for funding this project.

Thanks to Virginia Tech as well. The Virginia Tech Aerospace Department has been more than accommodating in allowing me to complete the latter parts of this degree remotely as I tried to find my way, first at Orbital ATK and now contracting through AFRL. I'd also like to take the time now to thank both of those institutions for letting me work while pursuing a degree.

Though I have not lived in Blacksburg for several years now, I cannot think of another place that I call home. Thanks to all of my friends, some of which are still there. You all have kept me sane-ish. And thanks to my family, for doing the same in their own special way. And for raising me as a Hokie. There is a Saturday night sometime in all our futures. Sandman is playing, and we're all jumping together.

And finally, thanks to Laura. There were some times, that I suspect are unavoidable in this sort of work, when I thought that everything was wrong and broken. Laura is the one that held all the pieces together and kept me whole. I am eternally grateful for her love and understanding.

Contents

List of Figures

List of Tables

Chapter 1

Introduction

The future of structural design is evolving. Classically, a system such as an aircraft wing is comprised of several subsystems e.g. load-bearing structures, electronics, and controls. Each such subsystem can be designed to handle one of these tasks individually. Recently, the rise in multifunctional materials is allowing for integration of subsystems, potentially reducing both part count and system weight while introducing novel capabilities. One way these new capabilities may be obtained is by adding a multifunctional filler to a matrix phase, forming a multifunctional composite. Of these fillers, Carbon Nanotubes (CNTs) are some of the most promising for their beneficial mechanical, electrical, and piezoresistive properties. CNT based composite sensors have been shown to offer several advantages over classical strain gauges; including better performance in detecting small scale phenomena, and usability in through-cross-section, or embedded sensing. While multifunctional systems offer great benefit they also involve coupled and competing behaviors. It becomes necessary to rely on advanced models and design algorithms to determine the optimal distribution of the filler within the matrix phase that will result in the best performing structure.

Additionally, the structural design space has often been limited by manufacturing processes. In turn this meant that conventional optimizations in shape and sizing were limited to design variables such as flange thickness, beam length, cutout shape, or number of trusses as those were the variables which machining processes allowed them to control. But the current additive manufacturing boom is quickly expanding the realizable design space. The ability to produce more organic shapes, use multiple materials, and finely control material distribution are all advantages of new manufacturing processes. Additive manufacturing (AM) has reached a point where adding specific amounts of a nanomaterial into an advanced, highly tailored composite topology is not just a concept, but a physically realizable solution to a multifunctional design problem.

This combined materials and manufacturing revolution is perhaps one of the driving factors behind the resurgence of topology optimization as a design tool. The comparative freedom the method offers in designing the layout of a structure can often lead to better performing,

novel designs. Now, more than ever, the complex design solutions that result from topology optimization are realizable. Topology optimization has blossomed as a field to cover designs of up to a billion variables, across multiple materials and functionalities, and on length scales ranging from the microscale to the size of entire aircraft [1].

The research presented here combines all of this new technology into a cohesive design tool. It proposes a topology optimization algorithm that may be used to determine the optimal placement of CNTs within a matrix in order to simultaneously optimize multiple performance objectives. Micromechnanics models are used to relate local volume fractions of CNTs to local mechanical, electrical, and piezoresistive properties. These volume fractions are allowed to vary from element to element within a discretized finite grid, as if an AM printer were capable of mixing different volume fractions in each voxel of the design. Analytic sensitivities are used to determine how changes in the local CNT volume fractions will affect the global objectives. Gradient based optimization is used to produce Pareto Fronts of nondominated points that show the best attainable multiobjective performance. Each Pareto point has an associated topology. Examining the trends in these topologies will help explain why one layout of CNT may be particularly well equipped for a given performance objective, while another may maximize a second objective, and others still may offer some compromise between the two. The core concept is that this algorithm is a tool which answers the question, "What is the best possible performance of objective X for a design that also has suitable performance in objective Y, and what topology needs to be manufactured to obtain these values?"

The rest of the dissertation is outlined as follows: In Chapter 2, the literature survey details advances in both nanocomposite modeling and multifunctional topology optimization. There are several different ways to obtain effective composite properties of a CNT-epoxy composite, and the section investigates these methods and comments on which of them are best suited for use within a gradient-based optimization routine. The topology optimization section discusses advances from the original SIMP [2] methodology to the current state-of-the-art, which can handle large problems with multiple objective functions and multiple materials. The chapter concludes with the statement that there is still unexplored territory in the optimization of a distributed nanocomposite system for multiple coupled objectives.

Chapter 3 introduces topology optimization in a general form and then specifies the optimization problem that is to be solved in the later chapters; optimizing the distribution of a limited amount of CNTs in order to maximize some combination of mechanical stiffness, electrical conductivity, or piezoresistive strain sensing. Sections in this chapter detail specific methods used to handle optimization of problems with many minima and problems with the numerical instability known as checkerboarding, both of which can occur in topology optimization.

The method is then applied to the optimization of a nanocomposite beam cross-section in Chapter 4. The cross-section is subject to either prescribed twist or prescribed bending and electrodes are placed along the boundary. The cross-section is discretized into a finite element

grid and each element is given a unique variable that controls the local CNT volume fraction. Equations are introduced to compute torsional rigidity, bending strain energy, electrical conductivity, and resistance change due to strain. Sensitivities of these four objectives with respect to changes in the local volume fractions are derived. Results are presented showing optimal topologies and performance for two separate design problems. A trade study is performed across multiple volume fraction constraints and electrostatic boundary conditions. It is shown that the volume fraction constraint is restrictive on stiffness performance, but the electrode boundary condition is more limiting for sensing performance.

Following the beam cross-section results, the Chapter 5 extends the algorithm to a 2D plane stress structure. Micromechanics are updated from the previous chapters to account for the additional strain terms that affect the piezoresistivity. A mechanical finite element model is coupled with the electrostatics finite element model to solve the multifunctional problem. A coupled adjoint sensitivity method is used to obtain sensitivity of the strain-sensing objective for the 2D structures. Two structures are considered: a plate with a hole and a compact tension sample. Trades are again performed on the global volume fraction constraint, and the resulting set of Pareto Fronts compare stiffness and sensing performance alongside the optimized topologies.

During the cross-section optimization process it was discovered that the boundary electrode location could play an important role in the sensing performance, and also to help remove some of the competing nature of the stiffness and sensing objectives. Chapter 6 introduces a quadratic surrogate model for mixed material distribution-boundary condition optimization, and applies the model to the simultaneous design of the topology and boundary electrode location. The surrogate model is validated by comparing it to a refined mesh evaluated at nodal values. An algorithm trade study is performed to select the best optimization algorithm for use in the surrogate optimization. The plate with a hole structure is reintroduced, now with a variable electrode that is optimized alongside the topology. The same trade across volume fraction constraints is repeated, and the optimal performance and topologies are compared to the fixed electrode case. A noticeable improvement in sensing performance is seen due to cooperative behavior between the topology and the electrode.

The final chapter summarizes the research, offers concluding remarks, and mentions possible extensions. Following the bibliogrpahy, Appendix A offers a more comprehensive summary of the surrogate model validation.

Chapter 2

Literature Survey

The implementation of a multifunctional nanocomposite topology optimization algorithm requires first creating a model that can relate design variables, in this case volume fractions of CNT, to properties such as mechanical stiffness, electrical conductivity, and piezoresistive constant. Much work has been done to characterize how changing CNT volume fractions may alter a composite's effective properties, and some of the relevant models are examined in this chapter. The selected model must be for the appropriate length scale and balance accuracy with computational cost, as it will be used to solve for local properties within a mesh that may contain thousands to millions of local elements. It is also important that the model be differentiable so that analytic sensitivities of the local properties with respect to changes in CNT volume fraction, which are needed for the analytic sensitivities objective functions, may be obtained.

Topology optimization has been used to solve material layout problems for the past three decades. Various methods of topology optimization have been developed, and some applications to multiple/multifunctional materials in optimization are considered in this chapter. The method used in this dissertation is a form of density-method topology optimization that traces its roots to the homogenization methods developed in the late 1980's. This method is well suited for the problem of a distributed material system, and it will be shown that there is currently work being done to couple topology optimization, multifunctional materials, and additive manufacturing. The field is active, quickly evolving, and with much promise of future applications.

2.1 Modeling of Carbon Nanotube Composites

Of the myriad multifunctional materials carbon nanotubes, (CNTs) have been a source of much interest since Iijima first introduced them in the early 1990's [3, 4]. They consist of single or multiple sheets of carbon atoms rolled into tubes which have diameters on

the nanoscale [5]. CNTs possess many desirable properties, including stiffness that can measure over 300 GPa [6, 7], high electrical and thermal conductivity [8, 9], and a measurable piezoresistive effect, which relates strain to resistance change [10, 11, 12, 13]. CNT-based sensors or sensing structures offer some benefits over conventional strain gage sensors [14]. The strain gage is a unidirectional strain sensor, it has poor detection at the nanoscale, and it also cannot easily be embedded in the structure to monitor internal strains or damage. All of these drawbacks may be overcome with the use of CNTs.

The properties of CNTs motivate their use as a filler within a composite. There have been CNT composites fabricated with ceramics [15, 16], metals [17, 18], and polymers [12, 19, 20]. The addition of nanotubes in polymers has been shown in experiments to increase Young's modulus and fracture toughness [21, 22], increase electrical conductivity [21, 23], and introduce a piezoresistive strain sensing effect [22, 12]. These experiments also showed that varying the volume fraction of the CNTs can help modulate the effective composite properties.

As the potential benefits of CNTs emerged over time, it became important to develop models that could predict the performance of composites that use CNTs as a filler. These models vary in fidelity and scale. Length scales range from several atoms (using quantum mechanics models) [24, 25], to several nanometers (molecular dynamics models) [26], to micron or larger (micromechanics) [27, 28, 10], to the macroscale (continuum, finite element) [29]. Within the proposed topology optimization framework it is beneficial to work with micromechanics models. A macroscale structure is to be optimized, and it is optimized by locally changing the microscale composition. See Figure 2.1. Notice that two different subsections of the macroscale may have two different material compositions, each of which will have local effective properties governed by micromechancis models.

Micromechanics models such as Voigt/Reuss, also known as Rule of Mixtures and Inverse Rule of Mixtures, provide simple and straightforward weighted-average equations. These relate the volume fraction of the phases present in the composite and their respective properties to the effective composite property [30, 31]. Together, these two models form upper and lower bounds on an effective property for a given composition of the phases. Hashin and Shtrikman were able to refine these bounds for a two-phase system and arrive at the tightest possible range for effective moduli in the composite, aptly called the Hashin-Shtrikman bounds [32].

More complex models include Eshelby methods, of which the Self-Consistent and Mori-Tanaka methods are the most prevalent [33, 34, 35, 36]. The Eshelby solution considers an inclusion within an elastic medium, and the resulting changes of the mechanical states of both the inclusion and the medium should the inclusion change shape [33, 34]. The Mori-Tanaka and Self-Consistent methods both use this concept, and vary their definition of the inclusion [35, 37].

Applying micromechanics specifically to the CNT-Epoxy composite, Kim, Mirza, and Song developed Mori-Tanaka and Halpin-Tsai (a version of self-consistent method) equations for

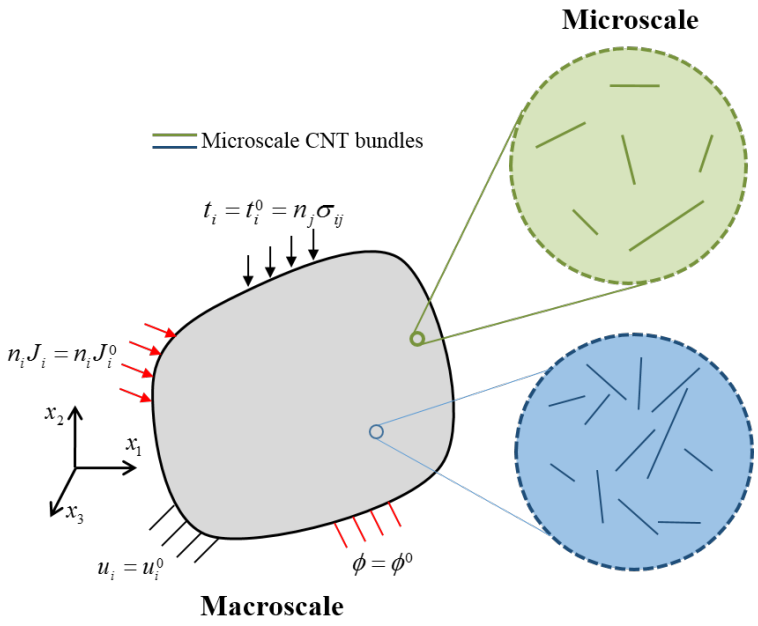

Figure 2.1: General design space illustrating different length scales and varying microstructures.

CNTs [38] and showed for low volume fractions (up to 10 percent CNT) there is a nearly linearly increasing relationship between CNT volume fraction and stiffness properties, such as axial modulus in aligned CNT composites. This behavior has also been shown using a composite cylinders micromechanics method [27].

Ren and Seidel [39] also modeled microscale representative volume elements (RVEs) of CNT-Polymer composites and included both electron tunneling effects and inherent CNT piezoresistivity in order to model changes in both electrical conductivity and piezoresistivity. These models showed that before a percolation volume fraction of CNT is achieved there is little change in the effective electrical properties. At percolation there begins a nonlinear decrease in resistivity, while there is a sharp increase in piezoresisivity. This percolation threshold is seen both in the model and in experiments [12] to be the volume fraction with the highest piezoresistivity. Adding more CNT beyond the percolation value continues to increase conductivity, but decreases piezoresistivity.

It is important to note that Voigt/Reuss, Hashin-Shtrikman, and Eshelby/Mori-Tanaka methods are continuous equations that relate an effective property of the composite to the properties of the phases and are also differentiable with respect to phase volume fraction. Specifically, within the context of this dissertation, these equations can relate volume fractions of the CNT to effective composite stiffness, electrical resistivity, and piezoresistivity. This allows for the incorporation of the micromechanics models into a continuous, gradient based optimization routine in which local volume fractions may change from element to el-

ement, similar to Figure 2.1. The use of micromechanics models in topology optimization is not entirely novel. Even the seminal textbook on topology optimization by Sigmund and Bendsoe [2] suggests the use of Hashin-Shtrikman bounds as an interpolation scheme in a density-based topology method. It is the extension of these ideas into systems that are both multimaterial and multifunctional for which literature is somewhat lacking.

2.2 Multiobjective Topology Optimization

Introduced by Bendsoe and Kikuchi in 1988, topology optimization is a 'design by material distribution' approach [40]. It differs from both shape and sizing optimization. Shape optimization may parameterize features of a structure, such as the shape of cutouts within a frame, then optimize those shapes [41]. Sizing optimization may seek to determine the thickness, length, radius, or other geometric parameters of structural members [42]. Topology optimization instead discretizes the design domain, often via the use of finite elements, and then asks the question, "where does one place material within the domain to optimize performance?" [2, 43]. This opens up the design space when compared to shape and sizing optimization, but comes with a drawback in that topology problems typically contain large numbers of design variables and result in more organic, nonconventional results. This complicated design space has higher potential for multiple minima and or/flat regions that are insensitive to the design variables [44]. Figure 2.2 differentiates between shape, sizing, and topology optimization.

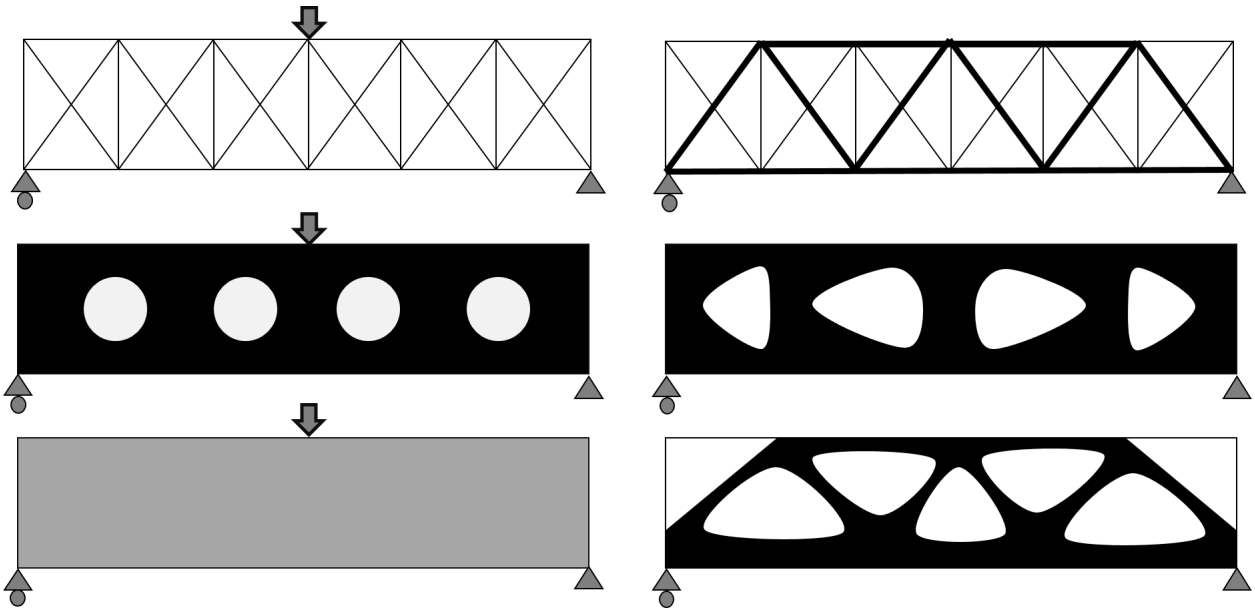

Figure 2.2: a) Sizing optimization b) Shape optimization and c) Topology optimization. Figure modeled after work in [2].

Early efforts in topology optimization involved using pseudo-density methods, such as SIMP (Solid Isotropic Material with Penalization) [2, 45], to minimize structural compliance. These methods assigned artificial density variables to each element within a mesh, and then used gradient based optimization methods, such as optimality criteria [46, 47], method of moving asymptotes [48], and sequential quadratic programming [49, 50] to drive the density variables to an on/off design. When converged, each element would either have a design variable value of "1", meaning there was material in that element, or a "0", meaning a void. In practice these designs often contained elements with intermediate densities, requiring post-processing. The solutions were also shown to be sensitive to initial conditions and susceptible to numerical exploits in the mesh that may lead to unrealistic designs [44, 51].

However, the potential of topology optimization to discover novel structural archetypes was recognized. A paper published by Sigmund in 2001 presented a 99 line Matlab code for compliance minimization via the SIMP method that functioned as an example of what the method could achieve [52]. As computational power advanced topology optimization algorithms went from solving representative Mitchell-truss problems [53] with a few hundred elements to entire aircraft wings with over a billion elements [1].

Topology optimization has expanded to cover a massive range of problems, including multiple materials, multiple objective functions, and multiple length scales. Several comprehensive reviews of topology optimization are available. Deaton and Grandhi cover the advancement of Topology Optimization in the 21st century, with a focus on the various types of topology optimization that have emerged (of which the SIMP-based density methods is one) [54]. Similarly, Sigmund and Maute published a comprehensive summary in 2013 [55]. The same year, Paulino presented that over 22 countries were publishing papers in topology optimization, with their focuses ranging from multiphysics, to nondeterministic solutions including manufacturing constraints, to microstructure optimization of fluid-structure cells, to even art and architecture [56].

This dissertation focuses on the subset of topology optimization that involves multifunctional materials. Sigmund and Torquato [57] used multi-phase topology optimization to design two-material structures with extreme thermoelastic coefficients given constraints on volume fractions of each phase. This behavior came at the cost of a low bulk modulus, reinforcing the need for a multiobjective optimization routine to design a structure with appropriate bulk stiffness that still maximizes thermoelastic performance. Stanford et. al [58] optimized a carbon fiber reinforced latex wing for a coupled aeroelastic response. These wings were then manufactured and tested, and it was found that even with a low fidelity aeroelastic model the optimization was able to improve upon aerodynamic performance. Kruijf [59] optimized a beam-like structure for maximum stiffness and thermal conductivity, and also introduced a micromechanics model to compute the optimal unit cell. This unit cell was then used to determine the macro scale material properties and a Pareto Front was created relating thermally conductive optima to maximum stiffness optima. It was found that the material composition of the unit cell lattice structure significantly impacted both thermal and elastic compliance. Maute et. al [60] used level set topology optimization to design a set of printable

SMP (shape memory polymer)-elastic matrix composites to match a specified deformed shape once actuated. This two-material system was able to closely match a deformed shape once actuated, and showed that there is indeed benefit to combining advanced manufacturing, multifunctional materials, and topology optimization. Zegard and Paulino even connected additive manufacturing with topology optimization [61] and were able rapidly to transition from blank design space to optimized structure to fabricated prototype. This highlights a possible future of design, where multimaterial topology optimization processes will interface with rapid manufacturing methods to turn out highly tailored designs.

Pertaining specifically to sensing structures in topology optimization, Rubio [62] investigated topology optimization of a piezoresistive patch in a compliant mechanism in which orientation of a monolithic Wheatstone bridge was optimized in addition to the topology of the compliant structure. Gusti, Mello, and Silva [63] optimized the topology of a piezoresistive membrane that was stretched over a structure to maximize the sensing capability and the stiffness. They were able to show over 150 percent increases in measured potential difference due to the piezoresistive effect.

But so far multifunctional optimization routines are limited to one or two materials. With the advances in material manufacturing it is now possible to go further. Rather than two materials, what if the design could have a different effective material in each element? This dissertation introduces a tool that goes beyond the idea of one material or two material structures to distributed systems of nanocomposites that can have tightly controlled subspaces. Each subspace has unique effective mechanical, electrical, and peizoresistive properties. Rather than using a single pseudo-density approach, these properties are obtained via the use specific micromechanics models for each local property. These effective properties help to determine global performance objectives.

Before the specific material models and multiobjective problems are developed and solved, the next chapter introduces the general form of topology optimization. It then addresses some common issues across all multiobjective topology optimization, namely multiple minima, mesh-dependence, and checkerboarding.

Chapter 3

Multifunctional Topology Optimization

A general topology optimization problem statement is given by Equation 3.1.

$$\begin{aligned} \min \ & F(\boldsymbol{v}) \\ \text{s.t. } & \boldsymbol{G}(\boldsymbol{v}) \leq \boldsymbol{G}^{*} \\ & \boldsymbol{v}_{min} \leq \boldsymbol{v} \leq \boldsymbol{v}_{max} \end{aligned} \tag{3.1}$$

where F is the objective function to be minimized, and $\boldsymbol{G}$ is the constraint function or set of functions that must be less than or equal to some specified values $\boldsymbol{G}^{*}$. The vector of design variables that are changed throughout the optimization, $\boldsymbol{v}$, govern both the objective and constraint functions. $\boldsymbol{v}$ may also be bound by side constraints, $\boldsymbol{v}_{min}$ and $\boldsymbol{v}_{max}$.

The material-distribution method (also known as the pseudo-density method) is an optimization technique that seeks to find the optimal layout of a material within a given design space [64]. The optimization is constrained on how much of the total design space the material may occupy, and the goal is to find out how best to distribute this material to optimize the objective. This is accomplished by discretizing the design space into finite elements and assigning a design variable to each element. The method was initially applied to the maximization of structural stiffness. Rewriting Equation 3.1 for compliance minimization:

$$\begin{aligned} \min \ & F(\boldsymbol{v}) = \boldsymbol{f}^{T}\boldsymbol{u} \\ \text{s.t. } & G(v) = \int \boldsymbol{v} \, dV \leq V_{allow} \\ & \boldsymbol{v}_{min} \leq \boldsymbol{v} \leq \boldsymbol{v}_{max} \end{aligned} \tag{3.2}$$

where $\boldsymbol{f}^T\boldsymbol{u}$ is the compliance. $\boldsymbol{u}$ is the displacement, $\boldsymbol{f}$ is the force, and $\boldsymbol{K}$ is the stiffness, a function of the design variables, $\boldsymbol{v}$. At an element level, each element has an associated displacement vector, $\boldsymbol{u}_e$, force vector, $\boldsymbol{f}_e$, and stiffness matrix, $\boldsymbol{k}_e$. The subscript e indicates the terms corresponding to the eth element. The fundamental component of the pseudo-density method comes in the treatment of the modulus of elasticity of a given element, E_e.

$$E_e = v_e^p E_{mat} \tag{3.3}$$

This is the equation of the commonluy used SIMP method [2, 45, 65]. Each element modulus is weighted with a pseudo-density design variable v_e. The purpose of the method is to drive all element design variables to either 0, where the E_e is then zero, meaning that element represents a void, or to 1, where $E_e = E_{mat}$ representing an element that has the stiffness of a given material. The penalization term, p, helps to accomplish this by making intermediate values of the design variable inefficient.

In the SIMP method, the design variables represent artificial densities that need to reach 0 or 1 to relate to the real structure (or lack of structure). The intermediate density values have no physical meaning. However, it is important to notice that Equation 3.3 relates a design variable to an effective property. It is similar to a micromechanics equation that relates a local volume fraction to an effective composite property. This makes the pseudo-density method a good starting point for optimizing a structure in which the design variables are chosen as the CNT volume fractions of each element.

3.1 Problem Statement and Solution Algorithm

This dissertation formulates and solves the following topology optimization problem: What is the *best* way to distribute a constrained volume of CNTs within a design space? *Best* is defined as maximizing some set of objective functions pertaining to structural rigidity, electrical conductivity, and strain sensing via piezoresistivity. A variation of the density method is used in which the design variables are assigned as local CNT volume fractions within each element. It is assumed that the manufacturing process used to fabricate the nanocomposite structures is able to accurately mix CNT and epoxy to a given volume fraction, and in doing so the CNT are well dispersed and randomly oriented within the matrix. It is also assumed that the finite element scale is such that there are enough nanotubes to prevent boundary discontinuities between elements. Unlike the SIMP method, there is no penalization on the design variables in this dissertation. The structure will not be comprised of zeroes and ones of epoxy and CNT. This problem is posed as a mulitobjective optimization, in which the distribution of CNT is designed to satisfy two competing objectives simultaneously. Constraints are placed on both local and global CNT volume fractions. Tailoring Equation 3.1 for this problem gives

$$\begin{aligned} \min\ & F(f_1(\boldsymbol{u},\boldsymbol{\phi}), f_2(\boldsymbol{u},\boldsymbol{\phi})) \\ \text{s.t.}\ & \sum_{e=1}^{nele} v_e V_e \leq V_{allow} \\ & 0 \leq v_e \leq v_{max} \end{aligned} \tag{3.4}$$

F is the multiobjective function, which contains the single objective functions f_1 and f_2. They are functions of the state variables; the displacements $\boldsymbol{u}$ and the electric potential $\boldsymbol{\phi}$. The total volume of CNT used is determined by multiplying each element volume fraction by the element volume, $v_e V_e$, and taking the sum. This must be less than a prescribed allowable, V_{allow}. The volume fraction in each element is bound by 0 and v_{max}. Equilibrium equations for the mechanics and conservation equations for the electrostatics are functions of the design variables. They relate the state variables to the applied boundary loads and electric potentials, as per

$$\begin{aligned} \boldsymbol{K}(\boldsymbol{v})\boldsymbol{u} &= \boldsymbol{f} \\ \boldsymbol{C}(\boldsymbol{v},\boldsymbol{u})\boldsymbol{\phi} &= \boldsymbol{I} \end{aligned} \tag{3.5}$$

where the mechanical stiffness matrix $\boldsymbol{K}$ is a function of the design variables. The electrostatic matrix $\boldsymbol{C}$ is a function of both the design variables and the displacements from the mechanical solution, showing a one-way coupling. Several forms of this problem are solved in the following chapters. Four objective functions are considered: torsional rigidity GJ, electric current through a set of boundary electrodes I_{bc} representing conductivity, strain energy U representing compliance, and resistance change due to strain $\dfrac{\Delta R}{R_0}$ representing sensing. Equation 3.4 is solved using the solution algorithm in Figure 3.1. In Figure 3.1 the general optimization algorithm is shown alongside the steps pertaining to the multiobjective topology optimization.

The initialization step includes defining the finite element mesh, applying relevant loads and boundary conditions, and specifying the optimization constraints. A pre-processing step performs one time operations, such as preparing a linear density filter matrix or setting up starting conditions for a multi-start method. Once the optimization loop begins, analysis takes the current iteration's design variables and uses them to calculate local effective properties via micromechanics equations. These local effective properties are then used to obtain the global objective function values. Analytic sensitivities of the objective functions with respect to changes of the design variables are used to update the design, and convergence criteria is checked via first order optimality [66, 67]. If the optimization is not converged, the loop continues until convergence is met. Once converged, the loop ends and outputs an optimized topology (or set of topologies if a multi-start method was used) and corresponding optimized performance values of the objective functions.

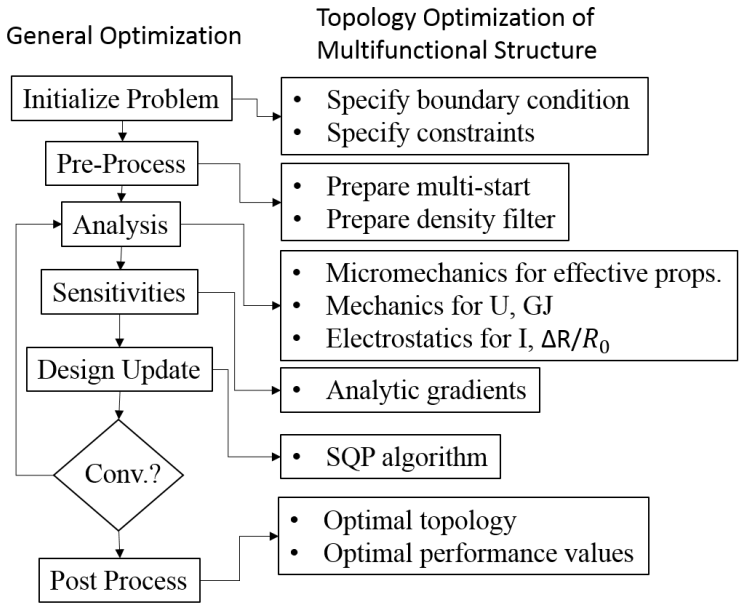

Figure 3.1: Topology optimization algorithm.

The remainder of this chapter focuses on the pre-processing steps. These include development of a restart method for alleviating the issue of local minima and implementation of a mesh independent design variable filter that also helps to prevent checkerboarding. The following chapters will introduce the specific optimization problems to be solved. The equations for relevant objectives, constraints, and sensitivities for each problem will be derived in the respective chapters.

3.2 Pre-Processing

In a review of instabilities in topology optimization Sigmund and Peterson pointed to several potential issues that must be addressed in all forms of topology optimization [44]. These include both the existence of multiple minimia and the formation of artificially efficient structures known as checkerboards. As these issues are not specific to any given objective functions or mechanics, it is beneficial to address them before the specific multifunctional composite optimization problems are introduced.

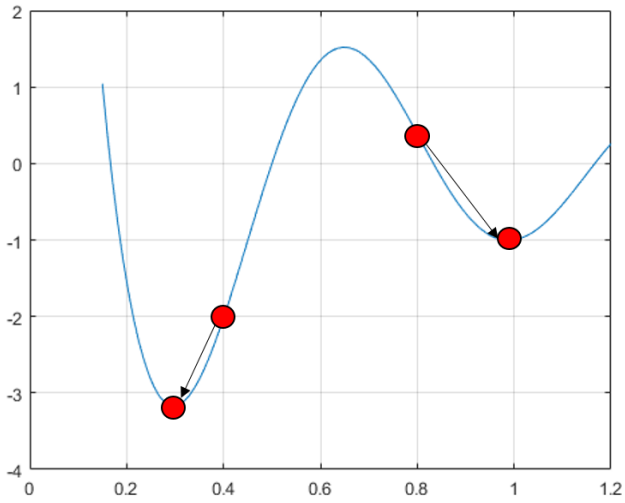

Figure 3.2: Example of a function with multiple minima

3.2.1 A Pareto Based Restart Method for Problems with Multiple Minima

"It is clear that topology optimization problems have extremely many local minima. Small changes in initial parameters... can result in drastic changes in the optimal design." -O. Sigmund and J. Peterson, 1998 [44]

In a simplified sense gradient-based optimization routines continue down a path dictated by the descent direction until they arrive at a local optima. Consider Figure 3.2. This function has one local minima near $x = 0.3$, and another local minima near the $x = 1.0$ value. Both are local minima, but $x = 0.3$ is a global minima. If the initial condition is set to $x_0 = 0.8$, the gradients of the function point towards the worse minima. Indeed, if this is the only initial condition tested, the optimizer will converge to $x = 1$, and one may never realize the better design.

One way to combat local minima to use a multi-start method, in which several optimizations are performed using different starting conditions. For example, if the optimization problem presented above is solved twice, once with $x_0 = .8$ and once with $x_0 = .4$, the global optima is obtained. But this has doubled the cost of solving the problem. Topology optimization problems have a high dimensional design space and may have large numbers of local minima, requiring large numbers of initial conditions to get sufficient coverage of the design space. As the problem becomes larger, with more and more design variables, this can become computationally expensive. It would be beneficial if instead of blindly choosing large numbers of starting conditions for expensive optimization runs there was a way to pre-select promising candidates and use those as starting points. There should be an efficient way to determine

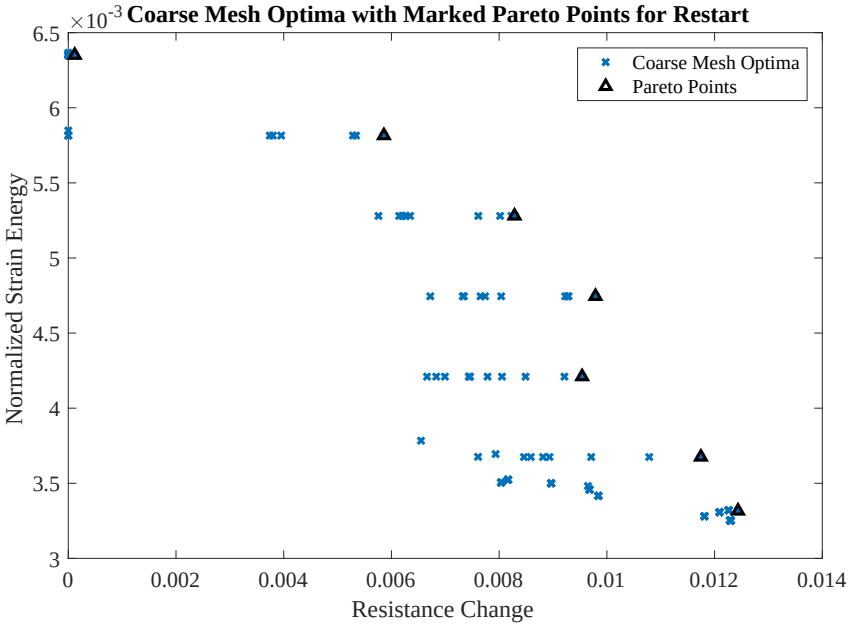

Figure 3.3: Results of the coarse mesh optimization. Marked points have their topologies saved for use as starting conditions in the refined mesh optimization.

that the starting conditions around $x_0 = 0.4$ are likely to turn out better than the starting conditions around $x_0 = .8$ in Figure 3.2.

While topology optimization exhibits mesh dependence [44], coarse mesh optima may capture general trends in the solution that can be scaled to a finer mesh. The restart method implemented here takes advantage of this fact. It first uses a multi-start method on a coarse mesh to solve a simplified version of the problem. Coarse mesh solutions are computationally inexpensive, and many starting conditions can be used to get better coverage of the design space. The best (Pareto optimal) results of the coarse mesh optimization are then selected, scaled up to a finer mesh size, and used to restart the problem. Thus, a comparatively small amount of starting conditions are used for the more expensive, fine mesh phase.

As an example, Figure 3.3 shows the results of a coarse mesh multiobjective optimization in which high resistance change and high strain energy are preferred. Each blue 'x' on the figure is the result of one full optimization of the coarse mesh problem using a random starting condition. All results in this section were obtained by using Sequential Quadratic Programming (SQP) within Matlab's *fmincon* optimization package. Function decrease tolerance, constraint feasibility tolerance, and optimality tolerance were all set to $1E-6$. Each point on the figure is the result of one full optimization of the coarse mesh problem, and was obtained by optimizing with a coarse mesh random initial condition. The tiers in the strain energy constraint were obtained by first performing single objective optimization to obtain approximate utopia points. These points were used to set the bounds on the epislon-

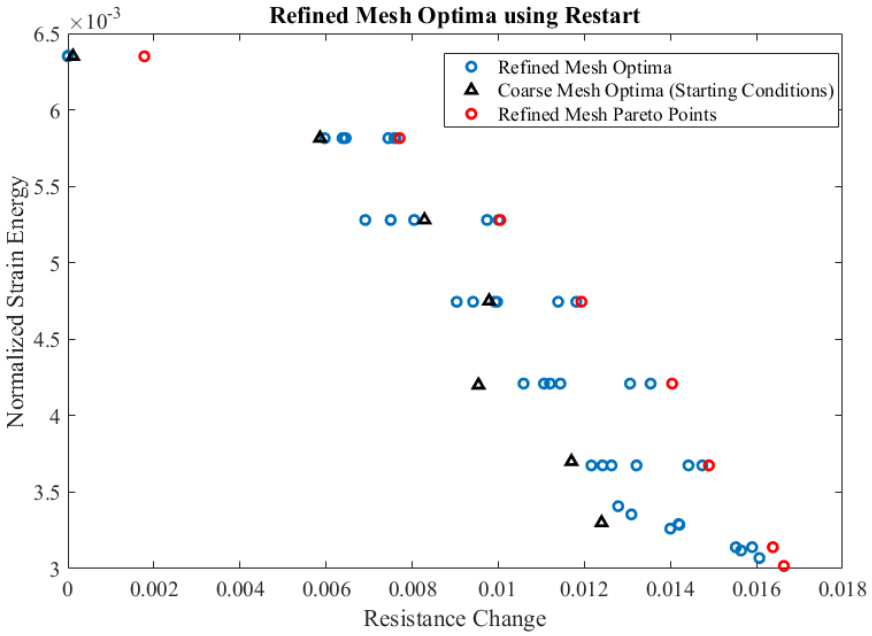

Figure 3.4: Results after scaling the mesh up to a finer size and optimizing. Coarse mesh optima are used as starting conditions.

constraint, which was linearly varied between these bounds. Additionally, one set of the random initial conditions was performed with an inactive strain energy constraint, hence the lack of tiered structuring in the bottom right of the figure.

The best points from this set of solutions are marked as nondominated points by the black triangles. The topologies which correspond to these points are scaled to the finer restart mesh size, and are used to start the finer scale, computationally expensive optimization. In the presented example, the fine mesh contains 1600 elements and the coarse mesh contains 400 elements. This four-to-one increase affects both the number of design variables in the optimization problem and also the number of elements and associated degrees of freedom in the analysis and sensitivities of the objectives, resulting in a much larger design problem. The results of the restart are shown in Figure 3.4, where the triangles mark the starting conditions kept from the coarse mesh phase, and the red circles mark the new Pareto Front. In this example problem the restart with a finer mesh is able to improve upon the initial topologies provided by the coarse mesh optimization.

It is important to note that every nondominated point from the coarse mesh is used as a starting point for every epsilon-constraint level (each level can be seen as a horizontal tier that forms in the Figure) in the refined mesh optimization. The importance of this is illustrated in Figure 3.5. Here a set of coarse mesh nondominated points, marked by the triangles, are color coded. The circles represent results of a refined mesh restart optimizations, and the color of the circle indicates which coarse mesh topology was used to restart that particular

case. It is seen that certain coarse optima may be better restart points than others, even if they are far from the original location or constraint level in the objective space. For example, restarting with the topology corresponding to the cyan triangle, C6, returns nondominated points for the restart method at 4 locations, all of which are located on a different tier than the C6 point itself.

This run of the restart method used 110 solutions of the coarse mesh optimization problem, and 77 solutions of the refined mesh problem, with starting conditions coming from the Pareto Points of the coarse mesh problem. As seen in Figure 3.6, the restart method provides better optima than using random starting conditions of the refined mesh. In this figure the red circles come from Figure 3.4. The restart method was also more computationally efficient, only using 37.2 percent of the CPU time required to obtain the Refined Mesh Random Start results.

These performance gains are not guaranteed for all applications. The Pareto-Based method does assume that the coarse mesh optimal topologies are at least somewhat representative of the fine mesh optimal topologies. In this presented study the coarse mesh contained one fourth as many elements as the fine mesh. It might be expected that as the ratio of coarse mesh to fine mesh elements increases the computational cost would continue to decrease, but the performance gain over a fine mesh random start may begin to decrease. This method also requires a mesh that can easily scale in number of elements while preserving the same topology. Unstructured meshes, or meshes with varying element sizes, may be difficult to adapt to the scaling method in its present form.

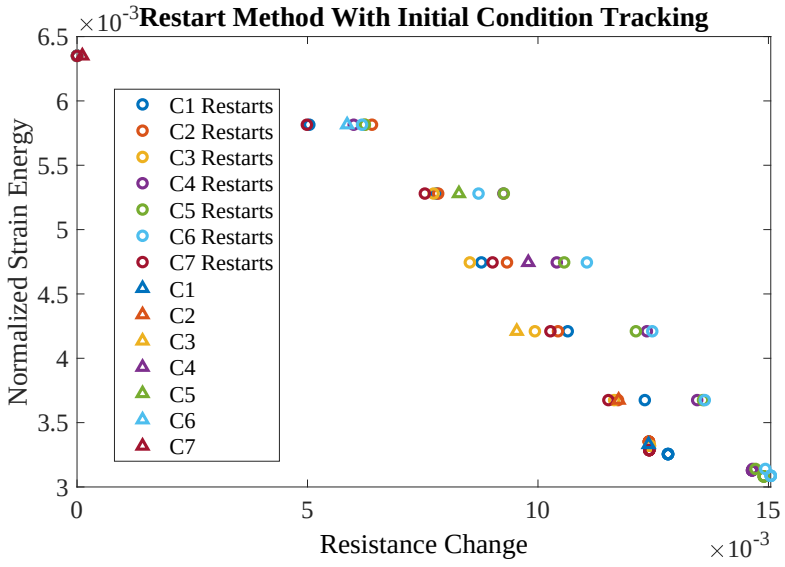

Figure 3.5: Restart Method with starting condition tracking. Coarse mesh optima are used as starting conditions.

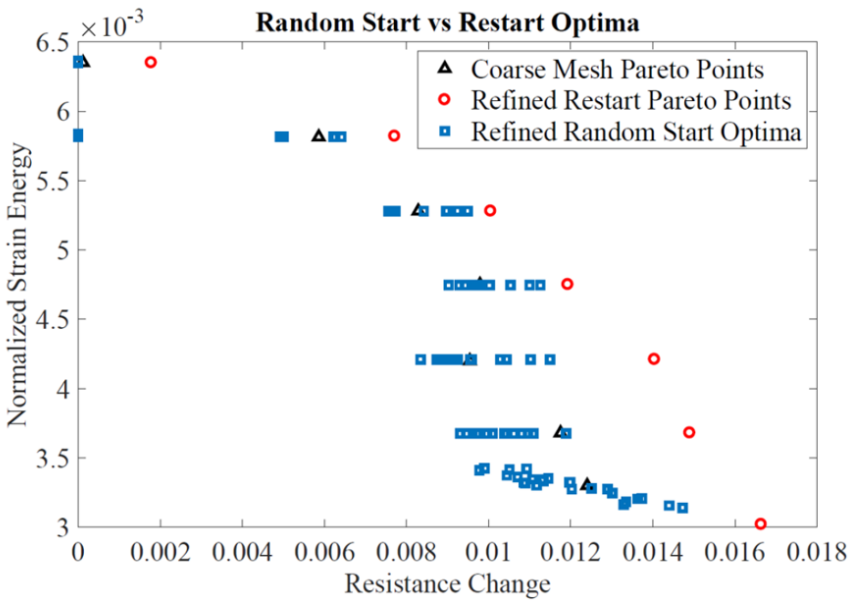

Figure 3.6: Comparing random start vs restart optima

3.2.2 Checkerboarding and the Design Variable Filter

While originally believed to be an optimal microstructure, checkerboarding is in fact a numerical error in which alternating elements connected only at a single node have artificially high performance [68, 69]. The top-left topology in Figure 3.7 shows the optimization of a structure where checkerboarding is clearly present. Of course, if one were to fabricate this structure there would be no real capability for the elements connected only at the corners to carry load.

Methods to alleviate checkerboarding include using higher order elements [68], superelement patches [70], smoothing post-processors, and filtering of either the design variables or the sensitivities [71, 72]. The first two methods add computational cost or complexity. The third method is purely a post-processing step that does not truly prevent the design from using the numerical errors inherent in checkerboards to create unrealistic optima. Filtering is advantageous in that it is incorporated into the optimization and in that, at least in the context of the filter used here, it can be set up as a pre-processing step and is not computationally expensive. A linear design variable filter is selected [72]. The filter forms a weighted average from neighboring design variables within a selected radius. The weights are based on the distance from the center of the element to be filtered to the center of the neighboring elements. This geometric filter radius is preferred as it is mesh independent and can be easily applied to a variety of problems without requiring structured meshes. Additionally, a geometric filter correlates well with an manufacturing processes, in which minimum part resolution would be given in spatial dimensions and not element lengths. The

geometric filter is applied via the following method

- The Geometric Filter
  - For each element i
    - locate all other elements with centers inside a circle of r_{min} units from the ith element. r_{min} is a user-defined filter radius.
    - determine filter weights of $\boldsymbol{W}_{ij} = \max(r_{min} - d, 0)$ where d is the distance between the ith and jth elements.
  - normalize each j row such that $\boldsymbol{W}(:, j) = \dfrac{\boldsymbol{W}(:, j)}{\sum \boldsymbol{W}(:, j)}$ to ensure the row of the filtering matrix sums to unity. The colon operator is used to indicate all rows in the matrix.
  - Apply design variable filter as $\boldsymbol{v}_{filtered} = \boldsymbol{W}\boldsymbol{v}_{unfiltered}$

The filtering matrix $\mathbf{W}$ is a function of only the mesh. It may be computed once as a pre-processing step and need not be calculated within the optimization routine. Additionally, this filter has the desirable property that any sensitivity of the filtered design variables may be multiplied by $\mathbf{W}^T$ to recover the sensitivity with respect to the unfiltered design variables, i.e.

$$F(\mathbf{v}_{unfiltered})' = [\mathbf{W}]^T F(\mathbf{v}_{filtered})' \tag{3.6}$$

where the $'$ indicates a derivative with respect to a design variable. This filter is used throughout the optimizations presented in the following chapters. The topic of filtering and appropriate minimum length scale is in itself an active area of discussion within topology optimization. See [73, 74] and [75] for examples of advanced filtering schemes.

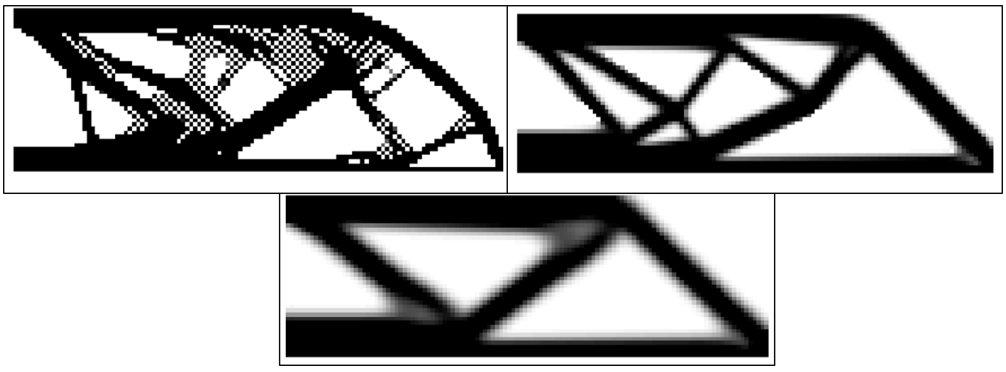

Figure 3.7: Solution to the same topology optimization problem with different filtering radii applied. Solved using the topology optimization 88 line code [53]. Top left: no filtering, checkerboarding in the solution. Top right: filter radius of 2 elements, checkerboards removed. Bottom: filter radius of 3.5 elements, filter begins to over-average design

Chapter 4

Optimization of Multifunctional CNT-Epoxy Beam Cross-Sections

In this chapter a beam subject to a prescribed twist or a prescribed curvature is designed. The design domain is illustrated in Figure 4.1. Two electrodes are attached to the beam, each with a prescribed electric potential. The goal is to design the beam's cross-sectional distribution of CNTs. The cross-section is discretized into a 2D finite element mesh and each element is given a design variable. The design variable filter described in the previous section is applied here, and the design variables after averaging represent element volume fractions of CNT. There are constraints on both the amount of CNT available to a single element and on the total amount of CNT in the cross-section, as per Equation 3.4. Micromechanics equations are introduced in the first section of the chapter and relate the local CNT volume fraction to local effective properties of stiffness, resistivity, and piezoresistivity. The local effective properties are used to solve for the global objectives in two design problems. Sensitivities of each objective function with respect to a change in the design variables are also derived.

First, the beam is loaded with a prescribed twist. The cross-section is optimized for torsional rigidity (GJ) and electric current (I_{bc}) across prescribed electrodes. For this problem the objectives are dependent on the same set of design variables, but are independent and can be calculated using uncoupled analyses. The objectives are obtained via solutions of finite element problems. A weighted-sum optimization [76, 77] is used to solve the multiobjective optimization, and results are presented as a Pareto Front of best attainable performance alongside the optimal topologies. This problem is multiobjective, but uncoupled.

The second problem introduces coupling in the form of piezoresistivity. A beam with a prescribed bending curvature is optimized for stiffness and strain sensing. Strain energy (U) is chosen as a measure stiffness. Resistance change in the presence of strain ($\frac{\Delta R}{R_0}$) is a common measure of a sensor's capability [78, 12], and is chosen as the sensing objective. An epsilon-constraint method [76, 77] is used to solve the multiobjective optimization problem,

and results are compared across a range of constraint values and boundary conditions.

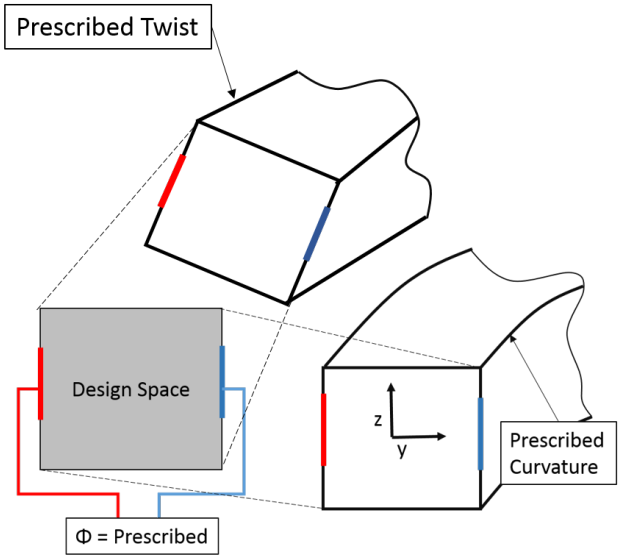

Figure 4.1: Test Case. Grey cross-section indicates the design space. Electrodes with a specified potential mark the electrostatic boundary condition. Loading is either a prescribed twist or a prescribed bending curvature.

4.1 Analysis and Sensitivity of the Objectives

Within an optimization iteration the analysis procedure follows Figure 4.2. The filtered design variables are used within element-wise micromechanics equations to obtain the local effective properties, which are then used to obtain the global objectives. These equations and their relevant sensitivities are derived in the following sections.

4.1.1 Micromechanics

Micromechanics laws relate the design variables to local Young's Modulus, resistivity, and piezoresistive constant in a given element. It is assumed that within an element the CNT are well dispersed and randomly oriented, giving linear and isotropic effective properties.

Young's Modulus

At low volume fractions the effective Young's modulus in a CNT-epoxy composite linearly increases as more CNT are added [27]. A rule of mixtures model is used to approximate the composite effective Young's modulus. The rule of mixtures equation is:

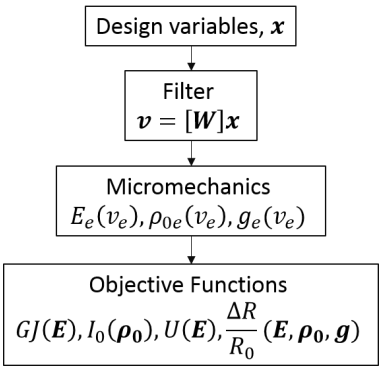

Figure 4.2: Analysis flowchart. Filtered design variables govern local element effective properties which in turn govern global objectives. The resistance change objective depends on all 3 effective properties used in the mechanics and electrostatic analyses.

$$E_e = E^{CNT} v_e + E^{mat}(1 - v_e) \tag{4.1}$$

where E_e represents the local effective Young's Modulus of the eth element, and v_e the local volume fraction of CNT in the eth element. E^{CNT} is the modulus of the CNTs, and E^{mat} is the modulus of the matrix. The rule of mixtures is continuous and differentiable, both desirable qualities when the equation is to be incorporated within an optimization algorithm. By nature of being the highest possible bound on effective modulus, the rule of mixtures model for stiffness acts to add conservatism to the sensing objective, which will be shown to be dependent on strain. The sensitivity of the Young's modulus with respect to a change in the volume fraction is

$$\frac{dE_e}{dv_e} = E^{CNT} - E^{mat} \tag{4.2}$$

Resistivity

Small increases in CNT volume fraction can decrease the composite effective resistivity by orders of magnitude [78]. This behavior is seen to be nonlinear even at low volume fractions, requiring use of an inverse rule of mixtures model [31]. Continuing with the assumption that the CNT are randomly oriented and well dispersed, it is assumed that effective resistivity is isotropic and given as

$$\rho_{0e} = \frac{1}{\dfrac{v_e}{\rho_0^{CNT}} + \dfrac{1 - v_e}{\rho_0^{mat}}} \tag{4.3}$$

where ρ_{0e} is the effective resistivity of the eth element with a local CNT volume fraction v_e. The CNT and matrix resistivities are given by ρ_0^{CNT} and ρ_0^{mat}, respectively The sensitivity is given by

$$\frac{d\rho_{0e}}{\partial v_e} = -\frac{\frac{1}{\rho_0^{CNT}} - \frac{1}{\rho_0^{mat}}}{(\rho_{0e})^2} \tag{4.4}$$

Piezoresistive Constant

Piezoresistivity is a property that dictates how changes in strain influence resistivity. A piezoresistive constant, sometimes called a normalized gage factor, can be used to measure this property. The piezoresistive constant is denoted as the variable g, and the local effective piezoresistive constant of the eth element is g_e. Bauhofer and Kovacs [79] have shown that depending on the percolation threshold of a given CNT-Epoxy composite, the piezoresistive behavior can exhibit an almost discrete on/off behavior. Below the percolation threshold the piezoresistivity is small, and at the percolation threshold the piezoresistivity is maximized. Alamusi et al. and Kuelemans [12, 80] show that after crossing percolation, continuing to add CNT will reduce the piezoresistive constant. Depending on the type of nanotube and fabrication procedure, the percolation threshold of CNT-Epoxy composites can be as low as .0025 percent CNT volume fraction [81] but it is most common that this threshold is between 1.5 and 4.5 percent [82, 79].

In the current micromechanics model 2 percent volume fraction was chosen for the percolation threshold. The effective piezoresistive constant is small before 2 percent, peaks at the percolation volume fraction of 2 percent, and decreases for larger volume fractions. A curve fit model is used to approximate this behavior, and is modeled after Figure 8 in [39].

$$g_e = \begin{cases} \sum_{i=1}^{3} A_i \tan((2i-1)\pi v_e) & v_e \leq .015 \\ 2(\cos(B_1 \pi v_e) + B_2) & .015 < v_e \leq .02 \\ -C_1 v_e^2 + C_2 v_e + C_3 & .02 < v_e \leq .1 \end{cases} \tag{4.5}$$

The sensitivity of the piezoresistive constant to the CNT volume fraction is

$$\frac{dg_e}{dv_e} = \begin{cases} \sum_{i=1}^{3} A_i (2i-1)\pi \sec((2i-1)\pi v_e)^2 & v_e \leq .015 \\ -2B_1 \pi \sin(B_1 \pi v_e) & .015 < v_e \leq .02 \\ -2C_1 v_e + C_2 & .02 < v_e \leq .1 \end{cases} \tag{4.6}$$

In Equations 4.5 and 4.6, the constants A_1-A_3, B_1-B_2, and C_1-C_3 are selected to ensure

Table 4.1: Constants used to form the element effective piezoresistivity

A_1	A_2	A_3	B_1
243613	122516	24571.2	100
B_2	C_1	C_2	C_3
1.05	406.25	16.25	3.9375

Table 4.2: Matrix and fiber material properties

	CNT	Epon
Resistivity ρ_0 (ohm/cm)	1	$1e9$
Young's Modulus E (GPA)	270	2.6

that the curve is continuous and has a continuous first derivative. These parameters may be altered to tune the piezoresistive model to fit a specific manufacturing process and/or available experimental data. Table 4.1 shows the values identified for these constants in this paper.

Material Properties and Micromechanics Plots

Material properties for CNT and Epon 862 are presented in Table 4.2 [82, **?**]. It should be noted that the Poisson's ratio of the nanocomposite was assumed to be a constant $\nu = 0.3$. Effective Poisson's ratios of CNT-Epon composites were modeled using a Mori-Tanaka method in [19, **?**], where it was found that for aligned CNT the composite effective properties were $\nu_{12} = 0.377, \nu_{23} = \nu_{13} = .263$. For randomly oriented nanotubes it can be assumed that these values may be averaged, resulting in an effective Poisson's ratio of .3.

The micromechanics equations are plotted against CNT volume fraction in Figure 4.3. This illustrates the fact that maximum stiffness and minimum resistivity are achieved via the maximum local volume fraction. The maximum piezoresistivity is achieved at a volume fraction of $v_e = .02$.

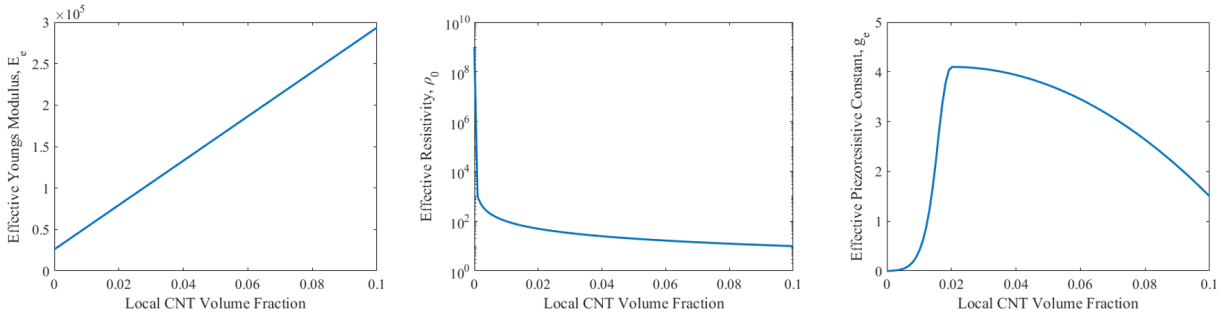

Figure 4.3: Local effective properties as a function of CNT volume fraction.

4.1.2 Objective Function: Torsional Rigidity of a Beam with Prescribed Twist

The objective that represents the cross-section's structural performance in torsion is the torsional rigidity. The solution of the Saint Venant torsion problem [83] is used to obtain the torsional rigidity of the composite cross-section. This equation is given as

$$\frac{\partial}{\partial z}\left(\frac{1}{\boldsymbol{G}(z,y)}\frac{\partial \boldsymbol{\theta}(z,y)}{\partial z}\right)+\frac{\partial}{\partial y}\left(\frac{1}{\boldsymbol{G}(z,y)}\frac{\partial \boldsymbol{\theta}(z,y)}{\partial y}\right)=-2\Theta \tag{4.7}$$

where $\boldsymbol{G}$ is the shear modulus and $\boldsymbol{\theta}$ is the Prandtl stress function. There is also a twist per length term on the right hand side, Θ. Often this term is set to a normalized value $\Theta = 1$, as is done here. This problem has been optimized for single material cross-sections by Kim [83, 84], and is extended to multiple materials here.

Torsional rigidity is defined as

$$GJ = 2\int \boldsymbol{\theta} dA \tag{4.8}$$

Which may be solved with a formulation of the weak form [85] and a solution via the finite element method. The resulting equation is of the form:

$$\boldsymbol{K}(\boldsymbol{G})\boldsymbol{\theta} = \boldsymbol{f} \tag{4.9}$$

or, for a given element

$$\boldsymbol{K}_e\boldsymbol{\theta}_e = \boldsymbol{f}_e \tag{4.10}$$

where $\boldsymbol{K_e}$ is the element stiffness matrix, $\boldsymbol{\theta_e}$ is the element stress function vector, and $\boldsymbol{f_e}$ is the element load vector.

The matrix $\boldsymbol{K_e}$ is a function of the geometry and type of element used as well as the material stiffness. In this case 4 node isoparametric bilinear quadrilateral elements [86, 87] are used to create the finite element model. The following shape functions are used for a 4 node quadrilateral element, using η and ξ to indicate element natural coordinates:

$$\begin{aligned} N_1 &= \frac{1}{4}(\xi - 1)(\eta - 1) \\ N_2 &= \frac{1}{4}(\xi + 1)(1 - \eta) \\ N_3 &= \frac{1}{4}(\xi + 1)(\eta + 1) \\ N_4 &= \frac{1}{4}(1 - \xi)(\eta + 1) \end{aligned} \tag{4.11}$$

and the gradient of the shape functions forms the gradient matrix, B.

$$\boldsymbol{B} = \begin{bmatrix} \dfrac{\partial N}{\partial \xi} \\ \dfrac{\partial N}{\partial \eta} \end{bmatrix} = \frac{1}{4}\begin{bmatrix} \eta - 1 & 1 - \eta & \eta + 1 & -(\eta + 1) \\ \xi - 1 & -(\xi + 1) & \xi + 1 & 1 - \xi \end{bmatrix} \tag{4.12}$$

Where the element constitutive matrix in torsion is given as

$$\boldsymbol{D}_e = \begin{bmatrix} \dfrac{1}{G_e} & 0 \\ 0 & \dfrac{1}{G_e} \end{bmatrix}. \tag{4.13}$$

where G_e is the element shear modulus and is related to the element Young's Modulus.

$$G_e = \frac{E_e(v_e)}{(1 + \nu)} \tag{4.14}$$

As the element shape functions were derived in natural coordinates, it is necessary to transform to physical coordinates using the Jacobian, $\boldsymbol{J}_e$.

$$\boldsymbol{J}_e = \begin{bmatrix} \dfrac{\partial Z_e}{\partial \xi} & \dfrac{\partial Y_e}{\partial \xi} \\ \dfrac{\partial Z_e}{\partial \eta} & \dfrac{\partial Y_e}{\partial \eta} \end{bmatrix} \tag{4.15}$$

where the element $Z_e = \sum x_i N_i(\xi, \eta)$ and $Y_e = \sum y_i N_i(\xi, \eta)$.

The element stiffness matrix, $\boldsymbol{K}_e$, is then given as

$$\boldsymbol{K}_e = \int_{\xi} \int_{\eta} \boldsymbol{B}^T \boldsymbol{D}_e \boldsymbol{B} |\boldsymbol{J}|_e d\xi d\eta \tag{4.16}$$

The element stiffness matrices and the load and stress function vectors are assembled into global matrices and vectors. The zero traction boundary condition is applied in order to solve the problem: $\boldsymbol{\theta}_s = 0$, where s denotes degrees of freedom on the boundary of the structure. Once $\boldsymbol{\theta}$ is obtained the torsional rigidity may be solved as

$$GJ = \boldsymbol{f}^T \boldsymbol{\theta} \tag{4.17}$$

The sensitivity of the torsional rigidity with respect to a change in the eth design variable may be computed [83]

$$\frac{\partial GJ}{\partial v_e} = \frac{\partial \boldsymbol{f}^T \boldsymbol{\theta}}{\partial v_e} = \boldsymbol{\theta}^T \boldsymbol{K} \frac{\partial \boldsymbol{\theta}}{\partial v_e} \tag{4.18}$$

Equation 4.9 may be differentiated and multiplied by $\boldsymbol{\theta}^T$. This is a form similar to the adjoint method, which will be discussed in more detail in the sensitivity of the current and the resistance change. In fact, this self-adjoint method is also how the SIMP method obtains derivatives for minimum compliance topology optimization [44]. This gives

$$\boldsymbol{\theta}^T \boldsymbol{K} \frac{\partial \boldsymbol{\theta}}{\partial v_e} = -\boldsymbol{\theta}^T \frac{\partial \boldsymbol{K}}{\partial v_e} \boldsymbol{\theta} \tag{4.19}$$

which can be used to write the sensitivity of the torsional rigidity in a form that contains the shear modulus.

$$\frac{\partial GJ}{\partial v_e} = -\boldsymbol{\theta}_{\boldsymbol{e}}^T \frac{\partial \boldsymbol{K}_{\boldsymbol{e}}}{\partial v_e} \boldsymbol{\theta}_{\boldsymbol{e}} = \frac{\partial G_e}{\partial v_e} \frac{1}{G_e} \boldsymbol{\theta}_{\boldsymbol{e}}^T \boldsymbol{K}_{\boldsymbol{e}} \boldsymbol{\theta}_{\boldsymbol{e}} \tag{4.20}$$

Finally, the sensitivity of the shear modulus is related to the micromechanics equation via the Young's Modulus.

$$\frac{\partial G_e}{\partial v_e} = \frac{\partial E_e(v_e)}{\partial v_e} \frac{1}{1+\nu} \tag{4.21}$$

and the sensitivity of the Young's Modulus to the change in the local element volume fraction is given in Equation 4.2.

4.1.3 Objective Function: Strain Energy of a Beam with Prescribed Bending Curvature

The second design problem involves the optimization of a beam cross-section under a prescribed bending curvature, representative of a sample loaded in a 3-point or 4-point bending test. The strain energy of a bending beam is a measure of structural compliance. It can be computed from bending rigidities and the bending curvatures. Bending rigidities may be computed from modified Euler-Bernoulli beam equations [83] as

$$\begin{aligned} EI_z &= \int Ey^2 dA = \sum_{e=1}^{nele} E_e y_e^2 A_e \\ EI_y &= \int Ez^2 dA = \sum_{e=1}^{nele} E_e z_e^2 A_e \\ EI_{yz} &= \int Eyz dA = \sum_{e=1}^{nele} E_e y_e z_e A_e \end{aligned} \tag{4.22}$$

where y_e and z_e are distances from the cross-section centroid of a beam with the x direction oriented along the beam's length. These are given by

$$\begin{aligned} z_e &= Z_e - Z_c \\ y_e &= Y_e - Y_c \end{aligned} \tag{4.23}$$

where Y_e and Z_e are locations of the element centers in the cross-section. Z_c and Y_c coordinates of the neutral axis, given by

$$\begin{aligned} Z_c &= \frac{\sum_{e=1}^{nele} E_e Z_e A_e}{\sum_{e=1}^{nele} E_e^{eff} A_e} \\ Y_c &= \frac{\sum_{e=1}^{nele} E_e Y_e A_e}{\sum_{e=1}^{nele} E_e^{eff} A_e} \end{aligned} \tag{4.24}$$

The bending rigidities may then be related to bending moment as

$$\begin{bmatrix} M_y \\ M_z \end{bmatrix} = \begin{bmatrix} EI_y & EI_{zy} \\ EI_{zy} & EI_z \end{bmatrix} \begin{bmatrix} \kappa_y \\ \kappa_z \end{bmatrix} \tag{4.25}$$

where κ_y and κ_z are the bending curvatures about the y and z axes. Here the problem may be simplified if the bending is applied about a single axis, and symmetry is enforced. For example let $\kappa_y = 0$, and let symmetry dictate that $EI_{zy} = 0$. From a design standpoint, this symmetry is achieved by optimizing half of the cross-section and then mirroring the design i.e. one design variable controls the volume fractions of two mirrored elements. The only remaining component of the moment is $M_z = EI_z\kappa_z$.

The strain energy is then given by

$$U = \frac{1}{2}\frac{M_z^2}{EI_z} = \frac{1}{2}EI_z\kappa_z^2 \tag{4.26}$$

and the sensitivity of the strain energy with respect to a change in the design variables is computed as

$$\frac{\partial U}{\partial v_e} = \frac{1}{2}\frac{\partial EI_z}{\partial v_e}\kappa_z^2 \tag{4.27}$$

Equation 4.26 shows that for a prescribed curvature, maximization of the strain energy corresponds to a maximization of the bending rigidity. Sensitivity of the strain energy is then dependent on the sensitivity of the bending rigidity with respect to the element volume fractions, which is given by

$$\frac{\partial EI_z}{\partial v_e} = \frac{dE_e}{dv_e}y_e^2A_e + 2\sum_{e=1}^{nele} E_e y_e \frac{\partial y_e}{\partial v_e}A_e \tag{4.28}$$

where $\dfrac{dE_e}{dv_e}$ comes from the micromechanics equations. The sensitivity of the change in the Y_c with respect to the change in design variable must also be considered.

$$\frac{\partial y_e}{\partial v_e} = \frac{\dfrac{dE_e}{dv_e}A_e\left(\sum_{e=1}^{nele} E_eY_eA_e\right) - \dfrac{dE_e}{dv_e}Y_eA_e\left(\sum_{e=1}^{nele} E_eA_e\right)}{\left(\sum_{e=1}^{nele} E_eA_e\right)^2} \tag{4.29}$$

4.1.4 Objective Function: Electric Current

Both cross-section design problems require some calculation of electric currents. In the first problem an unstrained current is optimized alongside the torsional rigidity. In the second problem a resistance change due to strain, which will be seen to be a function of both the strained and unstrained currents, is optimized alongside strain energy. Currents are obtained

via a finite element solution of the electrostatics equations. The electrostatics continuity equation (conservation of charge) states that the divergence of the current density ($\boldsymbol{\Psi}$) is 0.

$$\nabla \cdot \boldsymbol{\Psi} = 0 \tag{4.30}$$

Current density is related to electric conductivity ($\boldsymbol{\sigma}$) and the electric field ($\boldsymbol{E}$) via Ohm's law as

$$\boldsymbol{\Psi} = \boldsymbol{\sigma E} \tag{4.31}$$

The electric field is the negative of the gradient of the potential. Substituting this into Equation 4.30 gives

$$\nabla \cdot \boldsymbol{\Psi} = -\nabla \cdot (\boldsymbol{\sigma} \nabla \boldsymbol{\phi}) = 0 \tag{4.32}$$

In the 2D case the electric potential varies in the z and the y directions, $\boldsymbol{\phi} = \boldsymbol{\phi}(z, y)$. Conductivity may also change in both directions, $\boldsymbol{\sigma} = \boldsymbol{\sigma}(z, y)$. Rewriting the equation gives

$$\frac{\partial}{\partial z}\left(\boldsymbol{\sigma}(z,y)\frac{\partial \phi(z,y)}{\partial z}\right) + \frac{\partial}{\partial y}\left(\boldsymbol{\sigma}(z,y)\frac{\partial \phi(z,y)}{\partial y}\right) = 0 \tag{4.33}$$

The governing equations are discretized via the finite element method, resulting in the algebraic equations

$$\boldsymbol{C\phi} = \boldsymbol{f} \tag{4.34}$$

or, for a given element

$$\boldsymbol{C}_e \boldsymbol{\phi}_e = \boldsymbol{f}_e \tag{4.35}$$

where $\boldsymbol{C_e}$ is the element electrostatic 'stiffness' matrix, $\boldsymbol{\phi_e}$ is the element electric potential vector, and $\boldsymbol{f_e}$ is the element current vector. The electrostatic version of the stiffness matrix depends on the conductivity matrix $\boldsymbol{\sigma}$.

$$\boldsymbol{C}_e(v_e) = \int_{\xi}\int_{\eta} \boldsymbol{B}^T \boldsymbol{\sigma}_e \boldsymbol{B} |\boldsymbol{J}_e| d\xi d\eta \tag{4.36}$$

where $\boldsymbol{B}$ is the gradient matrix, $|\boldsymbol{J}_e|$ is the determinant of the element Jacobian, and $\boldsymbol{\sigma}_e = \begin{bmatrix} \sigma_{z_e} & 0 \\ 0 & \sigma_{y_e} \end{bmatrix}$ and is determined by the local element volume fraction. Prior to the application of

strain, i.e. non-piezoresistive problem, the current is calculated from element conductivities of the form $\sigma_z = \sigma_y = \dfrac{1}{\rho_{0_e}}$. For the coupled problem with strain applied, the piezoresistive term will be added and discussed in Section 4.1.5.

Equation 4.34 is divided into submatrices based on which degrees of freedom are constrained. The subscript u denotes degrees of freedom which are unspecified, but on the boundary. The subscript s indicates these degrees of freedom are part of the boundary condition, and have their electric potential specified. This represents specifying the placement of electrodes on the structure. Finally, the subscript i indicated degrees of freedom on the interior of the cross-section.

$$\begin{bmatrix} \boldsymbol{C}_{ii} & \boldsymbol{C}_{iu} & \boldsymbol{C}_{is} \\ \boldsymbol{C}_{iu} & \boldsymbol{C}_{uu} & \boldsymbol{C}_{us} \\ \boldsymbol{C}_{is} & \boldsymbol{C}_{us} & \boldsymbol{C}_{ss} \end{bmatrix} \begin{bmatrix} \boldsymbol{\phi}_i \\ \boldsymbol{\phi}_u \\ \boldsymbol{\phi}_s \end{bmatrix} = \begin{bmatrix} \boldsymbol{f}_i \\ \boldsymbol{f}_u \\ \boldsymbol{f}_s \end{bmatrix} \tag{4.37}$$

In this equation the entire $\boldsymbol{C}$ matrix is known, and $\boldsymbol{\phi}_s = \boldsymbol{\phi}_{s0}$ is known along the electrodes. $\boldsymbol{f}_u = \boldsymbol{f}_i = 0$ unless non-electrode boundary or interior currents are specified. There are two forms of these equations that are convenient for use in solving and obtaining sensitivities.

Form A:

$$\begin{bmatrix} \boldsymbol{C}_{ii} & \boldsymbol{C}_{iu} & 0 \\ \boldsymbol{C}_{iu} & \boldsymbol{C}_{uu} & 0 \\ 0 & 0 & \boldsymbol{II} \end{bmatrix} \begin{bmatrix} \boldsymbol{\phi}_i \\ \boldsymbol{\phi}_u \\ \boldsymbol{\phi}_s \end{bmatrix} = \begin{bmatrix} -\boldsymbol{C}_{is}\boldsymbol{\phi}_{s0} \\ -\boldsymbol{C}_{us}\boldsymbol{\phi}_{s0} \\ \boldsymbol{\phi}_{s0} \end{bmatrix} \tag{4.38}$$

or, in simplified Form A: $\hat{\boldsymbol{C}}\boldsymbol{\phi} = \boldsymbol{b}$. Here the symbol $\boldsymbol{II}$ is used to represent the identity matrix.

Total current, I_{bc}, is measured as the summation of the nodal currents across a boundary electrode. The vector q is created to aid in the summation. q has a value of 1 for degrees of freedom on the boundary electrode to be summed over, and is 0 for the degrees of freedom on the other boundary electrode.

$$I_{bc} = \boldsymbol{q}^T \begin{bmatrix} \boldsymbol{C}_{is}^T & \boldsymbol{C}_{us}^T & \boldsymbol{C}_{ss}^T \end{bmatrix} \boldsymbol{\phi} = \boldsymbol{p}^T \boldsymbol{\phi} \tag{4.39}$$

The adjoint method is used to obtain the sensitivity of the current. The total derivative is

$$\frac{dI_{bc}}{dv_e} = \frac{\partial I_{bc}}{\partial v_e} + \frac{\partial I_{bc}}{\partial \boldsymbol{\phi}} \frac{\partial \boldsymbol{\phi}}{\partial v_e} \tag{4.40}$$

The state equation is used to help solve the above equation. The state equation is $\hat{\boldsymbol{C}}\boldsymbol{\phi} - \boldsymbol{b} = \boldsymbol{0}$. As this equation is equal to 0, the derivative is also 0 and is given as

$$\frac{\partial \hat{\boldsymbol{C}}}{\partial v_e}\boldsymbol{\phi} + \hat{\boldsymbol{C}}\frac{\partial \boldsymbol{\phi}}{\partial v_e} - \frac{\partial \boldsymbol{b}}{\partial v_e} = \mathbf{0} \tag{4.41}$$

The sensitivity equation is appended with the above equation times the adjoint variable, $\boldsymbol{\lambda}$. Rearranging leads to

$$\frac{dI_{bc}}{dv_e} = \frac{\partial I_{bc}}{\partial v_e} + \boldsymbol{\lambda}^T(\frac{d\boldsymbol{b}}{dv_e} - \frac{d\hat{\boldsymbol{C}}}{dv_e}\boldsymbol{\phi}) + (\frac{\partial I_{bc}}{\partial \boldsymbol{\phi}} - \boldsymbol{\lambda}^T\hat{\boldsymbol{C}})\frac{\partial \boldsymbol{\phi}}{\partial v_e} \tag{4.42}$$

where $\boldsymbol{\lambda}$ may be chosen as any arbitrary vector. It is convenient to select a $\boldsymbol{\lambda}$ that makes the third term in the above equation 0. This results in the adjoint state equation:

$$\hat{\boldsymbol{C}}\boldsymbol{\lambda} = (\frac{\partial I_{bc}}{\partial \boldsymbol{\phi}})^T = \boldsymbol{p} \tag{4.43}$$

which is solved for $\boldsymbol{\lambda}$ and substituted to obtain the adjoint form of the sensitivity.

$$\frac{dI_{bc}}{dv_e} = \frac{\partial I_{bc}}{\partial v_e} + \boldsymbol{\lambda}^T(\frac{d\boldsymbol{b}}{dv_e} - \frac{d\hat{\boldsymbol{C}}}{dv_e}\boldsymbol{\phi}) \tag{4.44}$$

It is now necessary to derive each of the terms:$\frac{\partial I_{bc}}{\partial v_e}$, $\frac{db}{dv_e}$, and $\frac{d\hat{C}}{dv_e}$.

$$\frac{\partial I_{bc}}{\partial v_e} = \boldsymbol{q}^T(\frac{d}{dv_e}\begin{bmatrix}\boldsymbol{C}_{is}^T & \boldsymbol{C}_{us}^T & \boldsymbol{C}_{ss}^T\end{bmatrix})\boldsymbol{\phi} \tag{4.45}$$

$$\frac{db}{dv_e} = (\frac{d}{dv_e}\begin{bmatrix}-\boldsymbol{C}_{is} \\ -\boldsymbol{C}_{us} \\ II\end{bmatrix})\boldsymbol{\phi_{s0}} \tag{4.46}$$

$$\frac{d\hat{C}}{dv_e} = \frac{d}{dv_e}\begin{bmatrix}\boldsymbol{C}_{ii} & \boldsymbol{C}_{iu} & 0 \\ \boldsymbol{C}_{iu} & \boldsymbol{C}_{uu} & 0 \\ 0 & 0 & \boldsymbol{II}\end{bmatrix} \tag{4.47}$$

The above equations depend on the sensitivities of the electrostatic stiffness matrix with respect to changes in the design variables. As these variables (the CNT volume fractions in each element) are local, sensitivity of a particular element matrix can be used for the sensitivity of the element volume fraction.

$$\frac{\partial \boldsymbol{C}_e}{\partial v_e} = \boldsymbol{B}^T\frac{\partial \boldsymbol{\sigma}_e}{\partial v_e}\boldsymbol{B}|\boldsymbol{J}|_e \tag{4.48}$$

$$\frac{\partial \boldsymbol{\sigma}_e}{\partial v_e} = \begin{bmatrix} \frac{\partial \sigma_{z_e}}{\partial v_e} & 0 \\ 0 & \frac{\partial \sigma_{y_e}}{\partial v_e} \end{bmatrix} \tag{4.49}$$

where $\frac{\partial \sigma_{z_e}}{\partial v_e}$ and $\frac{\partial \sigma_{y_e}}{\partial v_e}$ have explicit known values based on the micromechanics laws used. All the terms needed to solve for the sensitivity are now known.

Care must be taken to choose the correct indices for each v_e, as each v_e corresponds to an element, and that element may have nodal degrees of freedom that lie on the interior, on the unprescribed boundary, and/or on the electrode. This can be simplified if the adjoint method is applied to the alternate solution of the current.

Form B:

$$\begin{bmatrix} \boldsymbol{C}_{ii} & \boldsymbol{C}_{iu} & 0 \\ \boldsymbol{C}_{iu}^T & \boldsymbol{C}_{uu} & 0 \\ \boldsymbol{C}_{is}^T & \boldsymbol{C}_{us}^T & -\boldsymbol{I}\boldsymbol{I} \end{bmatrix} \begin{bmatrix} \boldsymbol{\phi}_i \\ \boldsymbol{\phi}_u \\ \boldsymbol{f}_s \end{bmatrix} = \begin{bmatrix} -\boldsymbol{C}_{is}\boldsymbol{\phi}_{s0} \\ -\boldsymbol{C}_{us}\boldsymbol{\phi}_{s0} \\ -\boldsymbol{C}_{ss}\boldsymbol{\phi}_{s0} \end{bmatrix} \tag{4.50}$$

And the simplified Form B: $\tilde{\boldsymbol{C}}\boldsymbol{y} = \tilde{\boldsymbol{b}}$. The solution follows the same steps as the solution of Form A. First, the current is given as

$$I_{bc} = \begin{bmatrix} \mathbf{0} & \mathbf{0} & \boldsymbol{q} \end{bmatrix}^T \boldsymbol{y} \tag{4.51}$$

Then the adjoint equation (the state variable is now y instead of ϕ) is updated

$$\tilde{\boldsymbol{C}}^T \tilde{\boldsymbol{\lambda}} = \frac{\partial I_{bc}}{\partial \boldsymbol{y}} = \boldsymbol{q}^T \tag{4.52}$$

and finally the sensitivity equation is updated as

$$\frac{dI_{bc}}{dv_e} = \frac{\partial I_{bc}}{\partial v_e} + \tilde{\boldsymbol{\lambda}}^{\boldsymbol{T}} \left(\frac{d\tilde{\boldsymbol{b}}}{dv_e} - \frac{d\tilde{\boldsymbol{C}}}{dv_e}\boldsymbol{y} \right) \tag{4.53}$$

Here the form of I_{bc} is convenient in that $\frac{\partial I_{bc}}{\partial v_e} = 0$. Furthermore, it is noted that $(\frac{d\tilde{\boldsymbol{b}}}{dv_e} - \frac{d\tilde{\boldsymbol{C}}}{dv_e}\boldsymbol{y})$ may be rearranged, as it is a derivative of the original electrostatic equations, $\boldsymbol{C}\boldsymbol{\phi} = \boldsymbol{f}$

$$\frac{d}{dv_e} \begin{bmatrix} -\boldsymbol{C}_{is}\boldsymbol{\phi}_{s0} \\ -\boldsymbol{C}_{us}\boldsymbol{\phi}_{s0} \\ -\boldsymbol{C}_{ss}\boldsymbol{\phi}_{s0} \end{bmatrix} - \frac{d}{dv_e} \left(\begin{bmatrix} \boldsymbol{C}_{ii} & \boldsymbol{C}_{iu} & 0 \\ \boldsymbol{C}_{iu}^T & \boldsymbol{C}_{uu} & 0 \\ \boldsymbol{C}_{is}^T & \boldsymbol{C}_{us}^T & -I\!I \end{bmatrix} \right) \begin{bmatrix} \boldsymbol{\phi}_i \\ \boldsymbol{\phi}_u \\ \boldsymbol{f}_s \end{bmatrix} = -\frac{d\boldsymbol{C}}{dv_e}\boldsymbol{\phi} \tag{4.54}$$

The differentiation of the Form B equations is independent of whether or not the element contains boundary degrees of freedom.

$$\frac{dI_{bc}}{dv_e} = -\tilde{\boldsymbol{\lambda}}^T \frac{d\boldsymbol{C}}{dv_e}\boldsymbol{\phi} = -\tilde{\boldsymbol{\lambda}_e}^T((\boldsymbol{B}^T \frac{\partial \boldsymbol{\sigma}_e}{\partial v_e}\boldsymbol{B}|\boldsymbol{J}|_e)\boldsymbol{\phi}_e) \tag{4.55}$$

4.1.5 Objective Function: Resistance Change due to Strain

Resistance change due to strain, $\frac{\Delta R}{R_0}$, is measured as the difference in resistance between the unstrained structure (R_0) and the resistance of the strained structure (R_ϵ), normalized by the unstrained resistance i.e.

$$\frac{\Delta R}{R_0} = \frac{R_\epsilon - R_0}{R_0} \tag{4.56}$$

Resistance is related to current through Ohm's law, $R = \frac{V}{I} = \frac{\Delta\phi}{I_{bc}}$. $\Delta\phi$ is the prescribed potential difference across the electrodes, and is a constant for both the strained and unstrained resistances. This allows for simplification of the resistance change function.

$$\frac{\Delta R}{R_0} = \frac{R_\epsilon - R_0}{R_0} = \frac{I_{bc_0}}{I_{bc_\epsilon}} - 1 \tag{4.57}$$

Thus, the resistance change requires the calculation of two different currents. The currents may be calculated using the equations in the previous section, but differ in the formulation of the conductivity matrix. The unstrained element conductivity matrix is

$$\boldsymbol{\sigma}_{0e} = \begin{bmatrix} \frac{1}{\rho_{0e}} & 0 \\ 0 & \frac{1}{\rho_{0e}} \end{bmatrix} \tag{4.58}$$

where ρ_{0e} is given explicitly by Equation 4.3, and has a sensitivity given by Equation 4.4. The sensitivity of the unstrained conductivity matrix is then

$$\frac{\partial \boldsymbol{\sigma}_{0_e}}{\partial v_e} = \begin{bmatrix} -\frac{\frac{\partial \rho_{0_e}}{\partial v_e}}{\rho_{0_e}^2} & 0 \\ 0 & -\frac{\frac{\partial \rho_{0_e}}{\partial v_e}}{\rho_{0_e}^2} \end{bmatrix} \tag{4.59}$$

Once the structure is loaded the resistivity changes due to the piezoresistive effect. This adds an additional term to the resistivity equation [88, 10]. For a beam with prescribed bending curvature about a single axis it is assumed that the axial strain dominates this response. The resistivity of the e^{th} element in the presence of strain is given as

$$\rho_{\epsilon_e} = \rho_{0_e}(1 + g_e \epsilon_{xx_e}) \tag{4.60}$$

The above equation leads to changes in the sensitivity as the piezoresitive constant is a direct function of the element volume fraction. Also, the axial strain in an element depends on the prescribed curvature and the distance of the element from the centroid.

$$\epsilon_{xx_e} = \kappa_z y_e \tag{4.61}$$

Thus, the sensitivity of the strained resistivity is

$$\frac{\partial \rho_{\epsilon_e}}{\partial v_e} = \frac{\partial \rho_{0_e}}{\partial v_e}(1 + g_e \kappa_z y_e) + \rho_{0_e} \frac{\partial g_e}{\partial v_e} \kappa_z y_e + \rho_{0_e} g_e \kappa_z \frac{\partial y_e}{\partial v_e} \tag{4.62}$$

where $\dfrac{\partial \rho_{0_e}}{\partial v_e}$ is given by Equation 4.4, $\dfrac{\partial g_e}{\partial v_e}$ is given by Equation 4.6, and $\dfrac{\partial y_e}{\partial v_e}$ is given by Equation 4.29. Finally, Equations 4.60 and 4.62 are substituted into Equations 4.58 and 4.59, which are in turn used to solve for strained current and sensitivity by repeating either the Form A or Form B calculations from the previous section.

4.2 Results

With the pre-processing steps complete and the objective functions and their sensitivities derived it is now possible to formulate and solve the multiobjective optimization problems. The beam cross-section in torsion is presented first.

4.2.1 Optimization of a Beam Cross-Section for Torsional Rigidity and Electrical Conductivity

By creating a multifunctional structure that is capable of forming conductive networks between electrodes and simultaneously carrying load it may be possible to reduce system part count and simplify designs. The conductive network may serve to power other on-board systems or provide electrical grounding and/or ESD shielding [89, 90]. While this additional capability is desirable, the structure must still be stiff enough to resist the expected loading environment, in this case a prescribed twisting. The optimization will seek to maximize both

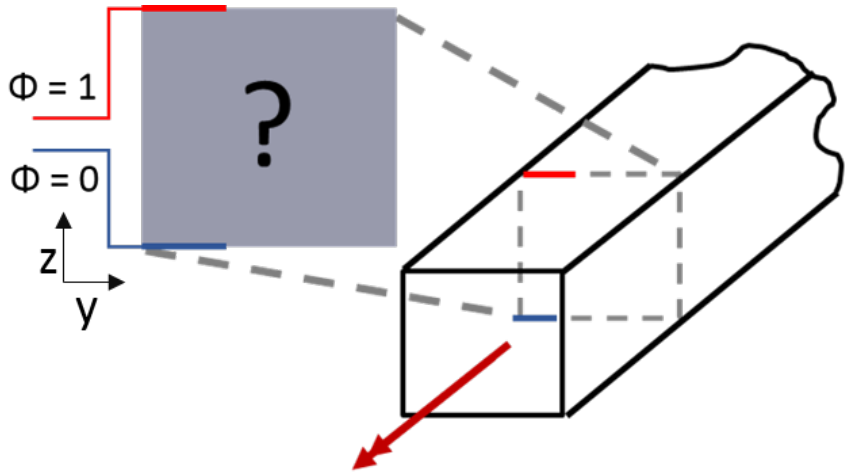

Figure 4.4: Illustration of a multifunctional beam under unit twist and with a prescribed unit voltage drop across electrodes.

the conductivity between electrodes and the torsional rigidity of the beam cross-section. The problem is subjected to a unit twist and a unit potential voltage drop is prescribed across electrodes. The problem is illustrated in Figure 4.4.

A weighted-sum method [76] is used to combine the two objective functions, and constraints are imposed on both local and global allowable volume fractions of CNT. Relative weight factors, w_1 and w_2, are used to determine the influence of each objective on the multiobjective optimization. Typically $w_2 = 1 - w_1$. These weights are modified to calculate points on the Pareto Front of multiobjective optima [91]. Scale factors s_1 and s_2 are used to normalize the objective functions. Normalization is required because the objectives may be of different by orders of magnitude. If this is the case the larger objective will dominate the design even if its associated weighting was low.

$$\begin{aligned} \min\ F &= \frac{w_1}{s_1} GJ + \frac{w_2}{s_2} I_{bc0} \\ \text{s.t.}\ & \int \boldsymbol{v}\ dV \leq V_{allow} \\ & 0 \leq \boldsymbol{v} \leq v_{max} \end{aligned} \tag{4.63}$$

The problem is solved using a sequential quadratic programming method within Matlab's *fmincon* function [49, 92]. The local volume fraction constraints are given as side constraints, with 0 percent CNT (pure matrix) as the lower bound and 10 percent CNT as the upper bound ($v_{max} = .10$). 10 percent CNT has been shown to be a general upper limit after which manufacturing of the CNT composite may prove problematic [93]. The global volume fraction constraint is set to 3% CNT. Analytic sensitivities are provided for the objective

functions per the previous sections. The sensitivity of the global volume fraction constraint is straightforward to compute.

$$G(\boldsymbol{v}) = \int \boldsymbol{v}\ dV \leq V_{allow} = \frac{\sum_{e=1}^{nele} v_e V_e}{V_{allow}} - 1 \leq 0 \tag{4.64}$$

$$\frac{\partial G}{\partial v_e} = \frac{V_e}{V_{allow}} \tag{4.65}$$

The scale factors in the weighted sum optimization are determined by using the utopia point, the best possible values for each of the objective functions as determined by performing single objective optimization. A Pareto Front, shown in Figure 4.5, is generated by performing nine optimizations with nine different w_1 and w_2 combinations. $w1$ linearly decreases from 1 to 0, and $w2$ increases from 0 in mirroring fashion.

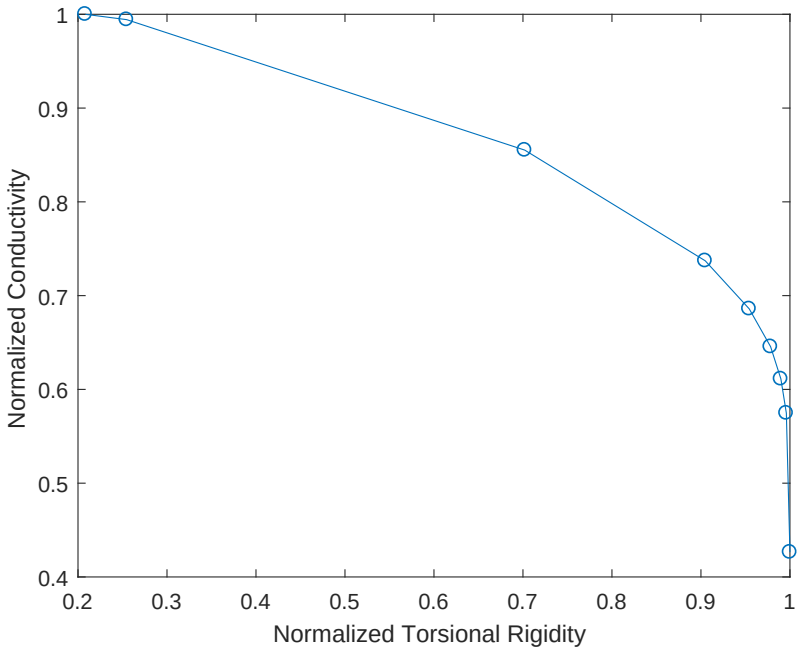

Figure 4.5: Pareto Front of mulitobjective optima for maximum torsional rigidity and conductivity

The Pareto Front compares optimized values of the two objectives, normalized by their respective scale factors. Note the slope in the Pareto Front as the normalized torsional rigidity increases. While there is a nearly linear trade-off in sacrificing conductivity to gain rigidity for 20 to 80 percent of the max attainable rigidity, past that any further increase

incurs increasingly larger losses in conductivity. It is possible to have 90 percent of the max attainable rigidity and retain over 75 percent of the max attainable conductivity. However, in order to reach the highest torsional rigidity attainable, the design can provide less than 45 percent of the max conductivity. The purpose of the Pareto Front is to offer a series of solutions for these types of multiobjective questions. The designer may say, "I need X torsional rigidity or my structure will be too flexible, how much conductivity can I get?" The Pareto Front provides the answer.

Each point marked on Figure 4.5 has an associated topology, shown in Figure 4.6. In these images each element is given a color that represents the local CNT volume fraction, as specified by the color bar. There are no voids in the structure. A local volume fraction of 0, the dark blue elements, represents pure matrix. The weighted-sum weight factors are displayed beneath the topologies, with w_1 showing the relative weighting on torsional rigidity and w_2 showing the weighting on electrical conductivity. When only torsional rigidity is considered, the optimization places the stiff CNT in a design that resembles a circular cylinder embedded within the matrix. As the importance of conductivity increases, more of the highly conductive CNTs are pulled to the conductive path between the electrodes. For the design with equal weighting factors on both objectives, $w_1 = w_2 = .5$ the topology represents more of a 'D' section embedded in the matrix.

Eventually the conductivity objective dominates and the torsional ring breaks down completely, leading to a design that places as much material between the electrodes as possible. These last two topologies in the figure have very little torsional rigidity when compared to the other designs. They have the performance shown in the two most upper left points in Figure 4.5. They have almost the maximized conductivity but less than 30 percent of the attainable rigidity. Even the topology for $w_1 = .25$ is able to retain over 70 percent of the rigidity. In summary, unless the purpose of the cross-section is to act purely as a conductor, it is likely necessary to form some sort of embedded tube section out of the stiff CNT. Then one can tailor how much of this section connects the electrodes based on how much conductivity is required to effectively perform the application, be it powering a component, shielding, etc. This illustrates how the topology plots are used along with the Pareto Front to relate performance to a manufactured cross-section.

Of course, the designer may not be satisfied with only 9 possible solutions to their multiobjective problem. Using more weighting combinations may lead to a better defined Pareto Front, as seen if Figure 4.7. However, each Pareto point requires another optimization, so a proper balance must be struck between a sufficiently well defined front and a sufficiently efficient computational method. It is also important to note that the points are not evenly distributed along the Pareto Front, with more points being clustered towards the higher torsional rigidity values. This highlights a potential shortcoming of the weighted-sum method. Even if w_1 and w_2 are uniformly varied, there is no guarantee that points will give uniform coverage of the Pareto Front.

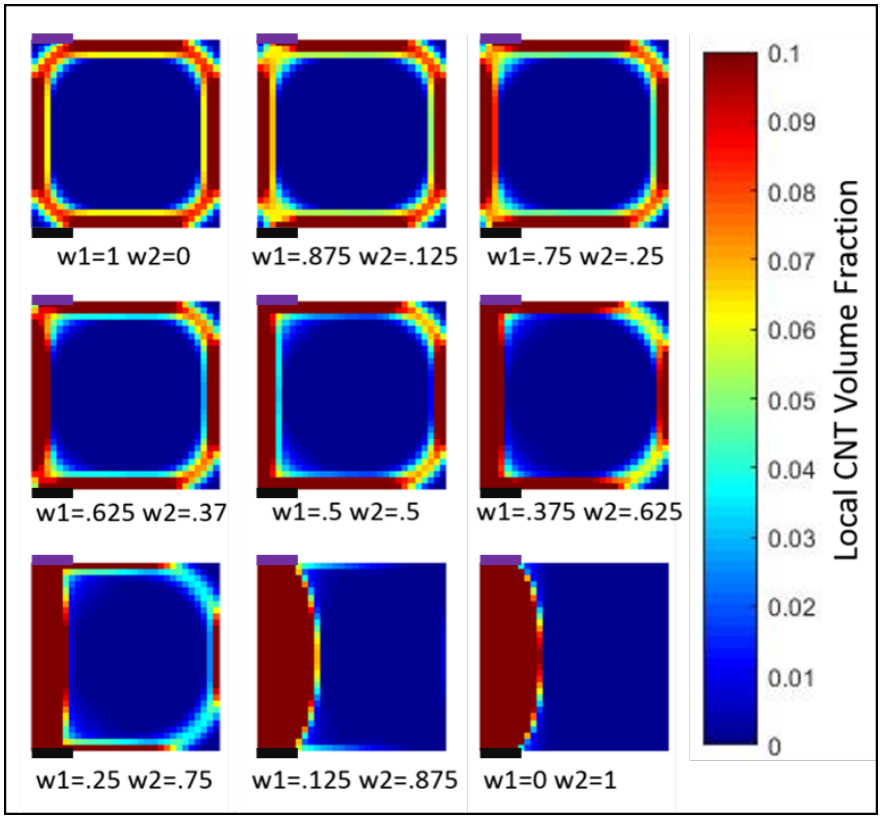

Figure 4.6: Optimized topologies for torsional rigidity and electrical conductivity. Black and purple lines mark the location of the electrodes.

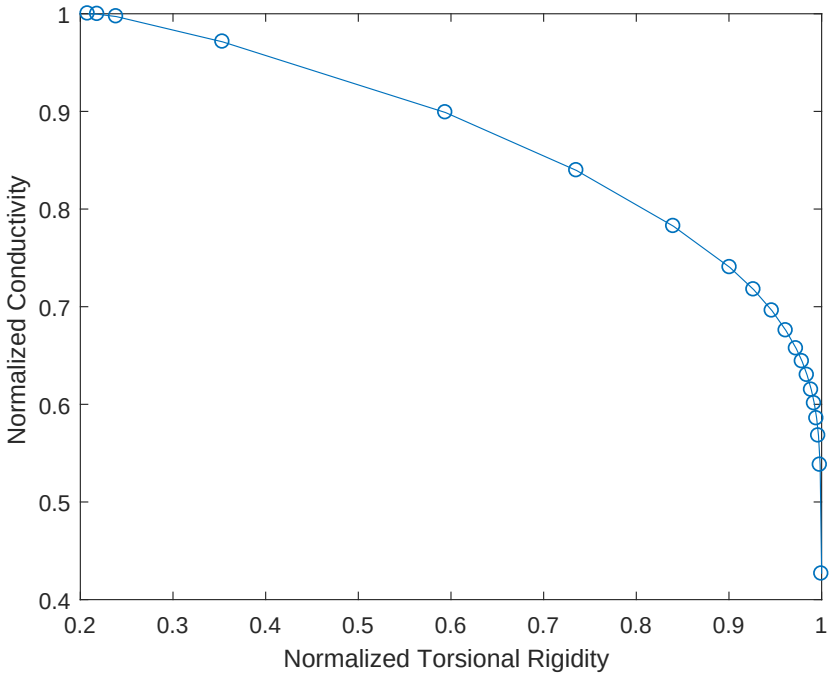

Figure 4.7: Pareto Front of mulitobjective optima for maximum torsional rigidity and conductivity with additional points.

4.2.2 Optimization of a Beam Cross-Section for Bending Rigidity and Strain Sensing

The previous problem showed the optimization of an uncoupled multifunctional system. While the topologies had to balance torsional rigidity and electrical conductivity as per the assigned weight factors, the mechanics that govern torsional rigidity and the electrostatics that govern conductivity were not directly connected. The introduction of strain sensing as an objective changes this via the introduction of a one way coupling. Section 4.1.5 shows that the electrostatics equations considering piezoresistivity are dependent on the strains from the mechanics.

In order to better distribute points along the Pareto Front this problem is solved using an epsilon-constraint optimization [77, 76, 94]. The strain energy objective is re-posed as a constraint i.e.

$$\begin{aligned} \min\ F &= -\frac{\Delta R}{R_0} \\ \text{s.t. } U &\geq U* \\ \int \boldsymbol{v}\ dV &\leq V_{allow} \\ 0 \leq \boldsymbol{v} &\leq v_{max} \end{aligned} \tag{4.66}$$

U^* is a prescribed minimum strain energy. Increasing U^* requires the design to increase stiffness, often at the cost of sensing. By changing U^* one can trade relative importance of stiffness versus sensing in the design. However, care must be taken in the selection of U^* to ensure the constraint is feasible. This is achieved by first performing single objective optimization to obtain approximate utopia points. These points are used to set the bounds of U^*, which is then linearly varied. Additionally, one run of the multi-start optimization is performed with an inactive strain energy constraint. The epsilon-constraint method is chosen over the weighted-sum method for more complex problems as it can force an even distribution of points along the Pareto Front. It also helps to determine any non-convex regions of the Pareto Front. Epsilon-constraint method reformulates the multiobjective problem into 'Give the best value of Objective A while satisfying constraints on Objective B to a defined threshold'.

The coupled optimization may exhibit many local minima. This motivates the use of the restart method outlined in Section 3.2.1. A trade study is performed to compare the effect of different global volume fraction constraints. Additionally, another trade compares six different boundary electrode locations. This results in a total of eighteen applications of the restart method to generate eighteen Pareto Fronts. The six boundary conditions are labeled and illustrated in Figure 4.8.

The problem is first solved for a 2% global volume fraction constraint. This is then doubled to 4%, and then finally the global volume fraction constraint is removed, effectively making the total allowable volume fraction 10% due to the local side constraints. For each Pareto Front, a coarse mesh of 20 x 20 elements is first optimized. The coarse mesh uses 11 different epsilon-constraint values and 10 different random starting conditions, for 110 total coarse optimizations. The nondominated points from this mesh have their associated topologies scaled to a 40 x 40 mesh and used as initial conditions for the restart method. As an example, Figure 4.9 shows the coarse mesh multi-start optimization results for a 2% global volume fraction constraint and the full length electrode boundary condition, BC1. The triangles mark the nondominated points that are kept for use in the restart method, and each point has an associated cross-section topology. Three of these topologies are shown in the Figure 4.9, with the color bar representing local CNT volume fraction in each element. The restart method results for this problem are shown in Figure 4.10. Here the black triangles are the kept nondominated points from the coarse mesh step. The blue circles mark optima obtained from the restart method, the red circles mark the new Pareto Front.

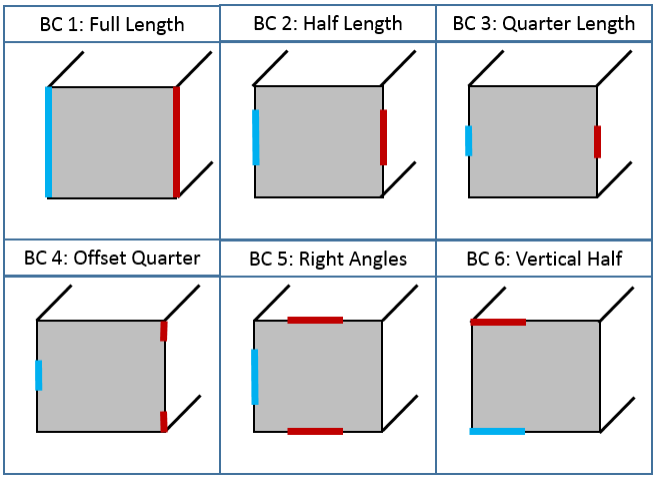

Figure 4.8: Boundary condition electrode placement

Note that the coarse mesh optima more closely match the restart optima in areas where the strain energy constraint is higher. The strain energy optima is likely a global optima and the optimal topology can be well represented with a coarse mesh. However, once this high strain energy constraint is relaxed and resistance change increases, the coupled physics lead to a more complicated design space with many optima. The specific mechanisms driving these optima are explained in the following results sections.

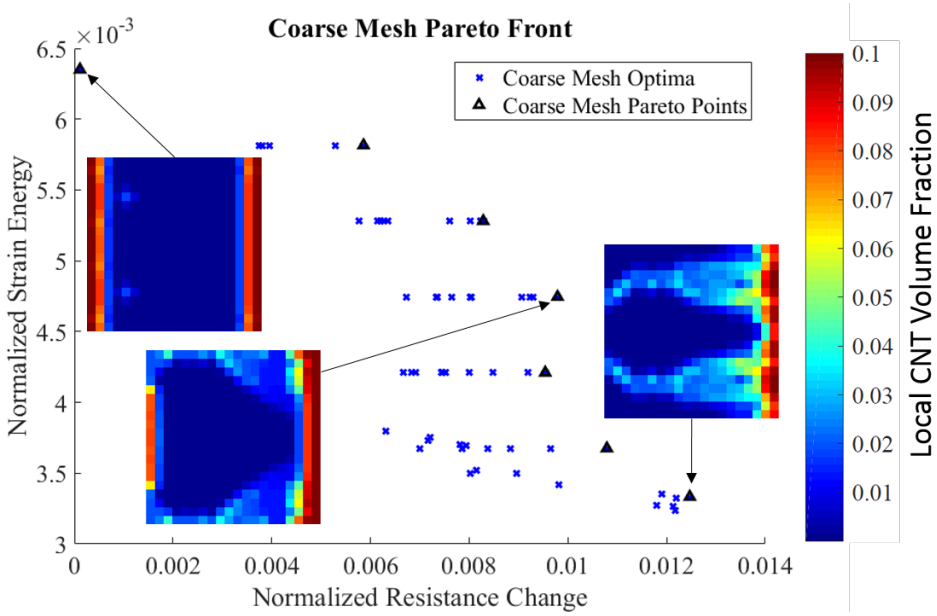

Figure 4.9: Coarse mesh multi-start results for a 2 percent volume fraction constraint and BC1.

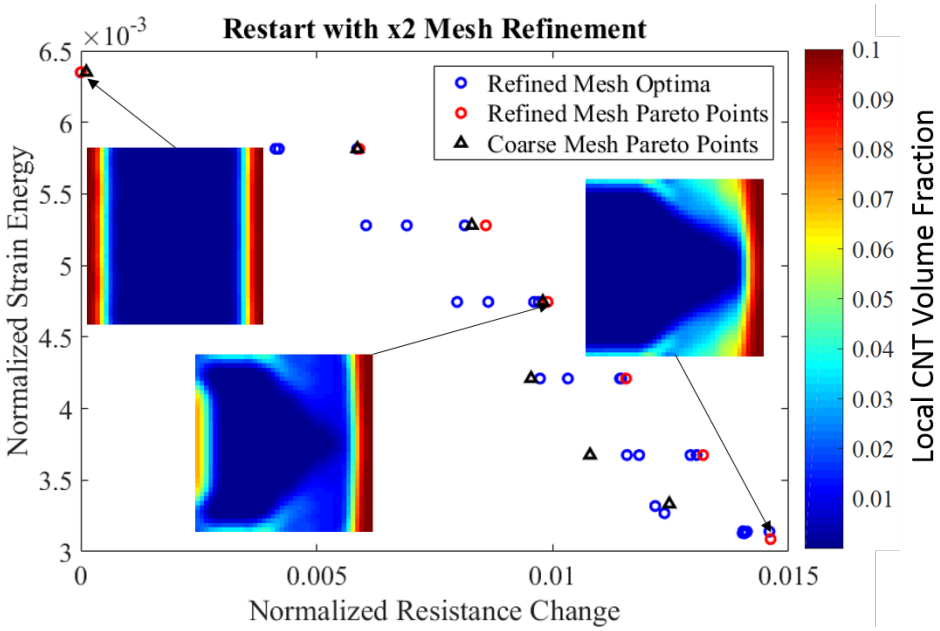

Figure 4.10: Refined mesh restart method results for a 2 percent volume fraction constraint and BC1.

Strain Energy and Resistance Change Optimization with a 2 Percent Global Volume Fraction Constraint

The refined mesh Pareto Fronts associated with the 2% global volume fraction constraint are shown in Figure 4.11. A Pareto Front is shown for each of the 6 boundary conditions listed in 4.8. Numbered markers are used to relate the specific Pareto point to its topology in Figure 4.12. Each labeled topology is presented with its strain energy and resistance change. Boxed black and grey lines on the boundary of the topologies mark the boundary electrode locations and the color bar maps the local CNT volume fraction.

It is apparent that the 'best' design for maximizing strain energy is a sandwich beam with all the CNT distributed as far from the vertical neutral axis as possible. This is a somewhat intuitive result, as adding CNT adds local stiffness per the rule of mixtures, the optimizer maximizes the bending rigidity about the vertical axis by moving the stiffening CNT to the edge of the cross-section.

The resistance change maximized topologies, labeled BC1.2.3-BC6.2.3, all share a stiff right side and a conductive path of lower volume fraction elements connecting the electrodes for the respective boundary condition. In explaining these topologies it is important to note that higher volume fraction elements cause horizontal shifts in the neutral axis location. This means one edge of the cross-section may see higher strains, and as piezoresistivity is dependent on the strain it may be beneficial to put highly piezoresistive material in this

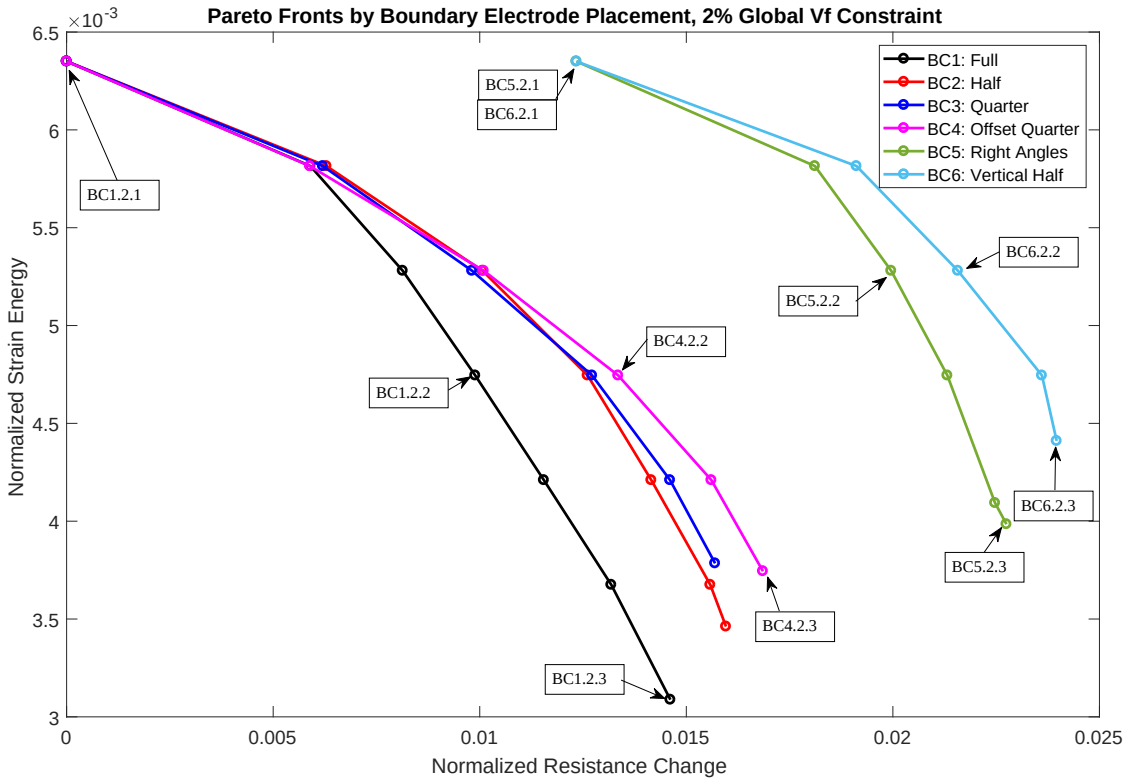

Figure 4.11: Pareto Fronts with labeled nondominated points. 2% volume fraction constraint.

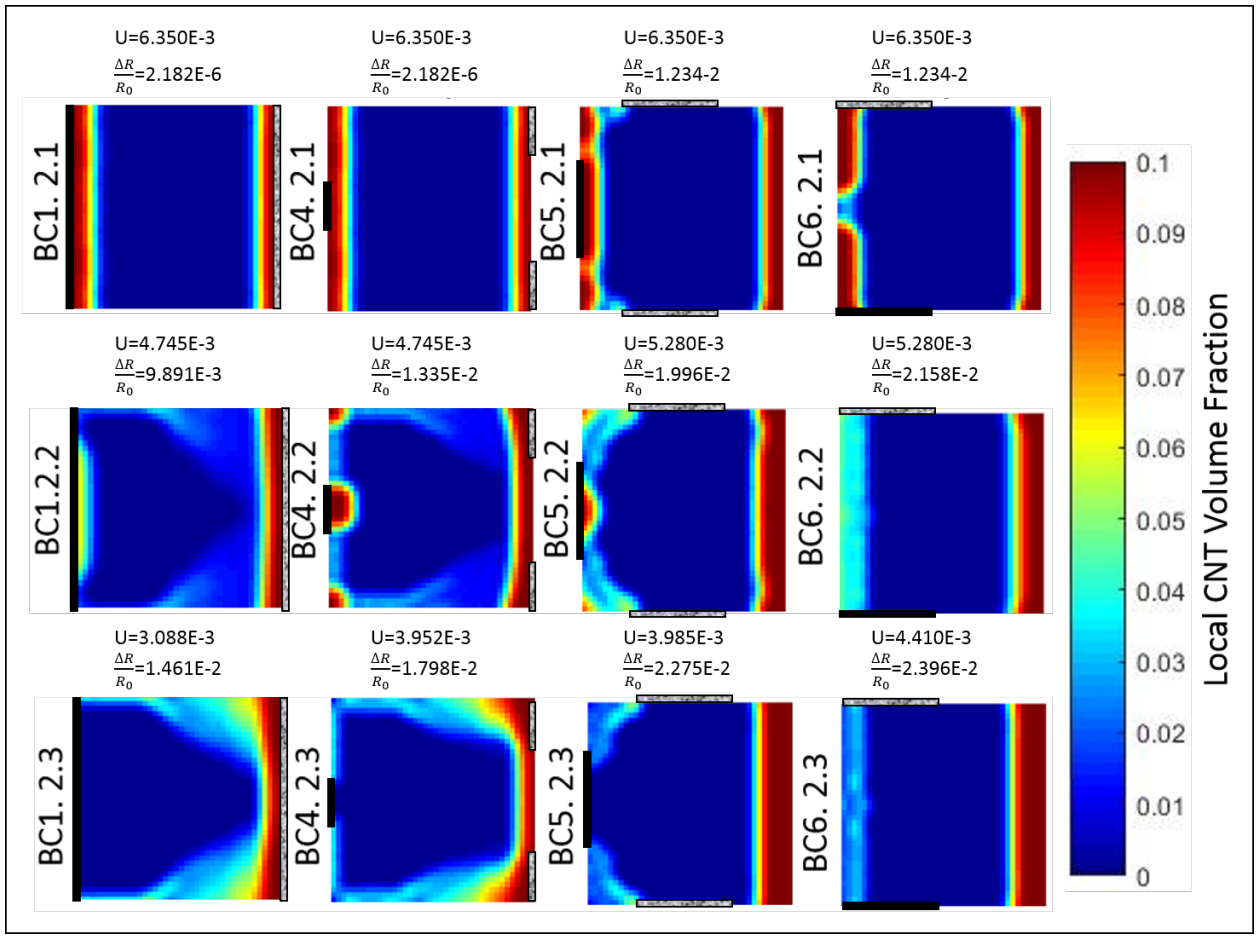

Figure 4.12: Comparing topologies with a 2% volume fraction constraint.

region. The micromechanics equation for resistivity in the presence of strain, Equation 4.60, is sign dependent. Two elements of the same volume fraction on exact sides of the neutral axis will generate opposite resistance change contributions. It is beneficial to have stiff material on one side of the cross-section and highly piezoresistive material on the opposite side. The stiff material pulls the neutral axis in that direction and the highly piezoresistive material on the opposite side can take advantage of larger strain values

For BC1-BC4 there must be a conductive path across the neutral axis to connect the left and right electrodes. There will always be some piezoresistive elements on both sides of the neutral axis in the current path, resulting in some canceling of peizoresistivity. Additionally, the formation of the conductive path across the neutral axis forces material towards the center of the cross section, which is sub-optimal for strain energy maximization.

This competing relationship between stiffness and resistance change can be partially decoupled by placing the electrodes on one side of the neutral axis, as per BC5 and BC6. In these cases all of the highly piezoresistive elements that form the conductive path are located on one side of the neutral axis. Adding the stiff elements on the opposite side, the right edge in the topologies shown, moves the neutral axis in that direction without it detracting from the summed piezoresistive contributions. This also improves strain energy performance by allowing the design to form a conductive path while maintaining a sandwich beam topology.

Figure 4.13 helps to further illustrate this behavior by plotting the local resistivity change due to strain along with a vector plot to show the conductive path for the best sensing topologies with two different electrode configurations: BC1 and BC6. The red and green colormap shows positive and negative piezoresistive contributions, respectively. Elements within the conductive path will contribute to the resistance change objective. While there is a band of red elements in right topology shown in Figure 4.13, these elements do not fall in the conductive path and do not detract from the sensing performance. Conversely, in the left topology the conductive path flows from left to right, and there will be some subtractive contribution from the red elements. As a result, BC6.2.3 has nearly double the sensing performance and still offers an improvement in stiffness over BC1.2.3.

The influence of boundary condition is also evident when comparing points BC1.2.1 and BC4.2.1 to BC5.2.1 and BC6.2.1, in which all designs are able to obtain the same strain energy value. BC1 and BC4 must sacrifice the formation of a conductive path between their left and right electrodes and any asymmetry along this path to obtain the strain energy value. BC5 and BC6 form a conductive path to their top and bottom electrodes while still moving stiff material away from the neutral axis. These designs are able to produce equivalent strain energy values with orders of magnitude higher resistance change values, underscoring the importance of boundary condition and prompting the question of whether it is of benefit to also optimize the electrode placement alongside the topology.

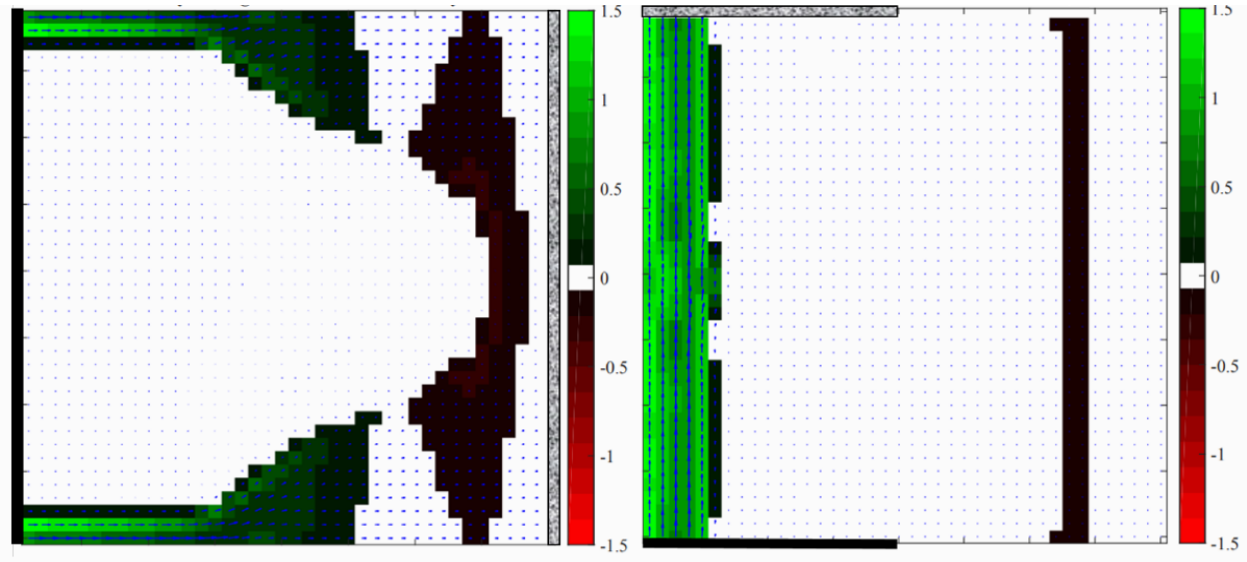

Figure 4.13: Comparing local piezoresistive contributions for BC1.2.3 (left) and BC6.2.3 (right). Colormap shows signed change in local resistivity due to strain. Vector plot shows the conductive path. Black and grey bars mark the electrodes.

Strain Energy and Resistance Change Optimization with a Four Percent Global Volume Fraction Constraint

Plotting Pareto Fronts for the 4% global volume fraction case in Figure 4.14 shows that the relaxation of the volume fraction constraint from 2% to 4 % nearly doubles the maximum strain energy. In designs where strain energy is maximized the optimal topology uses all available material and places this material as far from the neutral axis as possible.

By examining BC1.4.2 and BC4.4.2 in Figure 4.15 it is again shown to be beneficial to have more elements near 2% volume fraction on one side of the neutral axis. The two designs have the same strain energy value but BC4.4.2 has a 15 % greater resistance change. Due to the electrode placement even BC4.4.2 must form a conductive path across the neutral axis and suffer some loss of sensing, which is observed by comparing this topology to BC5.4.2. Both have similar amounts of piezoresistive elements far from the neutral axis and both have similar amounts of stiff material on the right side of the cross section. However BC5.4.2 does not have to form a conductive path from left to right, and does not accumulate a negative piezoresitive contribution from the right half of the cross-section. As a result it maintains the same strain energy as BC4.4.2 but has a 33 % increase in the resistance change.

These results reinforces the idea that for designs where high strain energy is important the amount of CNT available drives the performance. For designs where resistance change is important the selection of boundary condition is just as significant, if not more so, than the amount of CNT used.

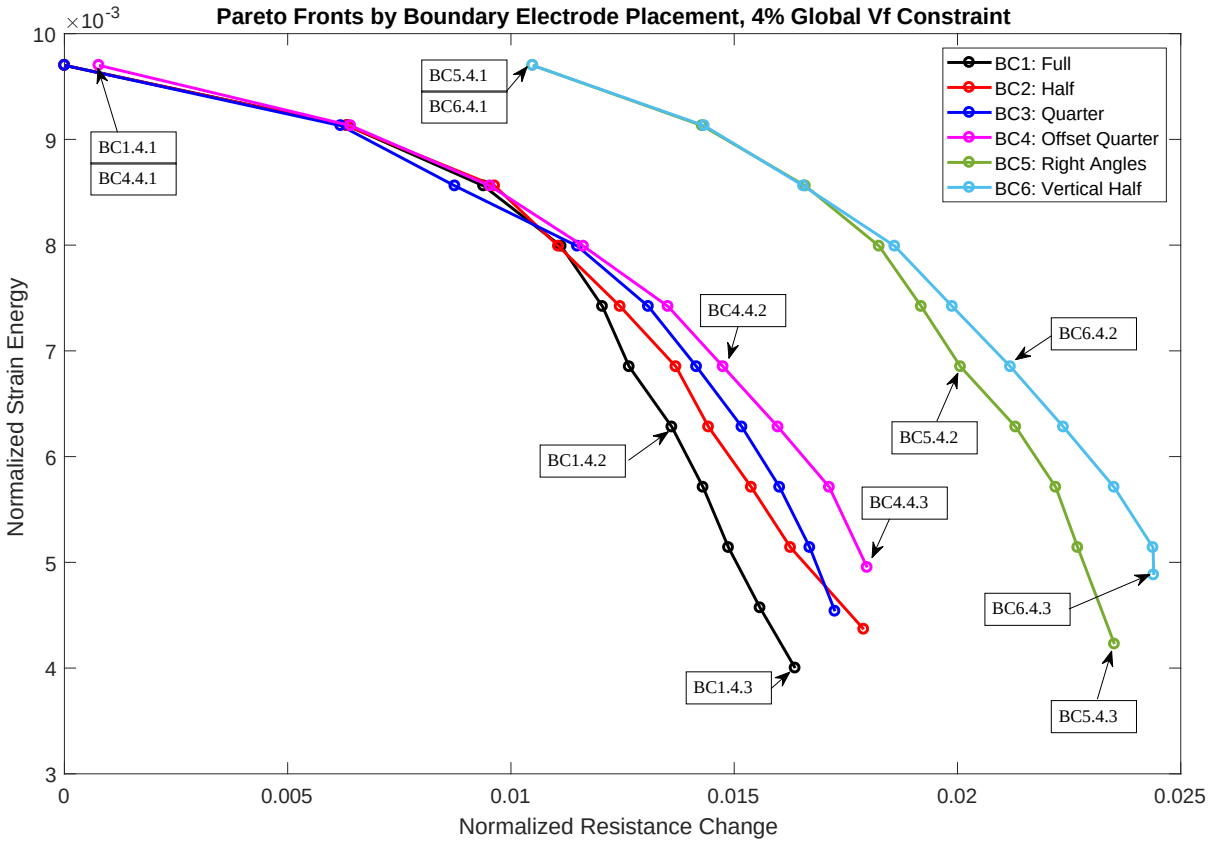

Figure 4.14: Pareto Fronts with labeled nondominated points. 4% global VF constraint

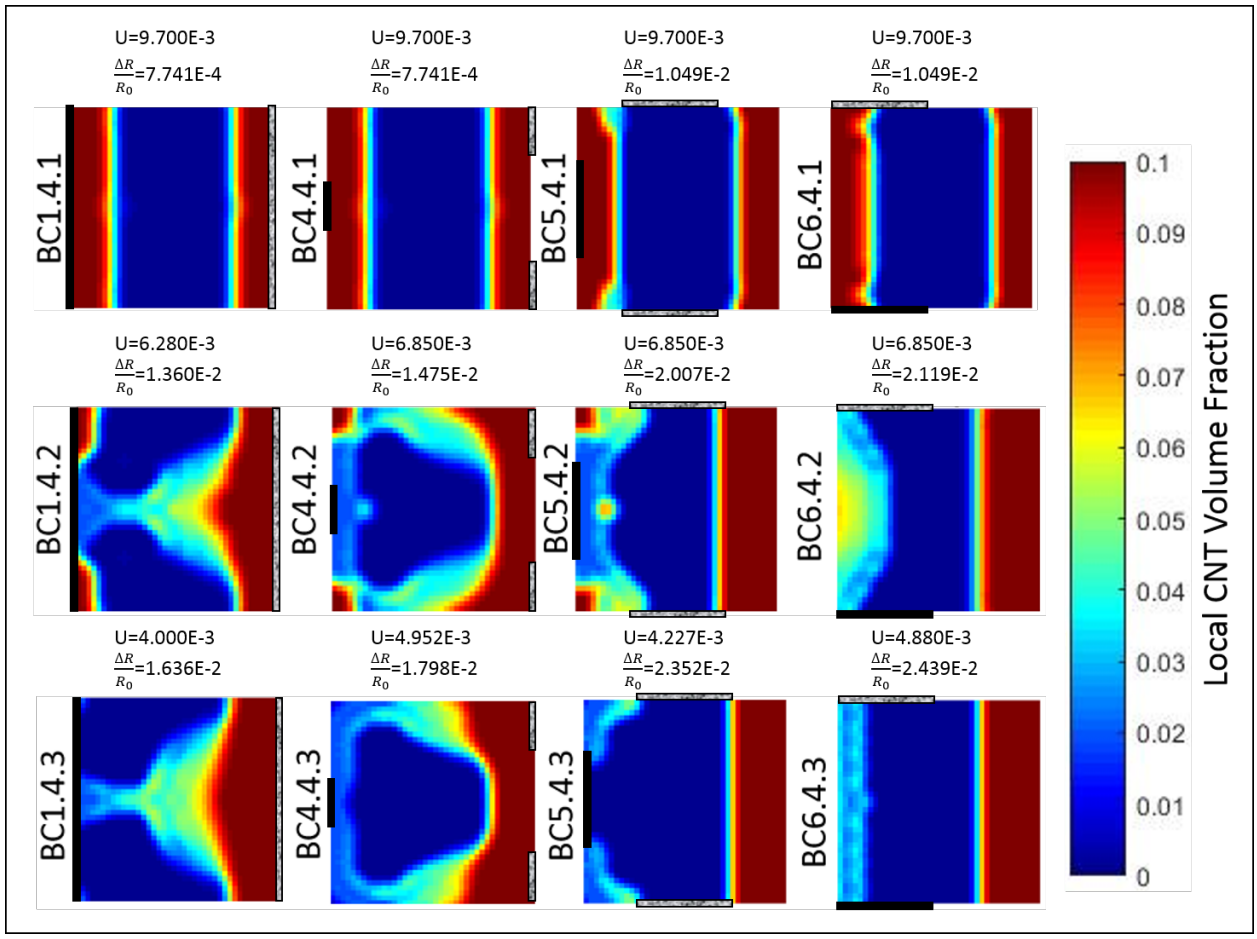

Figure 4.15: Comparing topologies with a 4 percent volume fraction constraint.

Strain Energy and Resistance Change Optimization without a Global Volume Fraction Constraint

The unconstrained results are shown in Figures 4.16 and 4.17. The removal of the global volume fraction constraint provides a 25.7 % increase in the normalized strain energy when compared to the 4% constraint solutions. As the strain energy constraint is relaxed and optimal topologies provide higher resistance change values, the total CNT volume fraction decreases. BC6.10.3, the topology with the largest resistance change, uses less than 4% CNT. This topology very closely matches BC6.4.3, and shows that allowing a design to use additional CNT beyond 4% does not improve the resistance change.

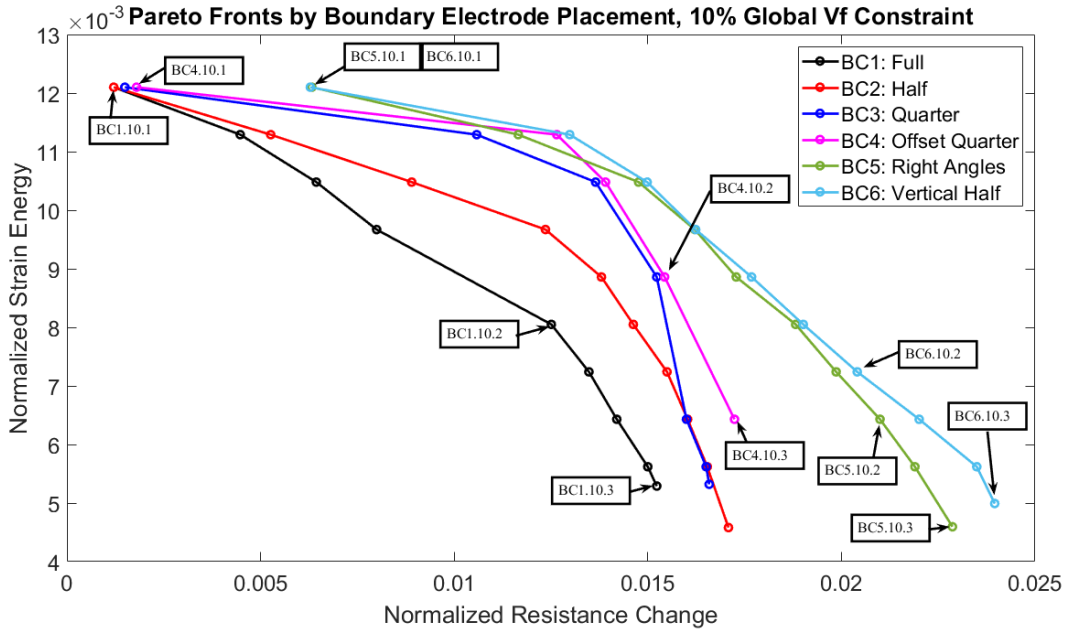

Figure 4.16: Pareto Fronts with labeled nondominated points for no global volume fraction constraint

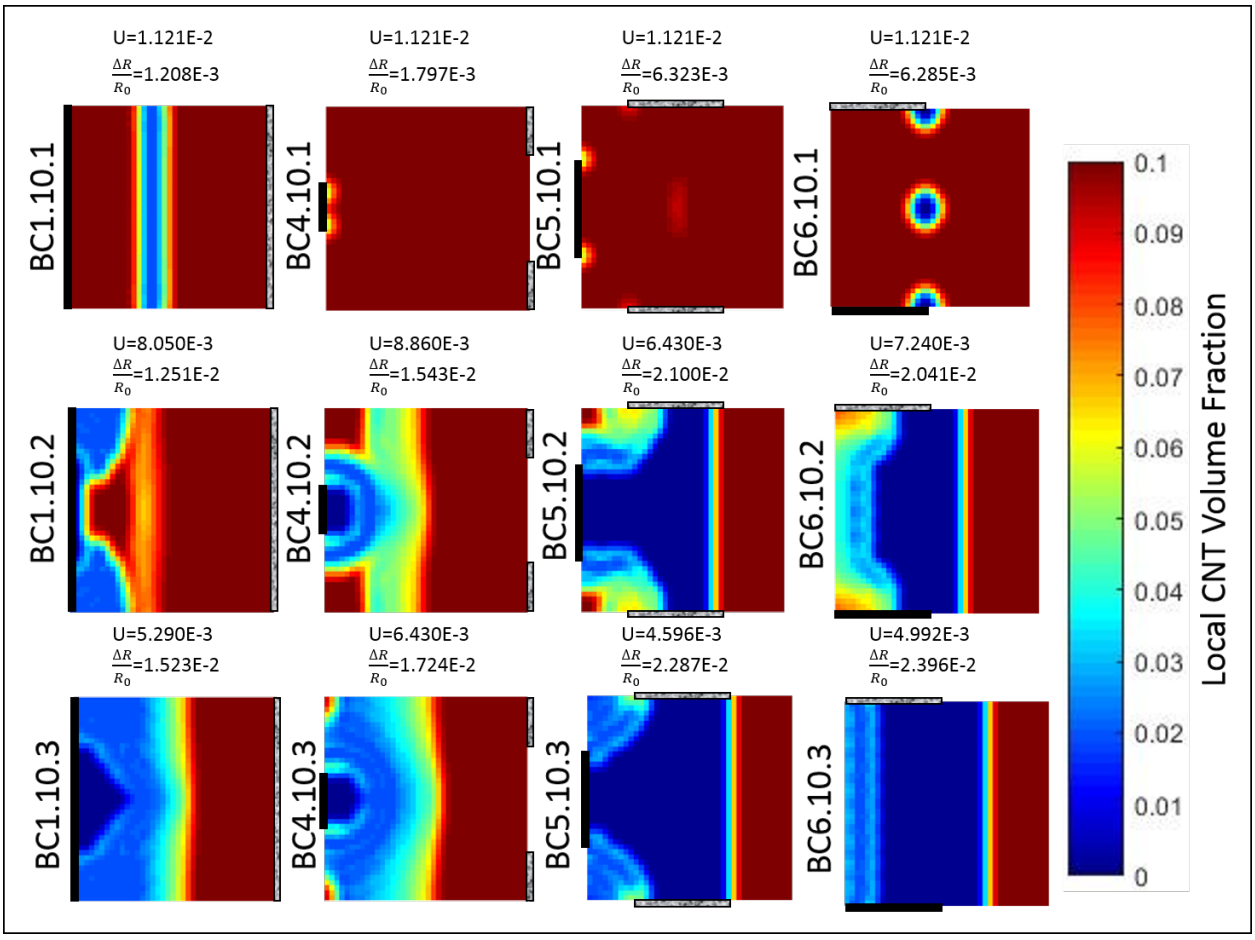

Figure 4.17: Comparing topologies without a volume fraction constraint.

As adding CNT will always improve stiffness, global optima for single objective stiffness maximization (BC1.10.1-BC6.10.1) would be a solid red cross-section. Due to the epsilon-constraint implementation, a small relaxation of this globally optimal U^* is used to aid in convergence. As such, some of the topologies, such as BC1.10.1 and BC6.10.1 do not converge to an all-red design, as they are trying to maximize sensing with the small amount of freedom they have to do so.

Comparing Results Across All Constraint Values

A final summary of the results is presented in Figure 4.18. The boundary conditions are sorted by line and marker color, and the volume fractions constraints are sorted by marker shape, with the 2% volume fraction constraint solutions being marked by circles, the 4% solutions being marked by triangles, and the unconstrained solutions marked by squares.

Allowing the cross-section to use more CNT generally results in better solutions. For a

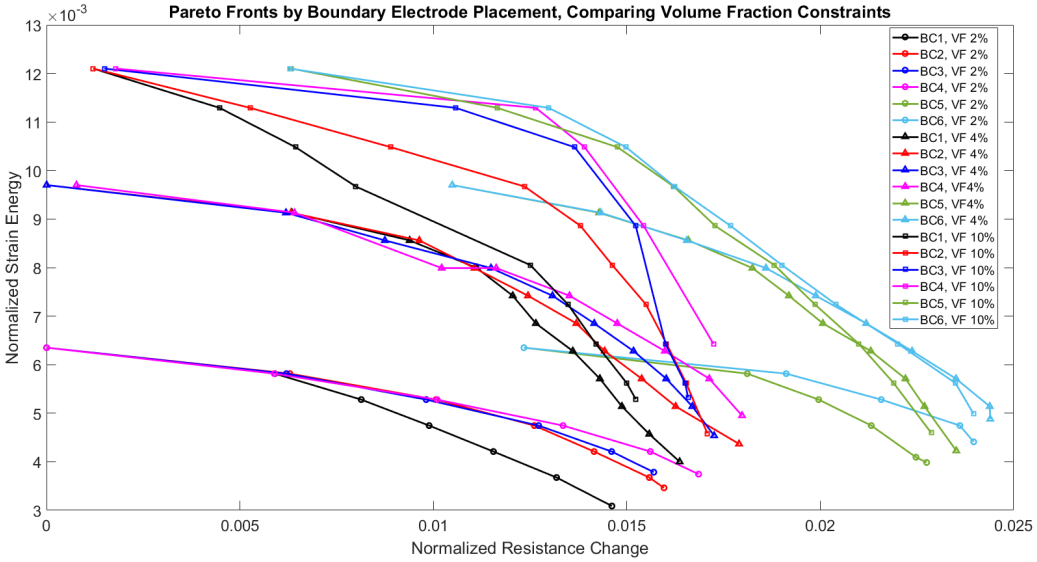

Figure 4.18: Comparing Pareto Fronts across different volume fractions and boundary conditions

given boundary condition all of the 4% Pareto Fronts dominate their 2% counterparts, and unconstrained solutions dominate both the 2% and 4% solutions, except in areas where the strain energy constraint is inactive. As the strain energy constraint is relaxed, the advantage of being able to use more material diminishes. Table 4.3 shows objective values against total volume fraction used for a set of the unconstrained optimal topologies. When large strain energies are required by the constraint, the optimal solution uses all of the available material for the highest attainable strain energy. It is only the slight relaxation of the epsilon-constraint value that prevents all of the top row topologies in Figure 4.17 from forming all-red designs. When the strain energy constraint is relaxed and resistance change increases, the optimal solution uses less CNT, down to less than 4% for the highest resistance change values. Thus, for cases where resistance change is maximized the 4% constraint is inactive, and the 4% and unconstrained results are different local minima for the same problem that result in variations of the random starting conditions.

4.3 Conclusions of Optimization of a Multifunctional Beam Cross-Section

Topology optimization was used to determine the best placement of CNT within an epoxy matrix for a beam cross-section. The beam was subject to either a prescribed twisting or a prescribed bending curvature. Electrical conductivity and piezoresistivity were measured

Table 4.3: Total volume fraction vs optimized resistance change and strain energy. Best performers in each objective are highlighted.

ID	Global VF Used	Norm. Strain Energy	Norm. Resistance Change
1.10.1	9.38%	$1.210E{-}2$	$1.208E{-}3$
1.10.2	7.96%	$8.050E{-}3$	$1.251E{-}2$
1.10.3	5.76%	$5.290E{-}3$	$1.523E{-}2$
4.10.1	9.96%	$1.210E{-}2$	$1.797E{-}3$
4.10.2	7.58%	$8.860E{-}3$	$1.543E{-}2$
4.10.3	6.02%	$6.430E{-}3$	$1.724E{-}2$
5.10.1	9.95%	$1.210E{-}2$	$6.323E{-}3$
5.10.2	4.50%	$6.430E{-}3$	$2.100E{-}2$
5.10.3	3.42%	$4.596E{-}3$	$2.287E{-}2$
6.10.1	9.53%	$1.210E{-}2$	$6.285E{-}3$
6.10.2	4.81%	$7.240E{-}3$	$2.041E{-}2$
6.10.3	3.43%	$4.992E{-}3$	$2.396E{-}2$

across fixed electrodes. Micromechanics models were used to relate the element CNT volume fraction to local stiffness, resistivity, and piezoresistivity. These local properties were then used to obtain global performance objectives; torsional rigidity, electrical conductivity, strain energy, and resistance change due to strain. Analytic sensitvities were derived for the objectives and used in a gradient-based sequential quadratic programming optimization scheme. This scheme was used to solve two separate optimization problems.

First, a twisting beam was optimized for maximum torsional rigidity and maximum conductivity between the electrodes. A Pareto Front of nondominated points was used to illustrate performance trade-offs of the objectives, and each nondominated point marked the performance of a corresponding optimized topology. It was shown that it was possible to obtain relatively good conductivity while maintaining a large percent of the max attainable torsional rigidity. Only when a very high amount of conductivity was required did the optimal topology shift away from an 'embedded tube' type of design. It was shown that the weighted-sum method did not always provide evenly mapped Pareto Fronts, but that for sufficiently smooth Pareto Fronts the method gave a good balance of a mapped objective space and reasonably low computational cost.

The second problem introduced electromechanical coupling via a piezoresistive effect. A restart method from the previous chapter was used to solve the multiobjective topology optimization problems with several minima. The method used a two-step mesh refinement and several starting conditions to solve the problem. Six different boundary conditions and three different global volume fraction constraints were compared. The objective was to simultaneously optimize for strain energy and strain sensing.

It was found that relaxing the global volume fraction constraint directly improved strain

energy results. The optimal topology without a global volume fraction constraint has over ninety percent more strain energy than the optimal topology with a 2% global volume fraction constraint. In the case of the constant curvature beam, strain energy is maximized by placing high CNT volume fractions as far from the neutral axis as possible.

Relaxing the global volume fraction constraint to 4% also improved resistance change. However, removing the constraint altogether showed that the most optimal sensing topologies still stayed close to 4% global volume fraction. The topology that performed the best in sensing used 3.43% CNT and the vertical-half electrode configuration, i.e. BC6.10.3. For a given boundary condition resistance change is maximized via shifting the neutral axis, introducing piezoresistive asymmetry across the strain field, and forming a conductive path between the boundary electrodes. Placing the electrodes such that the conductive path does not have to cross the neutral axis leads to topologies that can have both good stiffness and good sensing.

In the following chapter these optimization methods are extended to a 2D structure. Also, it is clear from these results that the electrode boundary condition plays an important role in determining conductivity and sensing performance. Following the 2D optimization, a combined topology and boundary electrode optimization method is performed.

Chapter 5

Optimization of 2D Plane Stress Structures

The cross-section optimization in the previous chapter introduced an example of the coupled strain energy and resistance change mechanics. For the beam cross-section design, the strain energy was calculated using the analytic solution based on Euler-Bernoulli beam theory. The resistance change was calculated using finite elements to based on electrostatic PDE's. But it was assumed that only the axial strain component was significant. This is not the case for 2D plane-stress structures. In order to optimize these structures the methods developed in earlier chapters are extended to coupled analysis of mechanics and electrostatics where FEM analysis is used to solve both the mechanical and electrostatic PDE's. Two structures are optimized for maximum stiffness (min. strain energy) and sensing (max. resistance change) under a prescribed mechanical load and electric potential difference. First, the micromechancis equations are updated to capture the influence of the 2D strains on the resistivities. New objective equations for strain energy and resistance change are introduced, and a coupled adjoint method is used to obtain the sensitivities. The two different structures considered are a representative plate with a hole and a compact tension sample. These structures optimized at different global volume fraction constraints, and Pareto Fronts are used to relate the optimal performance in terms of stiffness and sensing.

5.1 Updating the Piezoresistive Micromechanics

For the beam-cross section piezoresistivity was assumed to be influenced only by the axial strain. As this is no longer the case, Equation 4.60 must be updated. Silva et al. [**?**] presented a matrix of piezoresistive constants for a 2D plate structure. An analog is adapted here as the piezoresistive matrix, $\bar{\boldsymbol{g}}$. It alters the resistivity as

$$\begin{bmatrix}\rho_1\\ \rho_2\\ \rho_6\end{bmatrix} = \left[\begin{bmatrix}1\\ 1\\ 0\end{bmatrix} + \begin{bmatrix}g_{11} & g_{12} & 0\\ g_{12} & g_{11} & 0\\ 0 & 0 & g_{66}\end{bmatrix}\begin{bmatrix}\epsilon_1\\ \epsilon_2\\ \gamma_6\end{bmatrix}\right]\rho_0 \tag{5.1}$$

In the current model there are potentially three different resistivities, related to the three strain components via the $\bar{\boldsymbol{g}}$ matrix. ρ_0 is the unstrained resistivity, $\boldsymbol{\epsilon}$ is the strain vector, and $\bar{\boldsymbol{g}}$ is the piezoresistive constant matrix. The resistivity values are used to assemble the element conductivity matrix. Here both ρ_0 and $\bar{\boldsymbol{g}}$ are explicit functions of the CNT volume fraction in a given element, v_e. It must be noted that this formulation follows [95] and [96] and assumes that the through-thickness strains i.e. ϵ_3, γ_4, and γ_5 are not significant. In the future it may be of interest to investigate piezoresisitivty for the full strain field, in which a 6 x 6 matrix of piezoresistive constants may be required to relate 6 resistivity components to 6 strain components.

The element conductivity matrix is used within the electrostatic finite element formulation. This matrix is given as $\hat{\boldsymbol{\sigma}}$ and is obtained via inversion of the resistivity matrix.

$$\hat{\boldsymbol{\rho}} = \begin{bmatrix}\rho_1 & \rho_6\\ \rho_6 & \rho_2\end{bmatrix} \tag{5.2}$$

$$\hat{\boldsymbol{\sigma}} = \hat{\boldsymbol{\rho}}^{-1} \tag{5.3}$$

The sensitivities of the conductivity matrix with respect to volume fraction must be obtained to calculate the sensitivity of the resistance change objective. These sensitivities are

$$\frac{d\bar{\boldsymbol{\sigma}}}{dv_e} = -\bar{\boldsymbol{\rho}}^{-1}\frac{d\bar{\boldsymbol{\rho}}}{dv_e}\bar{\boldsymbol{\rho}}^{-1} \tag{5.4}$$

and

$$\frac{\partial\rho_1}{\partial v_e} = \rho_0'(1 + g_{11}\epsilon_1 + g_{12}\epsilon_2) + \rho_0(g_{11}'\epsilon_1 + g_{12}'\epsilon_2) \tag{5.5}$$

$$\frac{\partial\rho_2}{\partial v_e} = \rho_0'(1 + g_{12}\epsilon_1 + g_{11}\epsilon_2) + \rho_0(g_{12}'\epsilon_1 + g_{11}'\epsilon_2) \tag{5.6}$$

$$\frac{\partial\rho_6}{\partial v_e} = \rho_0(g_{66}'\gamma_6) \tag{5.7}$$

g_{ii}' and ρ_0' indicate derivatives of the micromechanics equations with respect to the local volume fraction. In literature [19, 10] the shear terms of the CNT-polymer composite piezoresistivity were seen to be small, and thus for the representative model used herein it is assumed

that $g_{11} = g_{12} = g$ and $g_{66} = 0$, where g is provided via Equation 4.5. Of course, if the design tool were to be applied to a manufactured CNT-polymer composite, it would be important to first characterize the specific material system to obtain a system-specific $\bar{\boldsymbol{g}}$.

5.2 Updating the Analysis and Sensitivity of the Objectives

As opposed to the cross-section analysis, the 2D optimization uses finite element models for the mechanics in place of analytic Euler-Bernoulli equations. The strain energy sensitivity is formulated using the self-adjoint method, similar to the torsional rigidity sensitivity in Section 4.1.2. A coupled adjoint method is used to obtain the sensitivities of the resistance change.

5.2.1 Objective Function: Strain Energy of 2D Plane Stress Structures

For the beam cross-section the strain energy was computed by solving discretized forms of cross-section analysis based on Euler-Bernoulli assumptions to obtain bending rigidities. These rigidities were then multiplied by the curvatures. A finite element model is now incorporated to solve the 2D mechanical problem of a 2D structure with a prescribed force loading. The topic of 2D plane stress finite elements is well studied [97, 98].

This problem is solved using 4 node quadrilateral elements, similar to those used to solve for torsional rigidity and electric current in the previous chapter. Each of the 4 nodes has two degrees of freedom, u_x and u_y. The element equilibrium equation for the 2D mechanics is

$$\boldsymbol{K}_e(v_e)\boldsymbol{u}_e = \boldsymbol{f}_e \tag{5.8}$$

$\boldsymbol{K}_e$ is the element stiffness matrix, v_e the element CNT volume fraction, $\boldsymbol{u}_e$ the element displacement vector, and $\boldsymbol{f}_e$ the element load vector. The CNT volume fractions affect the stiffness matrix by modifying the constitutive matrix, $\boldsymbol{D}_e$.

$$\boldsymbol{D}_e(v_e) = E_e(v_e)\begin{bmatrix} E_{mod} & \nu E_{mod} & 0 \\ \nu E_{mod} & E_{mod} & 0 \\ 0 & 0 & G_{mod} \end{bmatrix} \tag{5.9}$$

Where constants $E_{mod} = \dfrac{1}{1-\nu^2}$ and $G_{mod} = \dfrac{1}{2(1+\nu)}$. Using the 4 shape functions from Equation 4.11, the strain displacement matrix is

$$\boldsymbol{B}_k = \begin{bmatrix} \frac{\partial N_1^e}{\partial \xi} & 0 & \frac{\partial N_2^e}{\partial \xi} & 0 & \frac{\partial N_3^e}{\partial \xi} & 0 & \frac{\partial N_4^e}{\partial \xi} & 0 \\ 0 & \frac{\partial N_1^e}{\partial \eta} & 0 & \frac{\partial N_2^e}{\partial \eta} & 0 & \frac{\partial N_3^e}{\partial \eta} & 0 & \frac{\partial N_4^e}{\partial \eta} \\ \frac{\partial N_1^e}{\partial \eta} & \frac{\partial N_1^e}{\partial \xi} & \frac{\partial N_2^e}{\partial \eta} & \frac{\partial N_2^e}{\partial \xi} & \frac{\partial N_3^e}{\partial \eta} & \frac{\partial N_3^e}{\partial \xi} & \frac{\partial N_4^e}{\partial \eta} & \frac{\partial N_4^e}{\partial \xi} \end{bmatrix} \tag{5.10}$$

The element stiffness matrix is then

$$\boldsymbol{K}_e = \int_\xi \int_\eta \boldsymbol{B}_k^T \boldsymbol{D}_e \boldsymbol{B}_k |\boldsymbol{J}_e| d\xi d\eta \tag{5.11}$$

and is computed for each element and assembled into a global stiffness matrix. Boundary conditions are applied that specify which u_x and u_y are set to 0, and the problem is solved for the remaining displacements. The strain energy is

$$U = \frac{1}{2} \boldsymbol{u}^T \boldsymbol{K} \boldsymbol{u} \tag{5.12}$$

and the sensitivity of the strain energy is given via self-adjoint solution in the originial SIMP method paper by Sigmund and Bendsoe [2, 52]. Note the similarity to the sensitivity of the torsional rigidity obtained for the beam cross-section in Equation 4.18.

$$\frac{\partial U}{\partial v_e} = -\frac{1}{2} \boldsymbol{u}_e^T \frac{\partial \boldsymbol{K}_e}{\partial v_e} \boldsymbol{u}_e \tag{5.13}$$

The sensitivity of the stiffness matrix is dependent only on the sensitivity of the constitutive matrix.

$$\frac{\partial \boldsymbol{K}_e}{\partial v_e} = \int_\xi \int_\eta \boldsymbol{B}_k^T \frac{\partial \boldsymbol{D}_e}{\partial v_e} \boldsymbol{B}_k |\boldsymbol{J}_e| d\xi d\eta \tag{5.14}$$

And as the element Young's modulus has been factored out of D_e the sensitivity may be easily computed.

$$\frac{\partial \boldsymbol{D}_e}{\partial v_e} = \frac{\partial E_e}{\partial v_e} \begin{bmatrix} E_{mod} & \nu E_{mod} & 0 \\ \nu E_{mod} & E_{mod} & 0 \\ 0 & 0 & G_{mod} \end{bmatrix} \tag{5.15}$$

5.2.2 Resistance Change

The resistance change analysis detailed in Section 4.1.5 still holds for the 2D piezoresistive problem so long as the updated micromechanics are implemented via Section 5.1. The sensitivity must now be altered to reflect these changes. Previously, the coupling component of the sensitivity was captured by substituting the sensitivity of the strain field to volume fraction changes into the resistivity sensitivity via a chain rule, as per Equation 4.62. Now that the mechanical analysis is performed via finite elements, a coupled adjoint sensitivity may be derived.

Martins and Hwang laid out general forms of coupled adjoint sensitivities, which are adapted for the sensitivity of the coupled piezoresistive problem [99]. The equilibrium equations are labeled $R_1 = \boldsymbol{K}\boldsymbol{u} - \boldsymbol{f}$ and $R_2 = \boldsymbol{C}\boldsymbol{\phi} - \boldsymbol{I}$. The objective functions are $F_1 = U$ for strain energy and $F_2 = I_{bc}$ for the strained current out of the boundary electrode. The strained current is considered here as it is the term in the resistance change that includes the coupling. In matrix form

$$\boldsymbol{R} = \begin{bmatrix} R_1(\boldsymbol{v}, \boldsymbol{u}) \\ R_2(\boldsymbol{v}, \boldsymbol{u}, \boldsymbol{\phi}) \end{bmatrix} \tag{5.16}$$

$$\boldsymbol{F} = \begin{bmatrix} F_1(\boldsymbol{v}, \boldsymbol{u}) \\ F_2(\boldsymbol{v}, \boldsymbol{u}, \boldsymbol{\phi}) \end{bmatrix} \tag{5.17}$$

The goal is to determine the sensitivity of $\boldsymbol{F}$ with respect to a change the design variable, v_e. The total derivative is given as

$$\frac{d\boldsymbol{F}}{dv_e} = \frac{\partial \boldsymbol{F}}{\partial v_e} + \frac{\partial \boldsymbol{F}}{\partial \boldsymbol{y}} \frac{\partial \boldsymbol{y}}{\partial v_e} \tag{5.18}$$

where $\boldsymbol{y}$ is the state variable vector $\boldsymbol{y} = [\boldsymbol{u}, \boldsymbol{\phi}]$. The derivatives of the equilibrium equations are

$$\frac{d\boldsymbol{R}}{dv_e} = 0 = \frac{\partial \boldsymbol{R}}{\partial v_e} + \frac{\partial \boldsymbol{R}}{\partial \boldsymbol{y}} \frac{\partial \boldsymbol{y}}{\partial v_e} \tag{5.19}$$

which can be solved for $\dfrac{\partial \boldsymbol{y}}{\partial v_e}$. For direct sensitivity analysis $\dfrac{\partial \boldsymbol{y}}{\partial v_e}$ can be substituted into the equation above to compute the sensitivity of the objective functions.

In the adjoint method, the total derivative is reformulated to instead include the sensitivity of the residuals multiplied by the adjoint variable $\boldsymbol{\lambda}$.

$$\frac{d\boldsymbol{F}}{dv_e} = \frac{\partial \boldsymbol{F}}{\partial v_e} - \boldsymbol{\lambda}^T \frac{\partial \boldsymbol{R}}{\partial v_e} \tag{5.20}$$

$\boldsymbol{\lambda}$ is obtained through the solution of the adjoint equation in Equation 5.21

$$-\frac{\partial \boldsymbol{R}}{\partial \boldsymbol{y}}^T \boldsymbol{\lambda} = \frac{\partial \boldsymbol{F}}{\partial \boldsymbol{y}}^T \tag{5.21}$$

For the mechanical and electrostatic coupled problem this equation expands to

$$-\begin{bmatrix} \boldsymbol{R}_{1,u}^T & \boldsymbol{R}_{2,u}^T \\ \boldsymbol{R}_{1,\phi}^T & \boldsymbol{R}_{2,\phi}^T \end{bmatrix} \begin{bmatrix} \boldsymbol{\lambda}_{uu} & \boldsymbol{\lambda}_{u\phi} \\ \boldsymbol{\lambda}_{\phi u} & \boldsymbol{\lambda}_{\phi\phi} \end{bmatrix} = \begin{bmatrix} \boldsymbol{F}_{1,u} & \boldsymbol{F}_{2,u} \\ \boldsymbol{F}_{1,\phi} & \boldsymbol{F}_{2,\phi} \end{bmatrix} \tag{5.22}$$

where the subscript , u and , ϕ indicate derivatives of the residuals and objectives with respect to that state variable. If only the strained current sensitivity is required (as the strain energy sensitivity has been solved via self-adjoint), this reduces to

$$-\begin{bmatrix} \boldsymbol{R}_{1,u}^T & \boldsymbol{R}_{2,u}^T \\ \boldsymbol{R}_{1,\phi}^T & \boldsymbol{R}_{2,\phi}^T \end{bmatrix} \begin{bmatrix} \boldsymbol{\lambda}_{u\phi} \\ \boldsymbol{\lambda}_{\phi\phi} \end{bmatrix} = \begin{bmatrix} \boldsymbol{F}_{2,u} \\ \boldsymbol{F}_{2,\phi} \end{bmatrix} \tag{5.23}$$

Similarly, partitioning Equation 5.20 to only consider the strained current objective results in an updated version of Equation 4.55, which gave the sensitivity of the strained current. It now includes a coupling term.

$$\frac{dF_2}{dv_e} = -\boldsymbol{\lambda}_{u\phi}^T \frac{\partial \boldsymbol{K}}{\partial v_e}\boldsymbol{u} - \boldsymbol{\lambda}_{\phi\phi}^T \frac{\partial \boldsymbol{C}}{\partial v_e}\boldsymbol{\phi} \tag{5.24}$$

The adjoint variables and the sensitivities of the stiffness and condutivity matrices to volume fraction changes must now be obtained. The sensitivities of the residuals with respect to the states are

$$\boldsymbol{R}_{1,u} = \frac{\partial(\boldsymbol{K}\boldsymbol{u} - \boldsymbol{f})}{\partial \boldsymbol{u}} = \boldsymbol{K} \tag{5.25}$$

$$\boldsymbol{R}_{2,u} = \frac{\partial(\boldsymbol{C}\boldsymbol{\phi} - \boldsymbol{I})}{\partial \boldsymbol{u}} = \frac{\partial \boldsymbol{C}}{\partial \boldsymbol{u}}\boldsymbol{\phi} \tag{5.26}$$

$$\boldsymbol{R}_{1,\phi} = \boldsymbol{0} \tag{5.27}$$

$$\boldsymbol{R}_{2,\phi} = \frac{\partial(\boldsymbol{C}\boldsymbol{\phi} - \boldsymbol{I})}{\partial \boldsymbol{\phi}} = \boldsymbol{C} \tag{5.28}$$

The sensitivites of the objectives with respect to the states are

$$\begin{bmatrix} \boldsymbol{F}_{2,u} \\ \boldsymbol{F}_{2,\phi} \end{bmatrix} = \begin{bmatrix} \dfrac{\partial I_{bc}}{\partial \boldsymbol{u}} \\ \dfrac{\partial I_{bc}}{\partial \boldsymbol{\phi}} \end{bmatrix} \tag{5.29}$$

$$\frac{\partial I_{bc}}{\partial \boldsymbol{u}} = \frac{\partial \boldsymbol{p}^T \boldsymbol{\phi}}{\partial \boldsymbol{u}} \tag{5.30}$$

$$\frac{\partial I_{bc}}{\partial \boldsymbol{\phi}} = \boldsymbol{p}^T \tag{5.31}$$

So the adjoint equation is reposed as

$$-\begin{bmatrix} \boldsymbol{K}^T & \left(\dfrac{\partial \boldsymbol{C}}{\partial \boldsymbol{u}}\boldsymbol{\phi}\right)^T \\ \boldsymbol{0}^T & \boldsymbol{C}^T \end{bmatrix} \begin{bmatrix} \boldsymbol{\lambda}_{u\phi} \\ \boldsymbol{\lambda}_{\phi\phi} \end{bmatrix} = \begin{bmatrix} \dfrac{\partial \boldsymbol{q}^T \boldsymbol{\phi}}{\partial \boldsymbol{u}} \\ \boldsymbol{q}^T \end{bmatrix} \tag{5.32}$$

As $\boldsymbol{p} = \boldsymbol{q}^T \boldsymbol{C}$, and $\boldsymbol{q}$ is just a selection vector of 1's and 0's, the only remaining term to solve is $\boldsymbol{R}_{2,u}$ in Equation 5.26.

This may be computed on an element-wise basis and then assembled into a global sensitivity matrix, similar to the finite element assembly of the stiffness and conductivity matrices. For an element e

$$\frac{\partial R_2}{\partial \boldsymbol{u}_e} = \tilde{\boldsymbol{B}}_e \bar{\boldsymbol{j}}_e \boldsymbol{D}_e \tag{5.33}$$

where

$$\tilde{\boldsymbol{B}}_e = -\boldsymbol{B}_{\boldsymbol{e}}^T \hat{\boldsymbol{\sigma}}_e \tag{5.34}$$

and

$$\bar{\boldsymbol{j}}_e = \begin{bmatrix} j_{1e} & 0 & j_{2e} \\ 0 & j_{2e} & j_{1e} \end{bmatrix} \tag{5.35}$$

where the the j_e vector has 2 components, via

$$\boldsymbol{j}_e = \hat{\boldsymbol{\sigma}}_e \boldsymbol{B}_e \boldsymbol{\phi}_e |\boldsymbol{J}_e| \tag{5.36}$$

and

$$\boldsymbol{D}_e = \rho_{0e}\bar{\boldsymbol{g}}_e\boldsymbol{B}_{ke} \tag{5.37}$$

ρ_{0e} is the local unstrained resistivity, $\bar{\boldsymbol{g}}_e$ is the local piezoresistive matrix, $\boldsymbol{B}_{ke}$ is the element strain-displacement matrix, $\boldsymbol{B}_e$ is the element electrostatic-gradient matrix (the electrostatic analog to the strain-displacement matrix), $\hat{\boldsymbol{\sigma}}_e$ is the element conductivity matrix, and $|\boldsymbol{J}|_e$ is the determinant of the element Jacobian.

All terms to solve the adjoint state equation have now been derived. The only remaining terms in Equation 5.24 are the sensitivities of the stiffness and conductivity matrices with respect to local volume fractions. The sensitivity of the stiffness matrix is given via Equation 5.14 and the sensitivity of the conductivity matrix is given via Equation 4.48 with the updated 2D micromechanics sensitivities from Section 5.1.

Both strained current sensitivity and strain energy sensitivity are verified against a forward finite difference with a step size of $1e-6$. A test mesh of 492 elements is used, each with a random design variable value. Figure 5.1 shows that the analytic sensitivities agree with the finite difference sensitivities for both the strain energy and the current with the strain coupling.

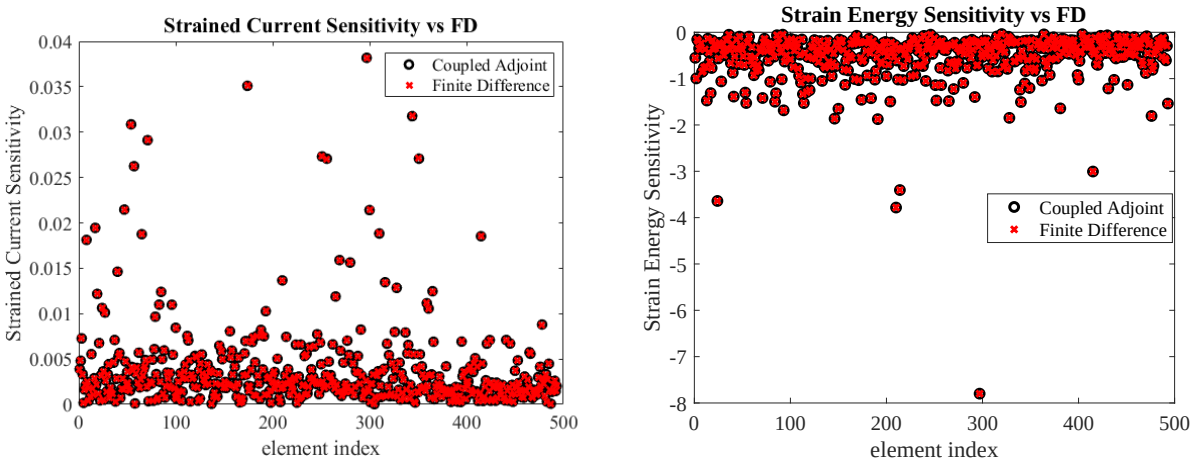

Figure 5.1: Left: Sensitivity Verification of the Strained Current. Right: Sensitivity Verification of the Strain Energy.

5.3 Results: 2D Plane Stress Structures

Two test cases are considered for stiffness and strain sensing optimization. The first test case is a representative plate with hole structure and the second test case is a compact

tension sample. The plate with a hole structure uses a symmetry boundary condition. It is constrained in the horizontal direction along the left edge, and in the vertical direction along the bottom edge. A uniform vertical load is applied along the top edge. Electrodes are placed along the inner curved edge and along the vertical right edge. The compact tension sample is loaded via equal and opposite vertical loads applied at the pin holes, and is fixed at the bottom corner and constrained in the horizontal direction at the top corner. These fixed degrees of freedom have zero reactions, and are only in place to prevent unconstrained displacements and rotations. For this structure the electrodes are placed along the top and bottom edges. The design spaces for both structures are shown in Figure 5.2.

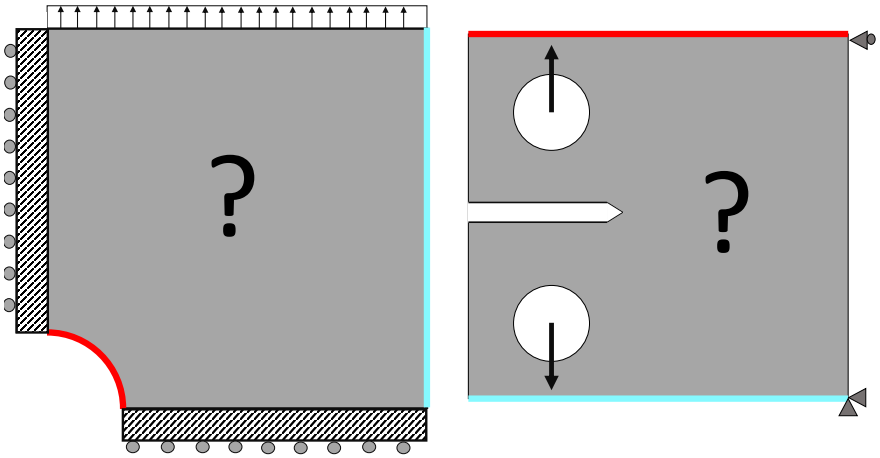

Figure 5.2: Design space for the 2D plane stress structures. Left: Plate w/Hole. Right: Compact Tension. Electrodes are marked via red and blue lines.

The coupled optimization is performed using the epsilon-constraint method introduced in Equation 4.66. Single objective optimization with a uniform CNT distribution is used to obtain utopia points that inform the bounds on the strain energy epsilon-constraint. Global volume fractions of 2% and 5% are considered, as well as a case without a global volume fraction constraint. For each structure presented, a 5% uniform CNT distribution is shown alongside some relevant metrics; volumetric strain, electric potential, and local resisitivity change. Then the Pareto Fronts for the three volume fraction cases are presented, in which the performance of a comparative uniform distribution is marked. From there, best stiffness and best sensing topologies are examined. Select Pareto Optimal topologies are shown for the 5% case, illustrating how the design changes as the strain energy epsilon-constraint is relaxed. Finally, the optimal sensing structure for the 5% volume fraction constraint is compared to the same optima for a case where the physics is uncoupled via a fixed strain field, i.e. all $E_e = .05E^{CNT} + .95e^{mat}$ and all $\frac{dE_e}{dv_e} = 0$. This helps to show the importance of including the coupled physics in the design.

5.3.1 Optimization of the Plate with a Hole

The topology, volumetric strain field, electric potential field, and the local resistivity change field for this structure with a uniform 5% volume fraction distribution are shown in Figure 5.3. The red and blue bars in the electric potential plot mark the locations of the electrodes. The electrode configuration presented here is used for all of the plate with a hole results in this section.

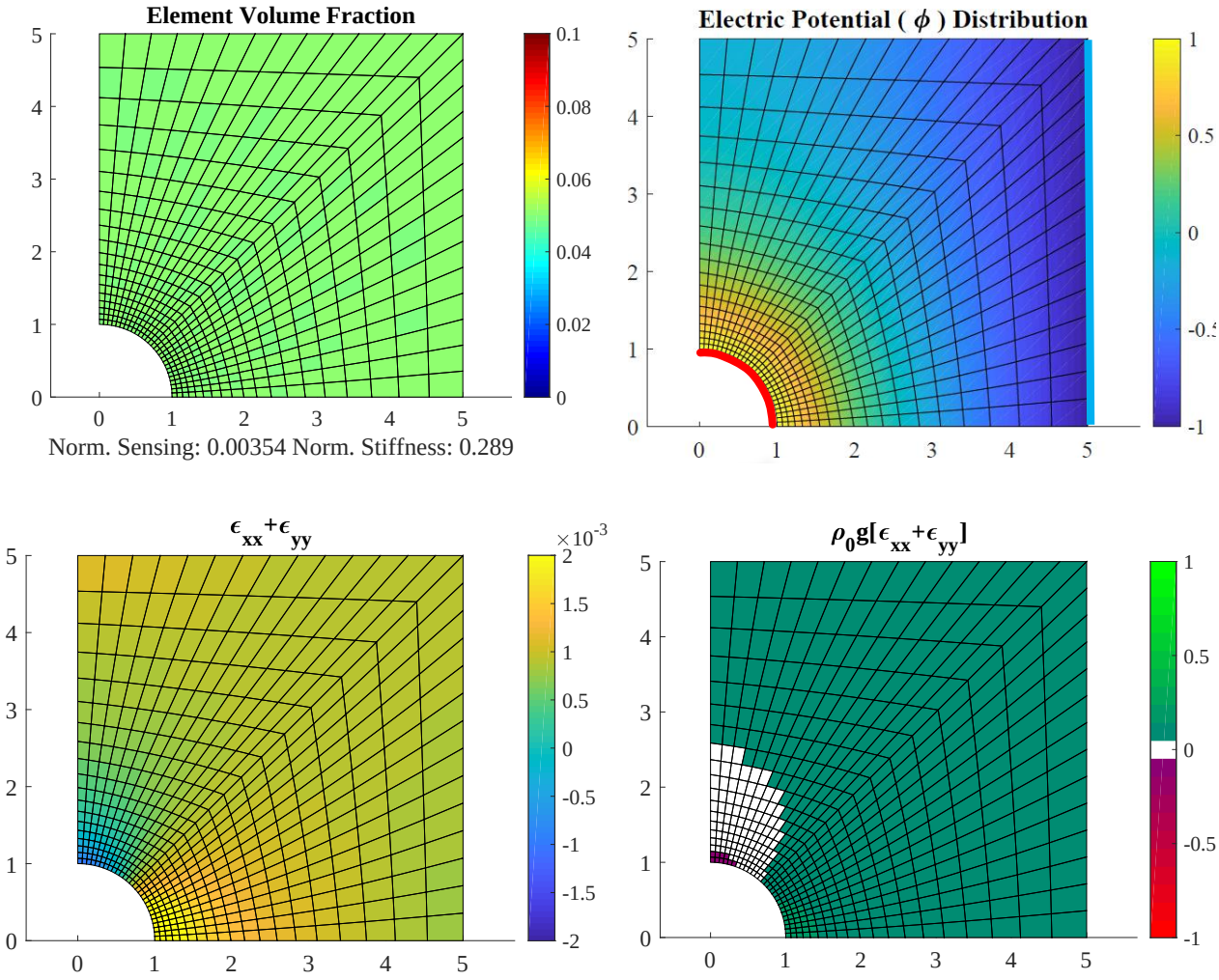

Figure 5.3: Top Left:Uniform Topology w/ Sensing and Strain Energy Performance. Top Right: Electric Potential Distribution. Red and Blue bars indicate electrodes. Bottom Left: Volumetric Strain, assuming $\epsilon_3 = 0$. Bottom Right: Resistivity Change due to Strain

Here it is seen that there is a strain concentration at the lower right edge of the hole, and a net-negative volumetric strain region at the top edge of the hole. These locations are likely to be important in both the stiffness and sensing optimizations. As the electrode runs along

this curved edge (which can be seen by the yellow band in the electric potential plot), it will be up to the optimizer to form conductive paths in this region in the best way possible.

Pareto Fronts for the plate with a hole are plotted in Figure 5.4. The top left subplot compares Pareto Fronts across all three constraint cases, and the remaining plots isolate a single constraint case.

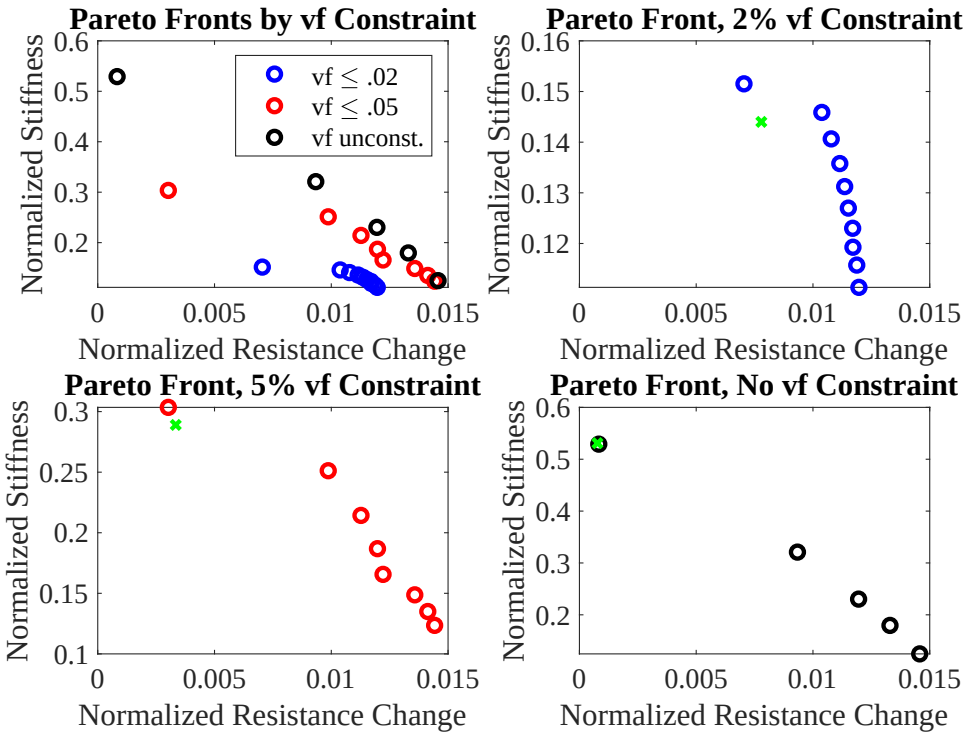

Figure 5.4: Pareto Fronts across global volume fraction constraints for the plate w/hole. Green x used to mark uniform CNT distribution performance.

In Figure 5.4 the vertical axis marks the stiffness performance and the horizontal axis marks the sensing performance, with higher values of both being preferred. Figure 5.5 plots the optimal stiffness and sensing values against the volume fraction constraint. Note that because the side constraints on each element restrict the local volume fraction to be less than or equal to ten percent, the unconstrained case can have a max global volume fraction of ten percent (each element volume fraction is at its upper bound).

The optimal stiffness is dominated by the volume fraction constraint, with the unconstrained case being forty percent more stiff than the 5% constrained case, which was itself twice as stiff as the 2% constrained case. The topologies that perform the best in stiffness are plotted for each constraint level in Figure 5.6 alongside their volumetric strain fields.

As the model assumes that adding more CNT will always increase the Young's modulus,

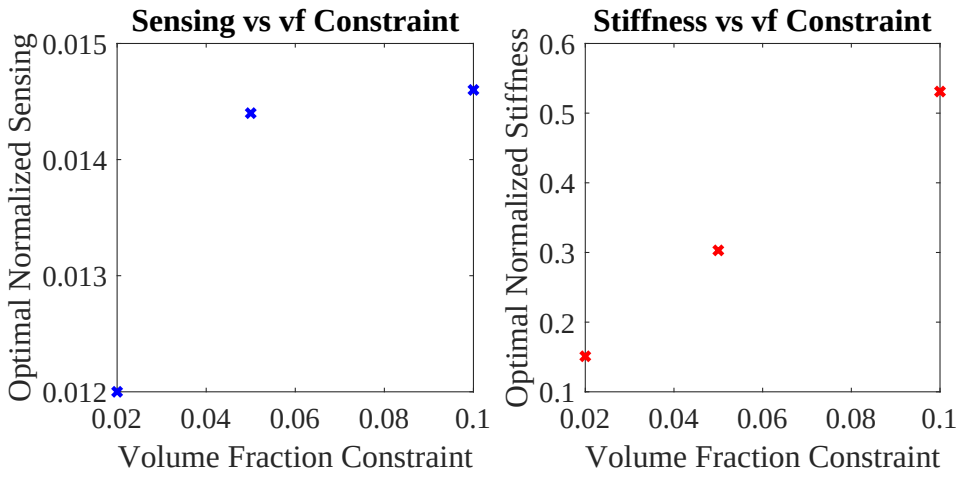

Figure 5.5: Optimal stiffness and sensing vs volume fraction constraint for the plate with a hole case.

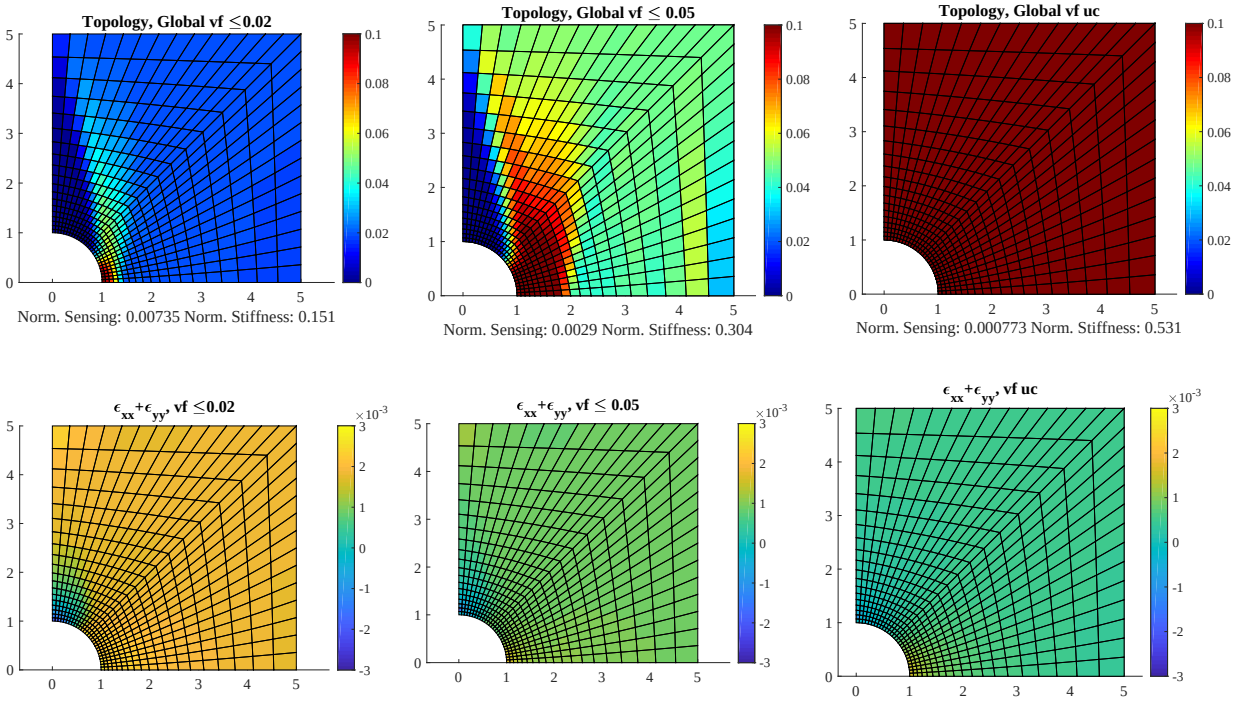

Figure 5.6: Top: Plate w/hole topologies optimized for stiffness. Bottom: Associated volumetric strain fields.

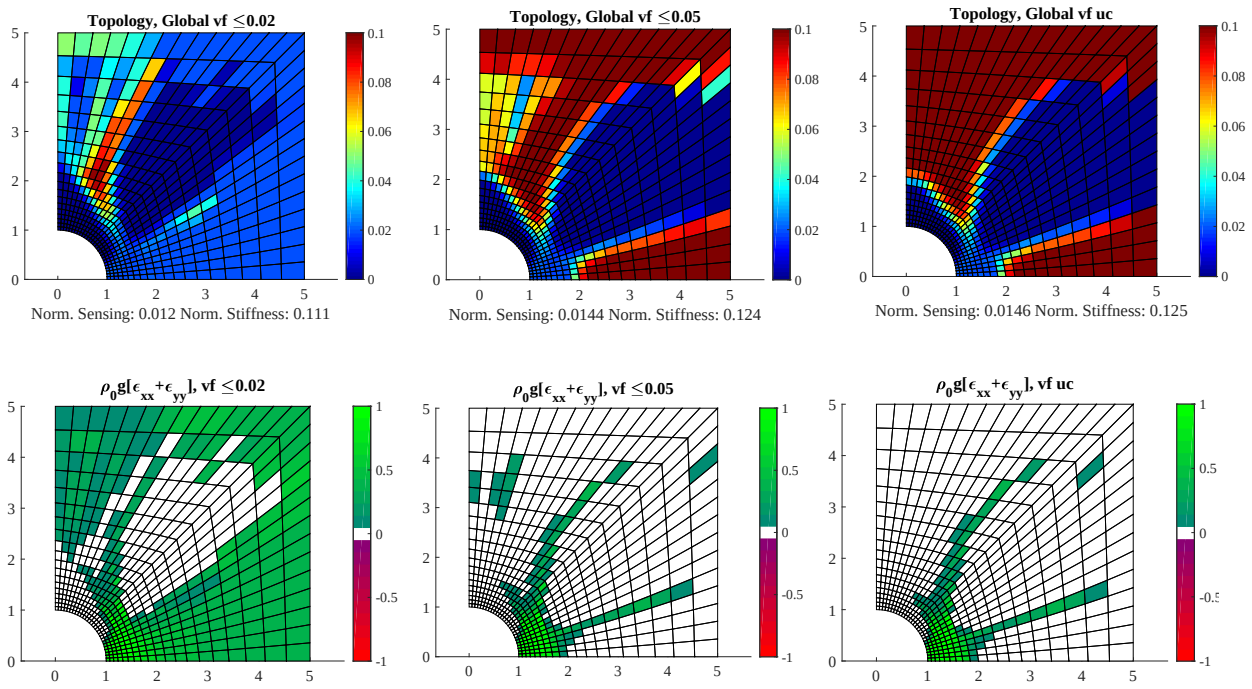

Figure 5.7: Top: Plate w/hole topologies optimized for sensing. Bottom: Associated local resistivity change.

the unconstrained optimum for stiffness maximization is a topology with maximum CNT in each element. Once the volume fraction constraint is activated and begins to restrict CNT usage, the stiffness is maximized by placing higher volume fractions of CNT near the right edge of the hole. This is done to minimize the stress concentration at this location. Another common feature in both the 2% and 5% topologies is an arc leading up and around the net-negative strain region. Away from the hole the strains are relatively uniform, and the optimizer has little preference as to volume fraction or specific topology in this region.

While relaxing the CNT volume fraction constraint translates to better stiffness in the presented results, more material does not always correlate to better sensing performance. The 5% constrained and unconstrained design both outperform the 2% constrained designs, but there is no sensing gain obtained when relaxing the constraint beyond 5%. In order to investigate this data further, the optimal sensing topologies for each constraint level are plotted in Figure 5.7 alongside their local resistivity changes due to strain.

It is optimal for sensing to place highly piezoresistive (near 2% CNT volume fraction) material near the highly strained right edge of the hole. A conductive path connecting this area to the electrode on the right vertical edge is also common across all of the designs. A region of low CNT volume fraction material in the center of the design, common across all three constraint levels, seems to be a preferred feature of the topology. Examining the local resistivity plots helps explain why this feature is beneficial in sensing. Notice the presence of

high strain-induced resistivity change along the perimeter of this low-CNT region. Adding this central region of low stiffness is increasing the strains along the conductive path, leading to improved global sensing. It also works with the vertical loading to create a load path that further concentrates strains in the high sensing region. Of course, carving out a large piece of the design and dumping more load into a relatively compliant (at 2% CNT) section of the structure may not be optimal in stiffness, but it makes for the best sensor.

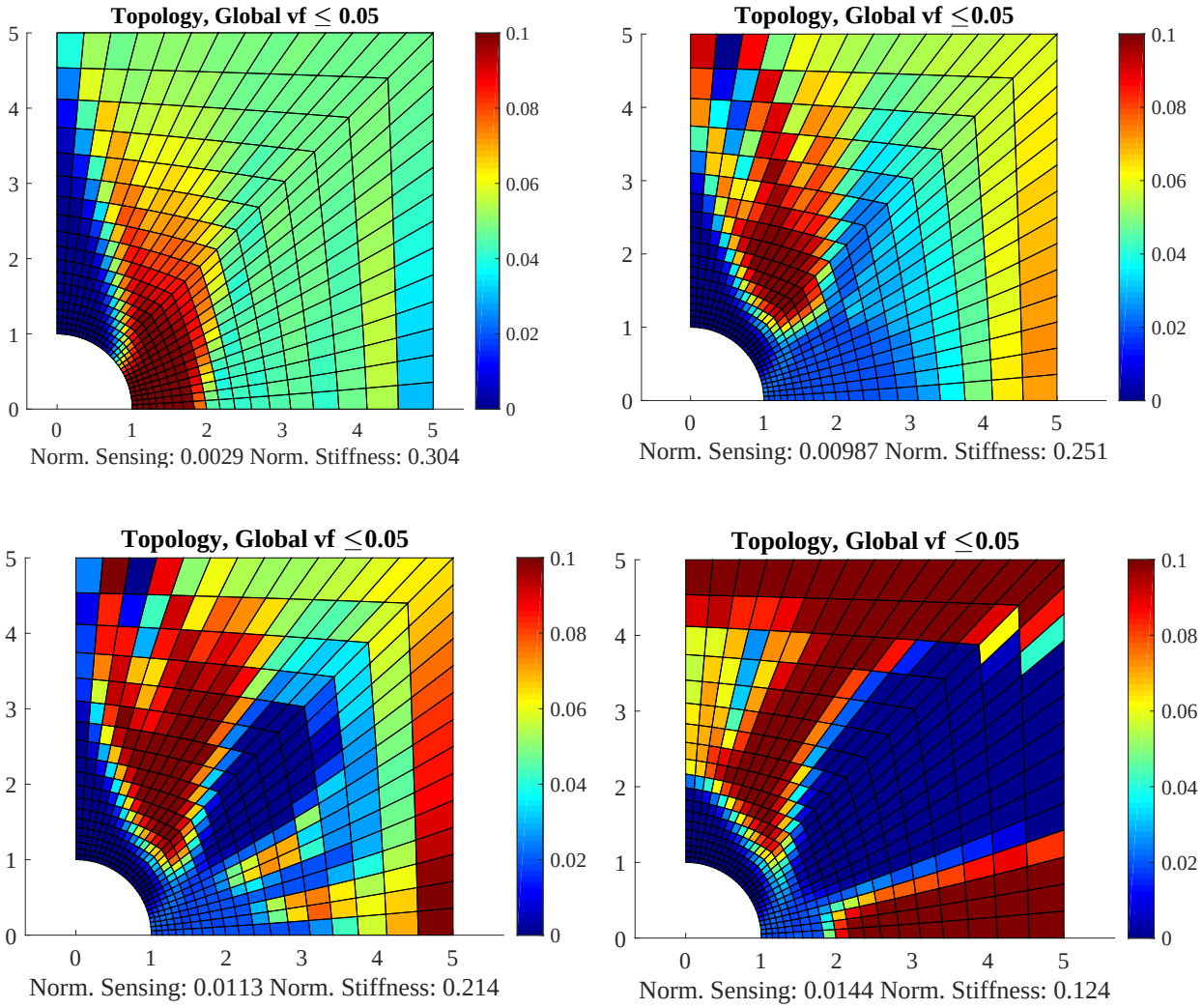

Figure 5.8: Select Pareto optimal topologies for the 5% constrained plate w/hole sample. Top left to bottom right transitions from optimal structure to optimal sensor.

To better characterize the transition from best structure to best sensor Figure 5.8 shows four of the Pareto Optimal topologies from the 5 % constraint results along with their respective stiffness and sensing performance. As the stiffness epsilon-constraint is relaxed, the region of low CNT in the center of the design grows, trading stiffness for improved

sensing. The optimizer is manipulating the strain field to boost resistivity changes in the highly piezoresistive regions. This phenomena was not captured in the uncoupled design, and is only introduced once the full set of physics are controlled by the CNT volume fraction. This is seen in the plotting of the optimal sensing topology with a 5% constraint for the coupled and uncoupled physics in Figure 5.9. In this example, including the coupled physics and allowing the CNT distribution to manipulate the strain field leads to a doubling in the sensing performance.

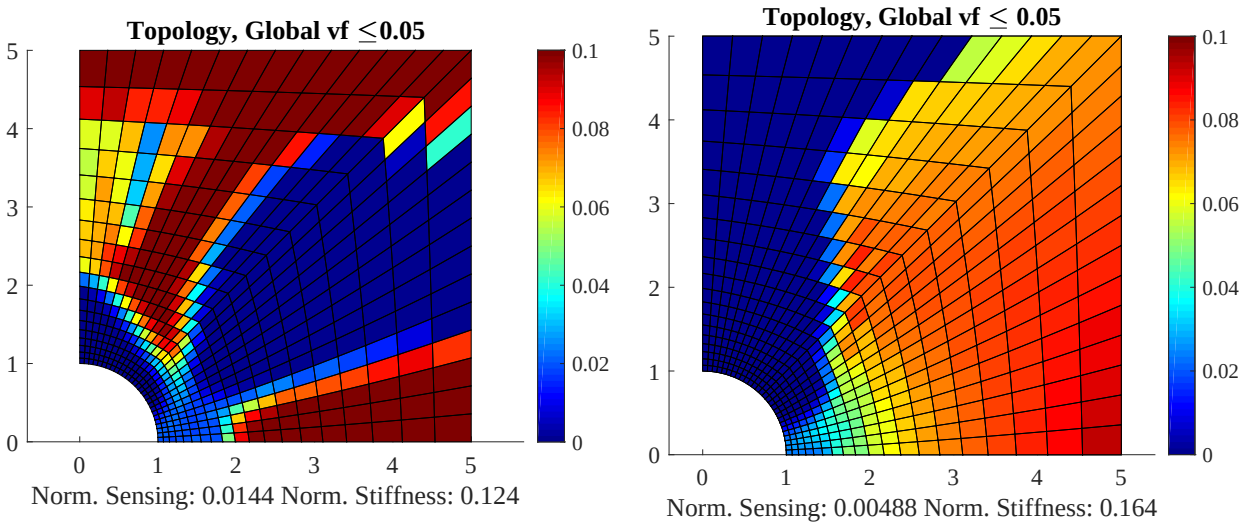

Figure 5.9: Left: Sensing optimization with coupled physics. Right: Sensing optimization constant Young's modulus (fixed strain field from bottom left of Figure 5.3), post processed with coupled physics.

5.3.2 Optimization of the Compact Tension Sample

The optimization problem established in the beginning of Section 5.3.1 is repeated here for the compact tension sample that was introduced in Figure 5.2. The electrodes are placed along the top and bottom edges. The topology, volumetric strain field, electric potential field, and the local resistivity change field for this structure with a uniform 5 % volume fraction distribution are shown in Figure 5.10. The blue and red bars in the electric potential field plot mark the electrode configuration used for all compact tension results presented in this section.

Notice that both the volumetric strain and the resistivity change are dominated by the strain in the notched region. Also note the shift from net positive to net negative volumetric strain around the edge of the structure, and the corresponding negative resistivity change. As was seen in the beam cross-section optimization, having both positive and negative resistivity change in the conductive path is suboptimal. It is up to the optimization algorithm to find a

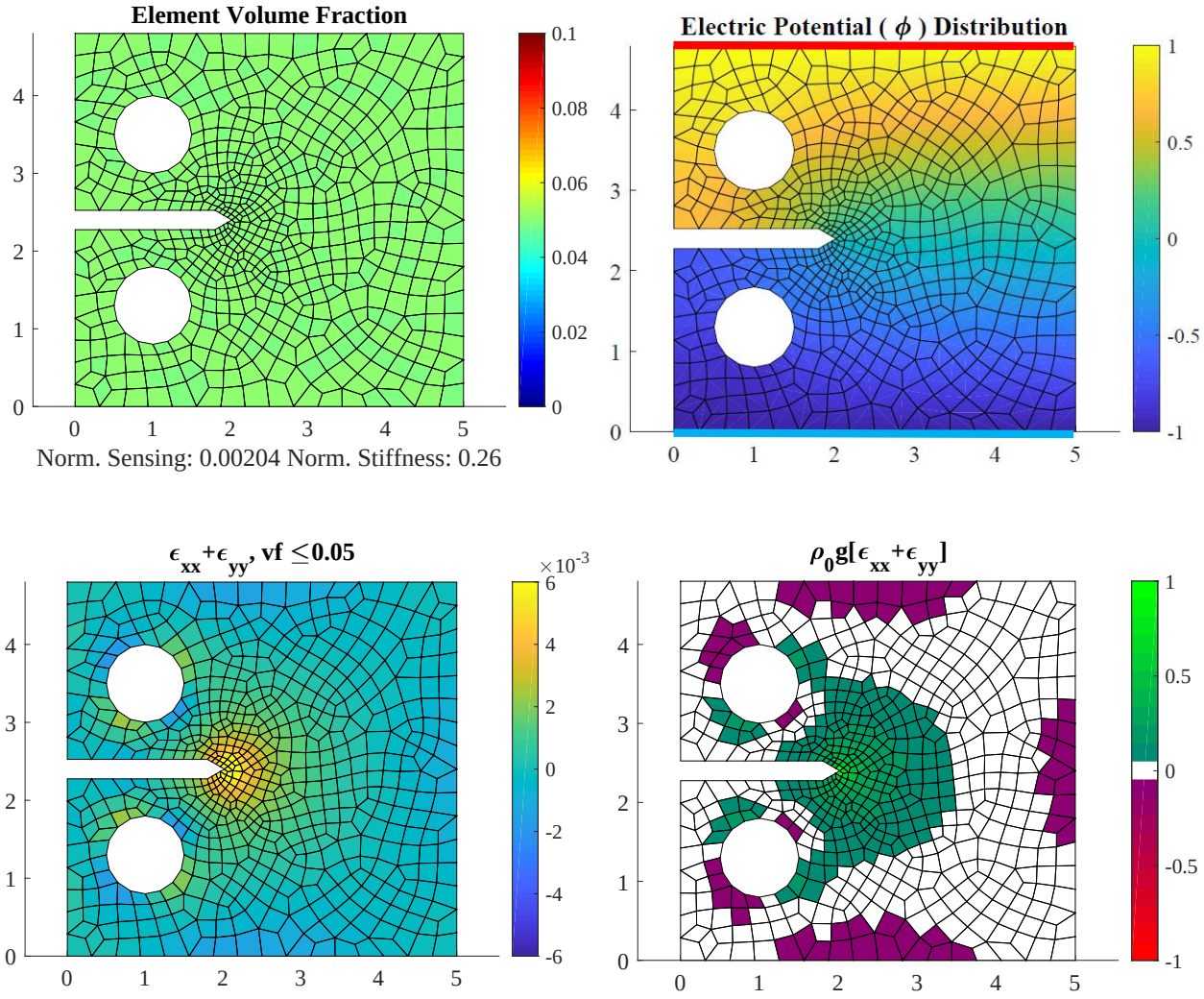

Figure 5.10: Top Left: Uniform Topology w/ Sensing and Strain Energy Performance. Top Right: Electric Potential Distribution. Red and blue bars mark electrodes. Bottom Left: Volumetric Strain, assuming $\epsilon_3 = 0$. Bottom Right: Resistivity Change due to Strain

way to connect the electrodes without introducing too many competing resisitivty changes. This problem is solved in the same manner as the plate w/hole, and the Pareto Fronts for 2%, 5%, and the unconstrained case are shown together in Figure 5.11. Again, the green x is used to indicate the performance of a topology with a uniform volume fraction distribution.

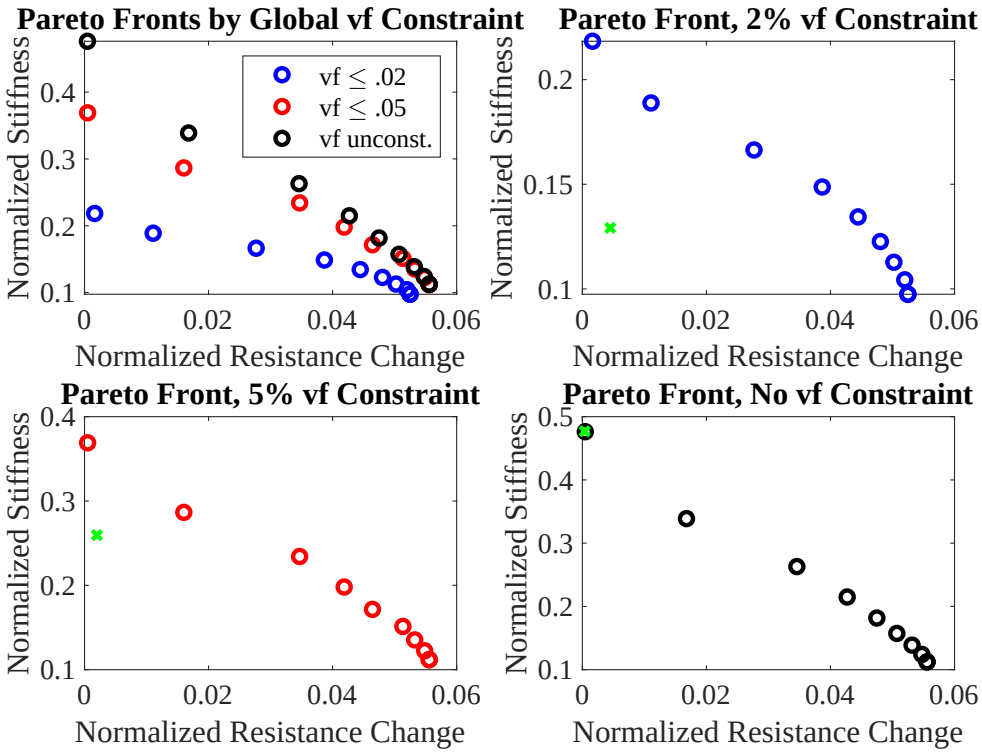

Figure 5.11: Pareto Fronts across global volume fraction constraints for the compact tension sample. Green x marks uniform topology performance.

The best performing stiffness and sensing values are plotted against volume fraction in Figure 5.12. Relaxing the volume fraction constraint again increases stiffness performance and increases sensing performance, up to a point. Stiffness is maximized by placing high volume fraction material around the notch, an area of high strain as seen in Figure 5.11. Optimal stiffness topologies and their associated volumetric strain fields are plotted in Figure 5.13.

The optimization is able to significantly improve upon the stiffness compared to the 5% uniform design. The optimized 2% design is only thirteen percent more compliant than uniform 5% design, while using less than half the material. The optimized 5% design is thirty-two percent stiffer than its uniform counterpart, while using the same amount of material. The unconstrained design, though less interesting as it is simply maximizing the local CNT volume fractions, provides the best possible stiffness value and is forty-six percent more stiff than the uniform 5% design. Stiffness is maximized by first placing high-CNT

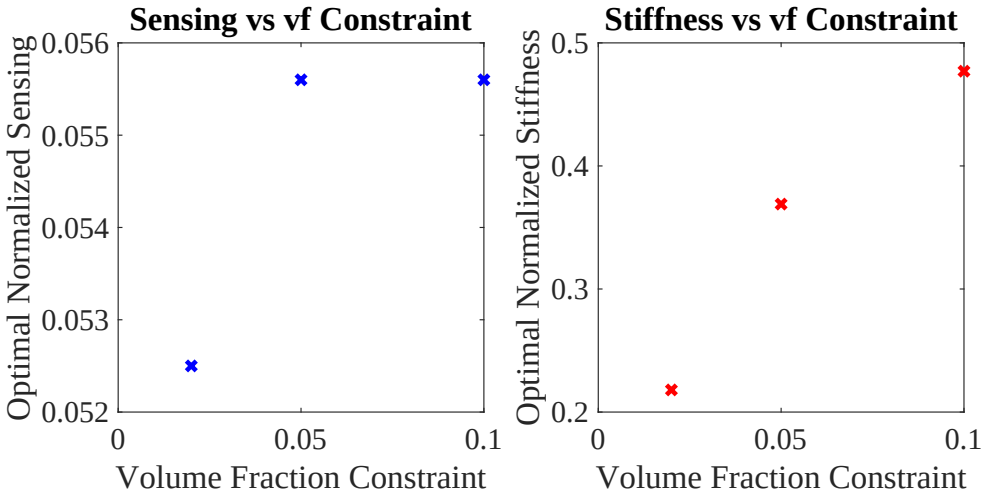

Figure 5.12: Optimal stiffness and sensing vs volume fraction constraint for the compact tension case.

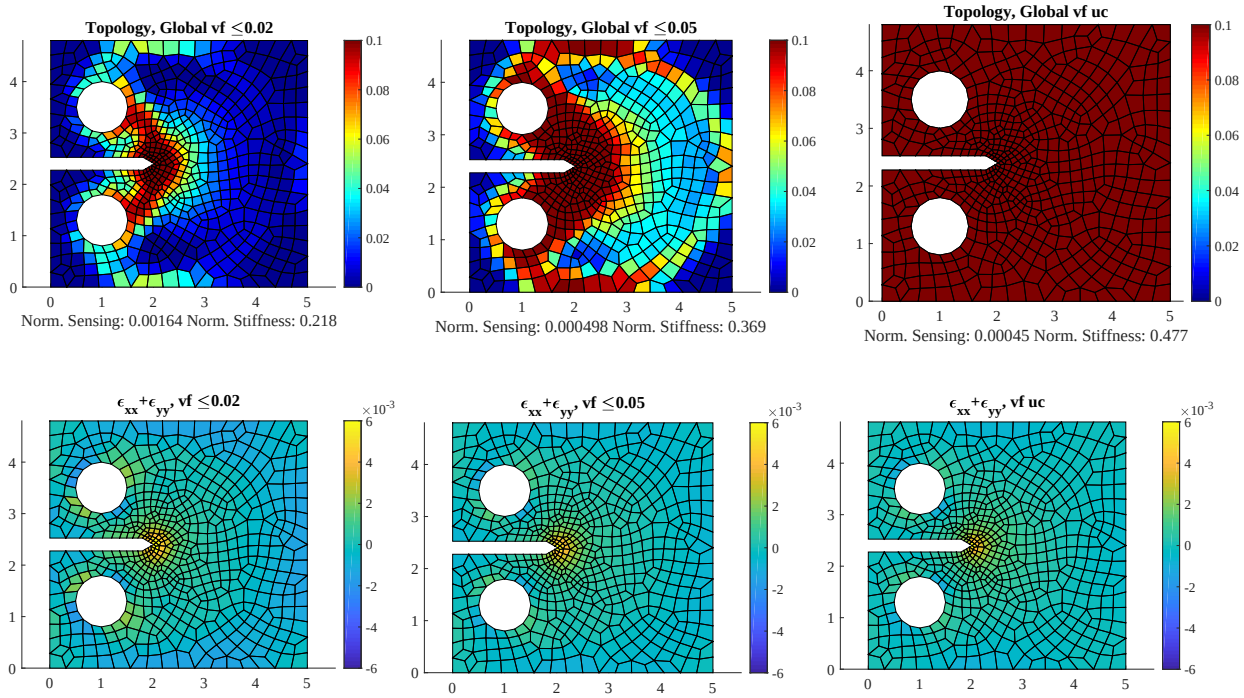

Figure 5.13: Top: Compact tension topologies optimized for stiffness. Bottom: Associated volumetric strain fields.

elements near the notch, and then connecting to the load holes. If additional CNTs are available, extending structural reinforcement to the top and bottom of the structure further improves stiffness, as seen when transitioning from the 2% to 5% constrained designs.

There are slightly diminishing returns on the stiffness performance as the volume constraint is relaxed. As the strain is dominated by the notched region, adding more stiff material away from this region is not overly efficient in further reducing the strain energy. Also, note that even with the maximum allowable amount of CNT in the notched region there is still a significant strain concentration. It appears that optimal structures operating under a volume fraction constraint can recover a sizable percentage of the max attainable stiffness via placement of stiff (high volume percent CNT) in the highly strained regions. However, as has been shown, stiff material in this region can be detrimental to sensing performance.

In regards to sensing performance, the 5% and unconstrained designs obtain identical sensing, and the 2% constrained design is able to achieve over ninety percent of the max attainable sensing for the compact tension sample. Compared to the plate with a hole structure, the compact tension sensing performance is affected less by the volume fraction constraint. This is due to the fact that the notch creates a highly localized region of very high strains, even more so than the hole in the plate with a hole structure. Most of the sensing performance is recovered as long as there is available CNT to place highly piezoresistive volume fractions (2 percent CNT) around this location. Optimal sensing topologies and their local resistivity changes for each constraint level in are plotted in Figure 5.14.

The optimal sensing topology forms a conductive path between the electrodes while concentrating the best sensing elements the notch edge. Further improvements are obtained by manipulating the strain field such that there is compliant material to the right of the notch, boosting the sensing via increased strains in a similar manner to the central cutout topology shown for the plate with a hole structure.

Stiffness is dominated by placing high CNT concentrations at the notch, and then linking the pin holes with more stiff material. Conversely the sensing objective is maximized by placing piezoresistive 2% CNT at the notch, inducing high strains near this region to increase the local resistivity changes, and placing highly conductive material between the top and bottom electrodes. As the epsilon-constraint on the stiffness is relaxed the Pareto optimal topologies corresponding to the points in Figure 5.11 change to reflect this shift in optimal behavior. This is shown for the 5% CNT constrained designs in Figure 5.15, with four Pareto Optimal topologies plotted alongside their respective performance values.

By removing stiff material from around the notch the design is able to leverage the influence of the CNT distribution on the strain field. This is seen in Figure 5.16. Similar to Figure 5.9, by including the strain-modifying behavior of the CNT distribution the optimization is able to sacrifice some of the stiffness performance to obtain a better sensing performance.

Section 4.2.2 showed that intelligent selection of the electrostatic boundary condition could help to improve sensing performance and decouple the competing behavior of stiffness and

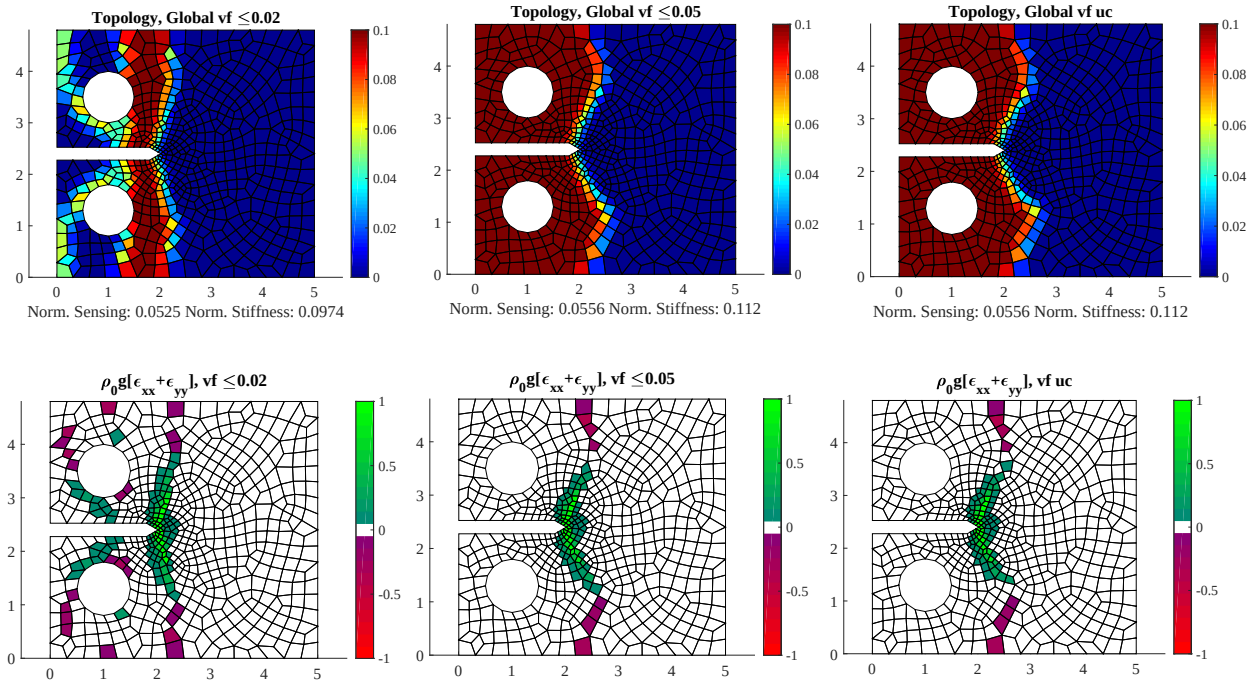

Figure 5.14: Top: Compact tension topologies optimized for sensing. Bottom: Associated local resistivity change fields.

sensing. There may exist some electrode location for which the structure can be stiff and still retain good sensing properties, or for which a comparative stiffness can be obtained with a higher sensing. This is to be examined in the following chapter.

5.4 Conclusions for Optimization of the 2D Structure

In this chapter a set of 2D structures were optimized for maximum stiffness and strain sensing. This first required updating the relevant analyses and sensitivities. A finite element model was introduced for the mechanical performance, the piezoresistive micromechanics were updated to reflect the influence of strains in 2D, and a coupled adjoint sensitivity method was derived for the strained current. This sensitivity was verified against a finite difference method for a test mesh. Two structures were optimized, and for each structure three different volume fraction constraints were considered.

For the plate with a hole structure the stiffness is optimized by placing high concentrations of CNTs around the hole in order to reduce the stress concentration. Optimal Sensing performance requires placing piezoresistive material near the hole, appropriately covering the high strain area. Also, sensing may be increased by manipulating the topology such that the load path is further concentrated in this high sensing region. Including the coupled

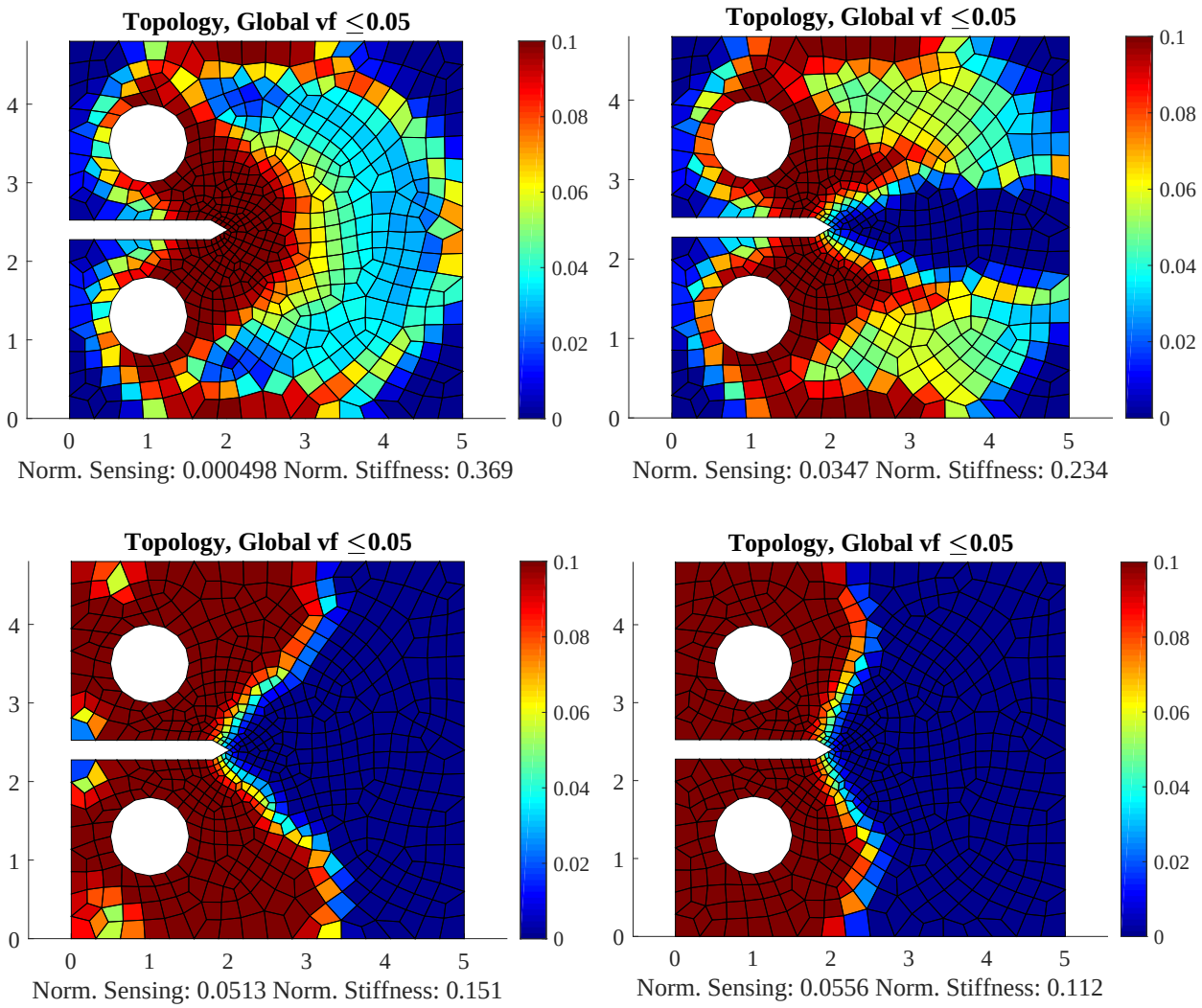

Figure 5.15: Select Pareto optimal topologies for the 5% constrained compact tension sample. Top left to bottom right transitions from optimal structure to optimal sensor.

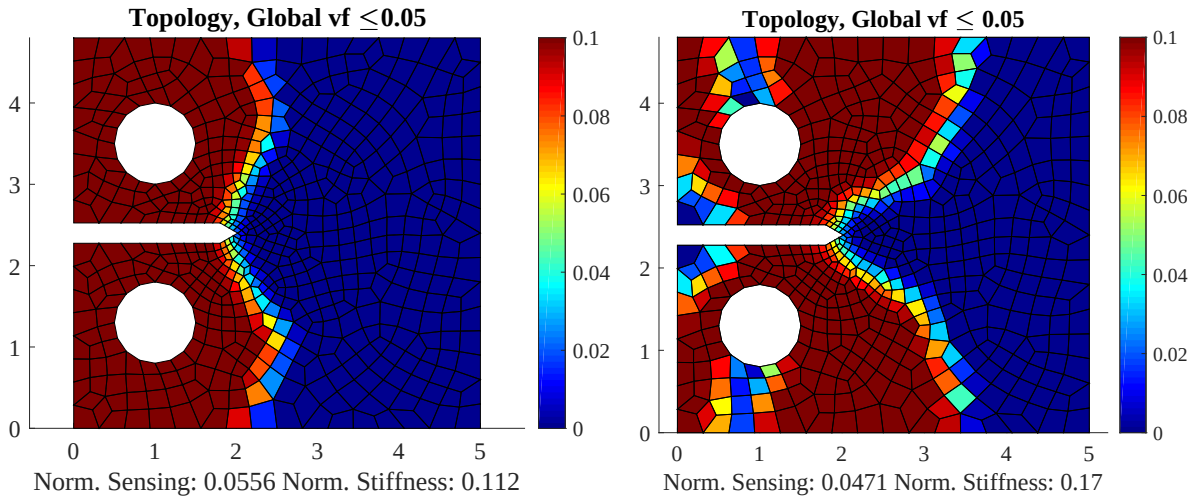

Figure 5.16: Left: Compact tension sensing optimization with coupled physics. Right: Compact tension sensing optimization constant Young's modulus (fixed strain field), post processed with coupled physics.

physics leads to different topologies that more than double the sensing performance when compared to a topology optimized without considering the strain manipulating effects of the CNT distribution.

A compact tension sample was also optimized for stiffness and sensing. It was shown that the global volume fraction constraint played less of a role in the stiffness performance when compared to the plate with a hole. This is due to the fact that the stiffness performance is dominated by the notch region, a highly localized region of large strains. So long as there is sufficient coverage of this region with high volume fraction material, most of the stiffness performance can be recovered. Sensing performance is once again governed by placing piezoresistive material in the high strain areas and linking the electrodes with high volume fraction conductive material. Again, a design that accounts for the coupled physics is able to outperform a design that does not.

It is noted that placement of the electrode boundary condition may have an effect on the sensing results. This is investigated further in the following chapter, using the plate with a hole as an example.

Chapter 6

Optimization of Topology and Electrode Location

The results presented in Section 4.2.2 show that the location of the boundary electrodes can have a significant impact on the strain sensing performance. It would be beneficial to be able to optimize this boundary condition location alongside the CNT topology for a given mechanical loading. Boundary condition optimization presents unique challenges in that these boundaries exist as discrete degrees of freedom in a finite element mesh and cannot be easily integrated into a continuous variable optimization. Turning a node 'on' or 'off' as an electrode requires a way of handling the discrete variables or a way of converting the problem into a pseudo-continuous optimization.

Several potential methods were investigated for solving the mixed discrete-continuous optimization problem. Implementation of mixed-integer methods to simultaneously optimize the continuous-variable topology and the discrete-variable boundary electrode location [100, 101, 102], was considered first. However, these methods often include successive solutions of a topology optimization nested within an outer loop for the boundary condition optimization. This may become prohibitively costly. Also, depending on the method chosen, it may not guarantee convergence to even a local minima. It would be preferable if this could be avoided and the both the topology and the electrode boundary condition could be optimized together using a gradient based method.

As an alternative, surrogate models (covered in depth in [103]) use curve fitting and statistics to interpolate the behavior of a function between discrete evaluation points. Unless remeshing is performed at every optimization iteration, the boundary nodes on a mesh are fixed points, and whether an electrode exists at a given node is a discrete problem. The optimal location of an electrode may well lie between nodes on the mesh. In fact, it would be very rare that the nodes are perfectly aligned to the endpoints of the optimal electrodes. So it is necessary to develop a surrogate model that allows for interpolation of the resistance change performance for electrodes that end between nodes. A quadratic response surface (QRS)

surrogate model is developed for this purpose.

6.1 The QRS Surrogate Model

The design variable vector is updated as $\boldsymbol{x} = [\boldsymbol{v}, \boldsymbol{b}]$, where $\boldsymbol{x}$ are the continuous design variables. $\boldsymbol{x}$ is comprised of the CNT volume fractions, $\boldsymbol{v}$, and the continuous electrode index variables, $\boldsymbol{b}$. For this case, the problem is simplified such that only a single electrode is designed, i.e. $\boldsymbol{b} = [b_1; b_2]$ where b_1 and b_2 mark the starting and ending location of the variable electrode. All nodes on the specified edge that fall between these points will be considered part of the electrode. The following steps introduce the equations needed to compute the surrogate model performance and its sensitivities.

First,the continuous electrode variables are rounded to the nearest discrete value, $\bar{\boldsymbol{b}} = round(\boldsymbol{b})$. The remainder, $\boldsymbol{r} = \boldsymbol{b} - \bar{\boldsymbol{b}}$, will also be used. $\bar{\boldsymbol{b}}$ is used within the analysis and sensitivity to compute the resistance change at the rounded electrode location.

The the resistance change objective at the rounded electrode values is

$$f_n = \frac{\Delta R}{R_0}(\boldsymbol{v}, \bar{\boldsymbol{b}}) \tag{6.1}$$

and the sensitivity of the objective at the rounded values with respect to changes in the volume fractions is

$$\frac{df_n}{dv_e} = \frac{d}{dv_e}\frac{\Delta R}{R_0}(\boldsymbol{v}, \bar{\boldsymbol{b}}) \tag{6.2}$$

To use a quadratic surrogate approximation the function needs to be evaluated at different points of $\boldsymbol{b}$. The $\boldsymbol{\delta}$ matrix is created as

$$\boldsymbol{\delta} = \begin{bmatrix} 1 & -1 & 0 & 0 & 1 & -1 \\ 0 & 0 & 1 & -1 & 1 & -1 \end{bmatrix} \tag{6.3}$$

and the discrete electrode objective function is evaluated for each column of $\boldsymbol{\delta}$.

$$f_{\boldsymbol{\delta}_i} = f(\boldsymbol{v}, \bar{\boldsymbol{b}} + \boldsymbol{\delta}_i) \tag{6.4}$$

These function evaluations are used to form the coefficients for the quadratic equation that may take the form

$$F = f_n + \boldsymbol{B}^T\boldsymbol{r} + \frac{1}{2}\boldsymbol{r}^T\boldsymbol{C}\boldsymbol{r} \tag{6.5}$$

Coefficients for the $\boldsymbol{B}$ vector and $\boldsymbol{C}$ matrix come from finite difference approximations. $\boldsymbol{B}$ is comprised of the first order finite difference coefficients:

$$\boldsymbol{B} = \begin{bmatrix} B_1 \\ B_2 \end{bmatrix} = \begin{bmatrix} \left(f_{\boldsymbol{\delta}_1} - f_{\boldsymbol{\delta}_2}\right)/2 \\ \left(f_{\boldsymbol{\delta}_3} - f_{\boldsymbol{\delta}_4}\right)/2 \end{bmatrix} \tag{6.6}$$

$\boldsymbol{C}$ is comprised of the second order finite difference coefficients:

$$\boldsymbol{C} = \begin{bmatrix} C_{11} & C_{12} \\ C_{12} & C_{22} \end{bmatrix} \tag{6.7}$$

$$C_{11} = \frac{\partial^2 f}{\partial b_1^2} \approx f_{\boldsymbol{\delta}_1} - 2f_n + f_{\boldsymbol{\delta}_2} \tag{6.8}$$

$$C_{22} = \frac{\partial^2 f}{\partial b_2^2} \approx f_{\boldsymbol{\delta}_3} - 2f_n + f_{\boldsymbol{\delta}_4} \tag{6.9}$$

$$C_{12} = \frac{\partial^2 f}{\partial b_1 b_2} \approx \frac{f_{\boldsymbol{\delta}_5} - f_{\boldsymbol{\delta}_1} - f_{\boldsymbol{\delta}_3} + 2f_n - f_{\boldsymbol{\delta}_2} - f_{\boldsymbol{\delta}_4} + f_{\boldsymbol{\delta}_6}}{2} \tag{6.10}$$

The sensitivity of the surrogate model to changes in the electrode variables is then

$$\frac{\partial F}{\partial b_i} = B_i + C_{ij} r_j \tag{6.11}$$

And the sensitivity with respect to all design variables: $\dfrac{dF}{d\boldsymbol{x}} = \left[\dfrac{df_n}{d\boldsymbol{v}} \dfrac{dF}{d\boldsymbol{b}}\right]$. $\dfrac{df_n}{d\boldsymbol{v}}$ is obtained from Equation 6.2.

6.2 Validation of the Surrogate Model

It is necessary to validate the surrogate model to show that it is adequately able to capture changes in sensing performance for electrodes that exist between nodes. The plate with hole structure is used for both this validation, and throughout the following results sections. Two meshes are used to help validate the surrogate model. In both models the negative electrode is fixed along the length of the right vertical edge. The positive electrode is fixed to the inner circular edge, but its length and location along this edge is allowed to vary. Figure 6.3 shows the structure, electrodes, and loading. The coarse mesh contains 16 elements along this inner curved edge. The second mesh has 32 elements along the curved edge.

The coarse mesh will be used in conjunction with the surrogate model, in which the parameter s will scale how far from an actual FEA node the electrode is being placed. By stepping through $0 \leq s \leq 1$ the validation analysis will iteratively move an end of the electrode from one node on the coarse mesh, into the space between nodes, and eventually to the next node. i.e. $\boldsymbol{b}_{coarse} = [b_1, b_2 - s]$ where $\boldsymbol{b}$ are the continuous electrode variables defined in the previous section. In the space between the nodes the performance will need to be approximated by the surrogate model.

Comparatively, the fine mesh has twice as many nodes along the curved edge, and rather than trading $0 \leq s \leq 1$ across the fine mesh is evaluated only at nodal locations. The fine mesh will not use interpolation, and will be used to validate the nodal and mid-point (interpolating) performance of the coarse mesh with the surrogate.

Three evaluations of the fine mesh (corresponding to the left end nodal location of the coarse element, the center of the coarse element, and the right end nodal location of the coarse element) are performed for comparison. The volume fraction of all elements is set to an even 5% CNT, and loading and mechanical constraints are the same as in Section 5.3.1. The result of moving across one coarse mesh element are shown in Figure 6.1.

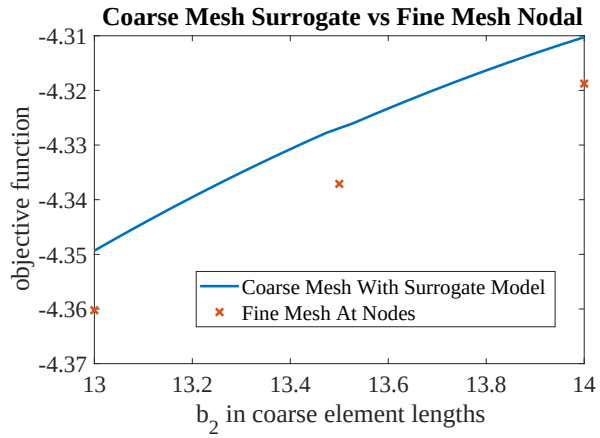

Figure 6.1: Comparing Coarse Mesh w/ Surrogate Model to Fine Mesh at Nodes

The performance changes in a similar manner for both the surrogate model and the fine mesh model as the electrode moves across the coarse element. Due to the differences in the finite element meshes themselves, the value of performance for the surrogate with the coarse mesh will not align with the performance of the fine mesh. What is important is that the shape of the curves be similar, which is the case. This is sufficient evidence that the surrogate model is performing it's job, and may be used in the optimization routine. For an in depth look at surrogate performance across multiple volume fractions and electrode configurations, refer to Appendix A.

A slight discontinuous change in slope is observed at the $b_2 = 13.5$ location for the surrogate

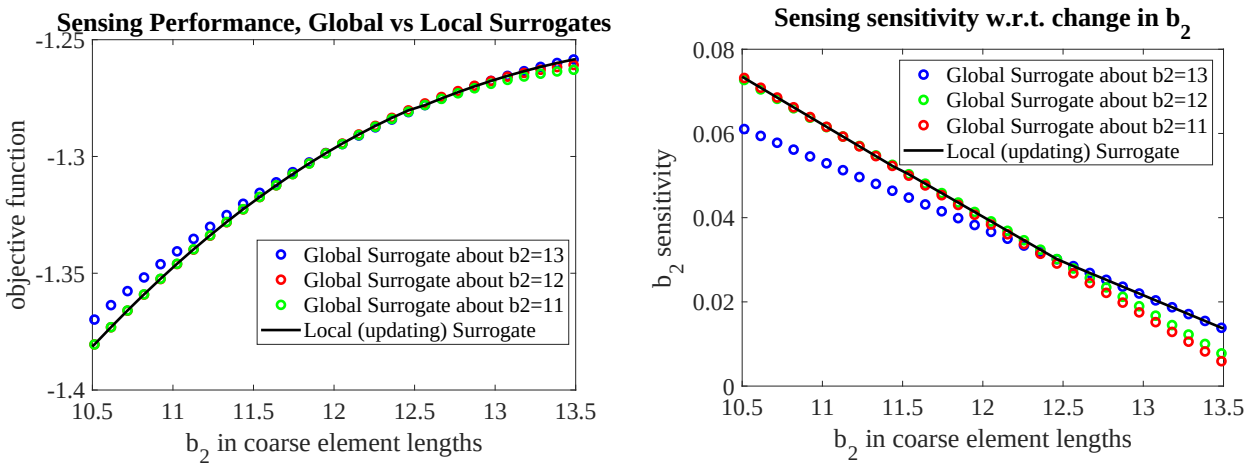

Figure 6.2: Left: Sensing performance across different local surrogate models. Right: sensing sensitivity to the design variable for the different models. The black line traces the model used in this dissertation.

model. This is due to the fact that the model presented in the previous section first rounds the continuous $\boldsymbol{b}$ variables and then constructs the surrogate by applying the $\boldsymbol{\delta}$ matrix to the rounded variables. At $b_2 = 13.5$ the rounded variable $\bar{b_2}$ transitions from 13 to 14, and the surrogate model is constructed about a different point. An alternative to this formulation is to apply a single global surrogate model over a larger range. This is not advised as the resistance change performance can be highly sensitive to electrode location, and the model may be inaccurate if evaluated far from the point about which it is constructed. Figure 6.2 helps to show this by plotting three global surrogate models. The models are constructed about different b_2 locations as per the figure legend. The surrogate model used herein is locally updated, changing between different global surrogate models. It is traced out by the black line in the figure.

Notice that the further the b_2 variable strays from the point about which the global surrogate is created, the further that specific surrogate deviates from the others. At $b_2 = 10.5$, for example, the surrogate about $b_2 = 13$ is starting to become inaccurate when compared to the other global surrogate models. A similar trend is noticed in the sensitivity, plotted on the right of Figure 6.2. The global surrogate models appear to only be accurate over a small range of b_2 values, reinforcing the idea that a locally updating surrogate scheme is beneficial.

It must be noted that due to the rounding nature of the locally updating scheme discontinuities may exist at the halfway points between integer b_2. These were sen to be small, and did not lead to troubles in obtaining the results presented in this dissertation. But such a formulation could, in theory, cause slow or unreliable convergence. In the future, if the scheme is to be improved upon, it may be useful to develop some interpolation scheme that connects the local surrogates via some continuous and differentiable curve.

6.3 Selecting the Optimization Method

As the surrogate model requires seven additional function evaluations per iteration, it is important to select an appropriate optimization method. The method should converge to strong optima while not being overly costly from a computational perspective. A trade study is performed to compare Sequential Linear Programming, Sequential Quadratic Programming, and Interior-Point optimization methods.

Sequential Linear Programming [104, 105] seeks to simplify an optimization problem by creating a Taylor Series approximation of the problem about the current design point. This problem can then be solved by convential optimization routines (Simplex, first order interior-point, etc.). One benefit of the method is that it does not attempt to compute or approximate second order terms i.e. the Hessian. This can improve speed in within each iteration, as it is often inefficient to compute Hessians of large or complex problems, and Hessian approximations of large problems may not be accurate for a large number of iterations. However, as the method is first order, it can have slower convergence than a method that retains some information about the curvature of the design space at the current point. This lack of information can lead to slow convergence if care is not taken to properly control step size via move limits, trust regions, or other bounding methods. Several open source versions of SLP are available, and for this study an SLP algorithm with a trust region strategy [106] was selected.

Interior-Point [107, 108] methods are a class of barrier methods which append the objective function with a so-called barrier function that is representative of the constraint feasibility. This barrier function penalizes designs that approach the constraint boundaries, keeping the design on the interior of the feasibility space. Care must be taken to construct a proper barrier function, and often it is the case that this function changes as the optimization proceeds. For example, consider the common logarithmic barrier function below.

$$B = f(\boldsymbol{x}) - \mu \sum_{i=1}^{n} log(g_i(\boldsymbol{x})) \tag{6.12}$$

Where f is the objective and $\boldsymbol{g}$ the set of constraints. Often the penalty parameter μ will be decreased as the optimization progresses, allowing the design to more closely approach the constraint boundaries. Clearly, as μ approaches 0 the barrier function approaches the original objective function. Interior-Point can be used to solve first and second order problems.

Like SLP, Sequential Quadratic Programming (SQP) creates a Taylor Series approximation of the problem at each iteration. However, SQP uses a second order series to capture local curvature. This can greatly improve performance, especially for highly nonlinear problems. However, this is traded with the need to either compute or approximate the second order derivatives of the objectives and constraints. Often obtaining second order derivatives is difficult or impossible. Also, in the case of topology optimization, where there can be hundreds

Table 6.1: Results for optimization algorithm trade study for optimization with the surrogate model. Greyed values are the best performers. Bold stepsize means the run did not converge to the set tolerance of 1e-5.

SLP				SQP				Interior-Point			
Iterations	Runtime (sec)	Stepsize	Optima	Iterations	Runtime (sec)	Stepsize	Optima	Iterations	Runtime (sec)	Stepsize	Optima
1000	1260	**1.56E-05**	8.75	175	395	1.12E-06	12.21	685	511	1.49E-06	8.61
1000	1262	**2.59E-05**	12	451	1079	2.82E-06	17.25	442	468	2.84E-06	9.15
1000	1348	**1.95E-05**	3.66	362	533	1.16E-06	4.60	393	295	4.04E-06	2.99
1000	1259	**3.65E-05**	6.98	43	170	3.01E-06	6.72	226	206	8.32E-07	5.92
741	5927	1.95E-06	10.05	240	8169	4.33E-06	12.86	250	1946	3.77E-06	7.38
1000	8173	9.95E-06	10.67	704	13851	1.76E-06	12.61	77	410	4.61E-06	6.32
1000	7985	**1.56E-04**	3.23	72	2793	1.32E-06	3.95	438	2186	2.65E-06	2.67
1000	7950	**6.32E-05**	6.51	199	2789	1.89E-06	7.07	285	1898	2.59E-06	5.53

or thousands of design variables, Hessians constructed from second order information can become enormous matrices to compute and store. It is often the case then that the Hessian is not computed, but approximated using first order information from both the current and previous optimization iterations. Methods such as BFGS [109] and the large-problem limited memory variant L-BFGS [110] are used to efficiently approximate the Hessian and are updated at each design iteration.

Matlab's constrained optimization suite [92] comes with built in Interior-Point and SQP functions. As the number of topology design variables can be large, the L-BFGS method is employed to approximate the Hessian for both the SQP and Interior-Point optimizations.

The 2D plate with a hole is used for the optimization algorithm trade study. The structure is constrained to have electrodes on the inner circular edge and on the right vertical edge, but the width and location of inner electrode were defined by the electrode design variables. The problem was optimized without a volume fraction constraint and with a 2 percent volume fraction constraint for 2 different (1 uniform and 1 random) initial conditions. Additionally, two meshes were considered. The coarse mesh consists of 486 elements while the fine mesh consists of 1364 elements. This results in a total 8 test cases.

The QRS approximation requires 7 analysis calls to create the surrogate model. As each analysis call requires 1 solution of the mechanical finite elements and 2 solutions of the electrostatic finite elements, it is important to track both final performance and computational cost. Final convergence, number of iterations to converge (capped at 1000), runtime, and final performance are shown across all three methods for the 8 test cases in Table 6.1.

Based on these results, SQP appears to be the clear winner in all categories except runtime. SLP fails to converge in 1000 iterations in all but 2 runs, and while Interior-Point always converges, it does so to weaker optima. SLP, being a first order method, will typically have slower convergence for complex problems when compared to the other second order methods. It may be possible to reduce the runtime of SLP by using a first order surrogate model. As SLP does not approximate a Hessian, it does not require a quadratic model. Of course, while this improves runtime, a first order model may be less accurate than its quadratic

counterpart. For fairness in comparing methods in this trade it was decided to use the same surrogate model for all optimization methods.

Interior-Point, while generally faster to converge, is a barrier method that pushes the designs away from constraint surfaces. This may help to explain why it is unable to find as good of an optima as SQP, and also explain why it may converge faster. SQP may take several subiterations within each major iteration to find a feasible descent direction, as it is closer to the boundary of the feasible space. Matlab's documentation of algorithm selection in *fmincon* even recognizes this fact, showing in an example problem where Interior-Point is used for speed, and then SQP is used to restart the problem and find a better optima [92]. The speed increase of Interior-Point is only significant in the fine mesh runs (rows 5-8 of Table 6.1). If one were to write their own Interior-Point algorithm it may be possible to improve performance by implementing an update scheme for the barrier parameters $\boldsymbol{\lambda}$. The update strategy in itself is heuristic, and significant tuning may be required to get satisfactory results.

As it is generally preferred to find stronger optima so long as the cost is not completely prohibitive, SQP is chosen as the method to use in the surrogate optimization.

6.4 Optimization Results for Topology and Boundary Electrode Placement

The 2D plate w/hole structure from Section 5.3 is reintroduced here and the same mechanical loads and mechanical boundary conditions are applied. The negative electrode remains fixed, but the location and length of the positive electrode may vary along the edge shown in Figure 6.3. The electrode is designed via two continuous variables, the $\mathbf{b}$ vector from Section 6.1. b_1 controls the starting point of the electrode, and b_2 the end point. These variables are constrained such that $b_1 > b_2 + 1$ to prevent the rounded variables in the surrogate model from being the same, resulting in a 0 length electrode. As the surrogate model also makes use of the adjacent element edges, the electrode is constrained such that the rounded electrode variable may not occupy the initial or final element edge, which would result in the surrogate model having no adjacent edge to evaluate. It may be possible to remove this constraint by introducing separate forward or backwards surrogates that are implemented only at the ends of the potential electrode space.

The optimization is again performed using ten epsilon-constraint values and three global CNT volume fraction constraints (2%, 5%, unconstrained). Results are compared against the results for the respective fixed electrode cases.

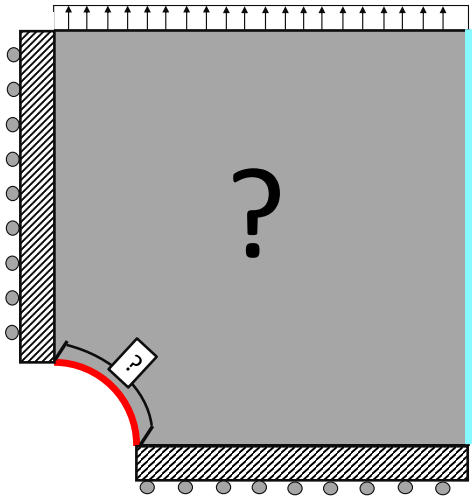

Figure 6.3: 2D plane stress design space with designed electrode included.

Table 6.2: Comparing sensing performance for fixed and designed electrode.

2%			5%			Unconstrained		
Fixed Electrode	**Optimized Electrode**	**Ratio**	**Fixed Electrode**	**Optimized Electrode**	**Ratio**	**Fixed Electrode**	**Optimized Electrode**	**Ratio**
0.0104	0.0151	1.46	0.0113	0.0204	1.81	0.0093	0.0177	1.89
0.0120	0.0193	1.62	0.0144	0.0274	1.90	0.0146	0.0274	1.88

6.4.1 Optimization of the Plate w/ Hole Structure with Designed Electrode

The Pareto Fronts for designed electrodes and topology are plotted alongside the optima with only the designed topology in Figure 6.4. The 'x' indicates an optima obtained with the designed electrode, the 'o' is reprinted from the fixed electrode results in Section 5.3.1.

At high stiffness there is little difference between a the fixed electrode and the optimized electrode designs. As the strain energy epsilon-constraint is relaxed the design that includes the variable electrode dominates its fixed electrode counterpart. This occurs across all volume fraction constraints, and the increase in sensing performance increases as the stiffness decreases for the 2% and 5% constrained cases. Table 6.2 tabulates the sensing performance with and without the designed electrode. The first column shows the sensing with a fixed electrode, the second shows the sensing with a design electrode, and the third shows the ratio of the two. Optimizing the electrode offers a significant sensing performance across all constraint levels (at least a 1.46 times increase in sensing for the values shown). This increase is more significant (at least a 1.81 times increase for 5% and a 1.88 times increase for the unconstrained case) as the volume fraction constraint is relaxed.

To help explain these results, Figure 6.5 shows two optimal topologies for the 5% constrained

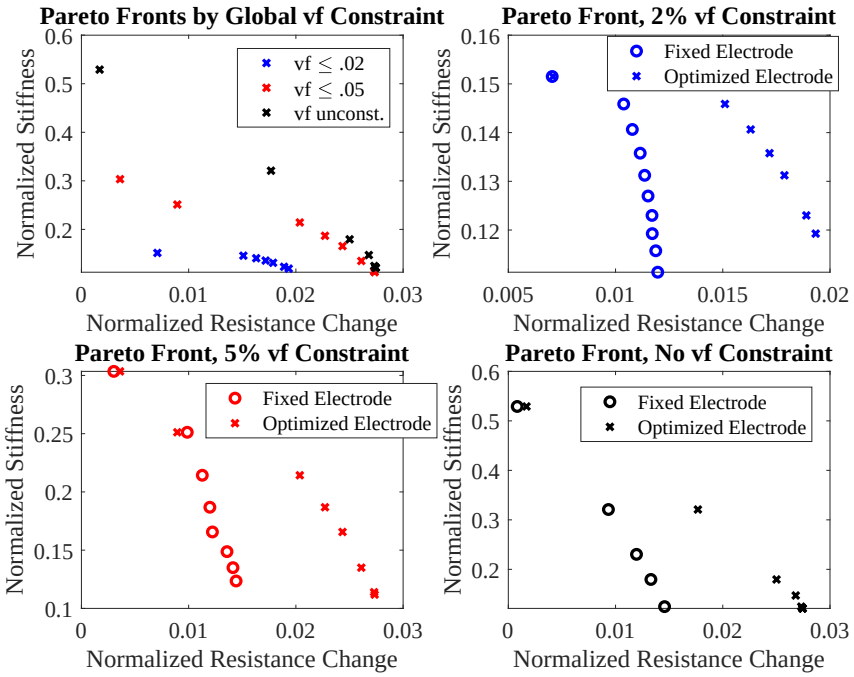

Figure 6.4: 2D plane stress Pareto Fronts comparing optima with designed electrode and topology to optima with just designed topology.

results. The topologies are shown above their respective local resistivity plots. A black bar is used to mark the fixed right side electrode and a purple bar is used to mark the optimized inner electrode. While both of these topologies contain an optimized electrode, the first topology shown is for a design that requires a higher stiffness. The second design has a lower stiffness, and a greatly improved sensing.

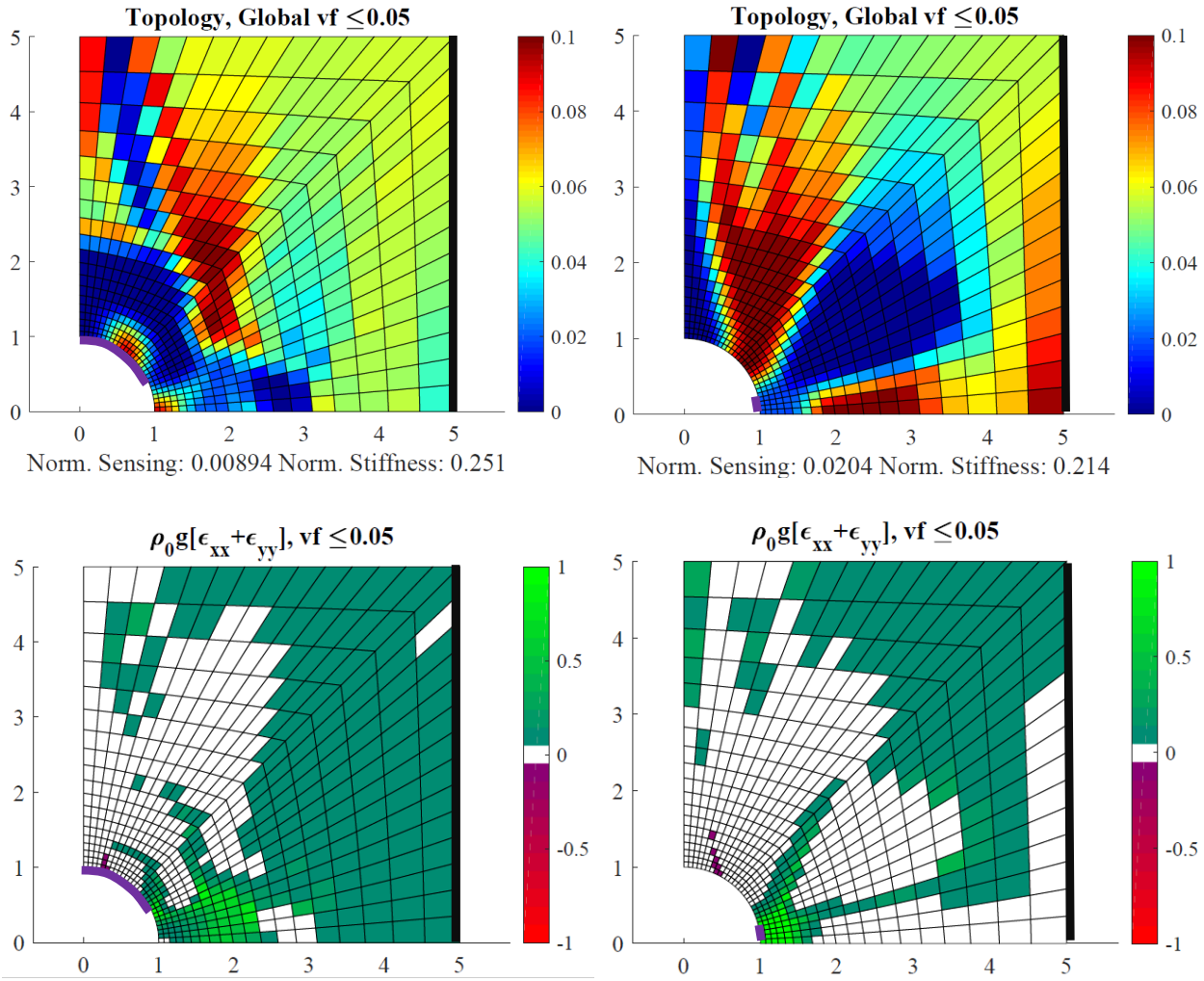

Figure 6.5: Left: Optimized topology with a .251 stiffness requirement. Right: optimized topology with a .214 stiffness requirement. Topologies plotted above local resistivity change.

In the left design the stiff, poor sensing material (red) is used in region around the hole to improve stiffness. The electrode optimization does not appear to be able to take advantage of the stiffer topology, and the optimal still covers a majority of the inner curved edge. This topology and electrode combination does not dominate the fixed electrode results from the previous chapter.

In the right design this stiff material is replaced by the highly piezoresistive (light blue) material. This topology and electrode combination offers nearly double the sensing performance when compared to a fixed-electrode optima. To help explain why this topology dominates its fixed-electrode counterpart, Figure 6.6 plots the second topology next to the optima obtained for a fixed full-length electrode.

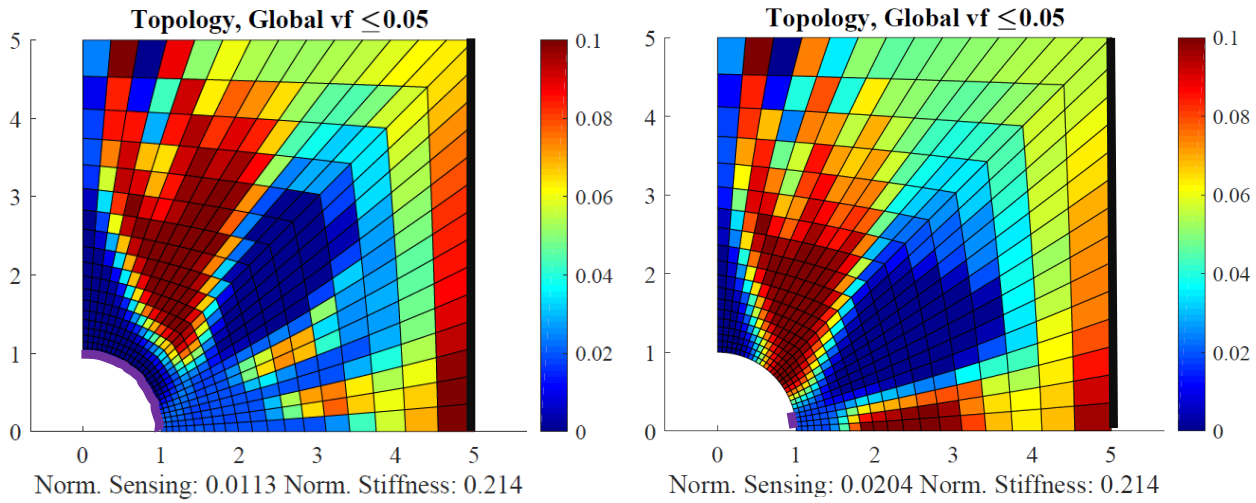

Figure 6.6: Left: Optimized topology with a .214 stiffness requirement and fixed electrode. Right: Optimized topology with a .214 stiffness requirement and optimized electrode.

While the topologies contain similar features, there are important differences. For one, the topology with the designed electrode has stiff material (red elements) distributed around the edge of the hole, next to the piezoresistive material. This is a feature not shared by the topology with the fixed electrode, and allows for a larger cutout in the center-right of the design while still satisfying the strain energy epsilon-constraint. Recall that in these topology plots red elements are both stiff and conductive. If the red elements are attached to the inner electrode, the path of least resistance would bypass the sensing elements in the bottom right of the hole section. With a full length electrode, there is no way to bring this stiff material down to the circular edge without losing sensing performance.

Another advantage the designed electrode optima has is that the optimized electrode only spans the highest strain portion of the circular hole. This forces all of the current to flow directly through the high sensing region. This electrode design is consistent across the best sensing topologies for all volume fraction constraints, which are shown in Figure 6.4.1.

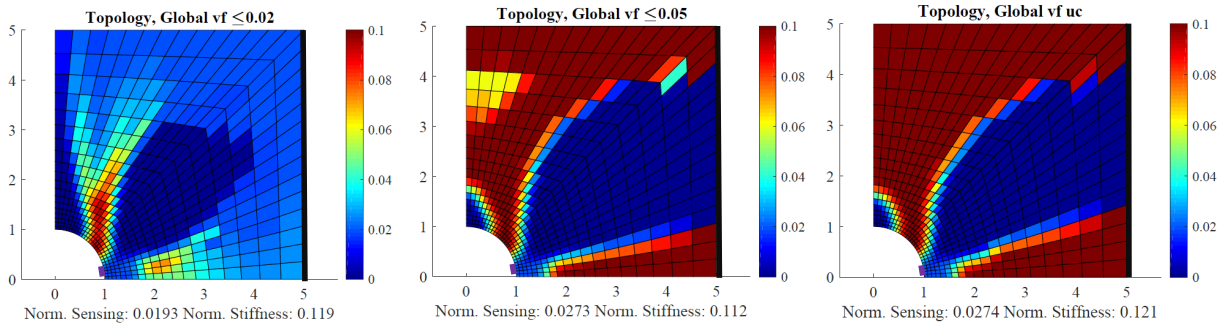

Figure 6.7: Best sensing topologies across all volume fraction constraints, with designed electrode.

In all cases, once the stiffness requirement is sufficiently reduced the designed electrode optima dominate the fixed electrode optima. This stiffness threshold corresponds to when the optimizer no longer needs stiff, poor sensing material to occupy the location of the stress concentration around the hole. For deisgns with intermediate stiffness requirements shifting the electrode allows for unique topologies that satisfy stiffness without subverting the sensing-optimal conductive path. Even when the stiffness constraint is completely relaxed the optimized electrode works with the topology to force the current to flow through the best sensing regions of the design.

The development of the topology with a designed electrode as the stiffness epsilon-constraint is relaxed is shown in Figure 6.8. The development of the optimal sensing features mentioned in the preceding paragraphs are seen to develop as the stiffness requirement decreases.

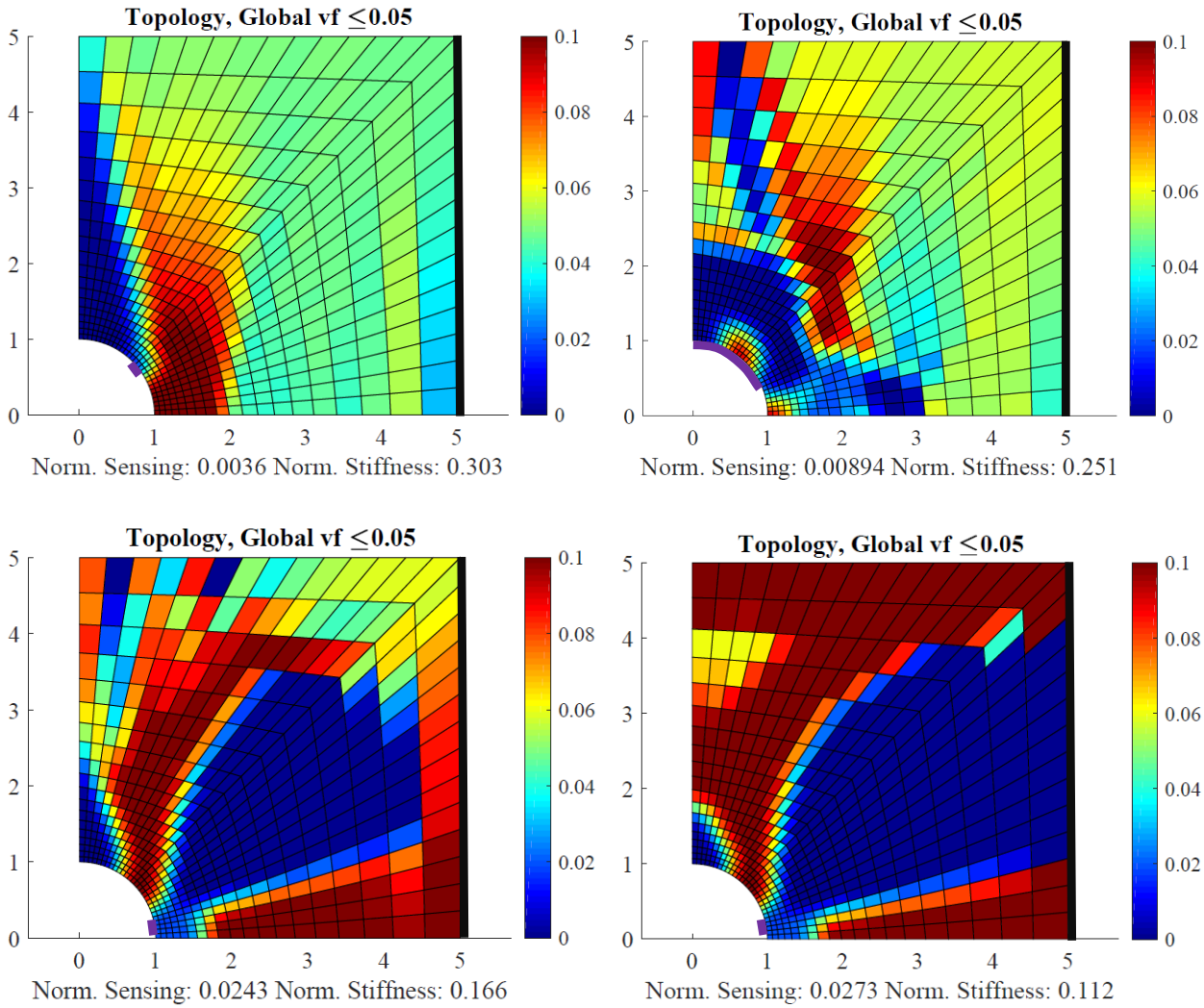

Figure 6.8: Select Pareto optimal topologies for the 5% constrained plate w/hole structure and the designed electrode. Top left to bottom right transitions from optimal structure to optimal sensor.

6.5 Conclusions for 2D Optimization of Topology and Electrode

Based on results in both the cross-section and 2D structure optimization, it was decided that optimizing the electrode along with the topology could further improve sensing performance. This presented a challenge as the electrodes exist as discrete degrees of freedom in the electrostatic finite element problem. A quadratic surrogate model was used to model the electrode start and end locations as continuous variables. This model was validated by

comparing a coarse mesh surrogate evaluated between nodes against a fine mesh evaluated at discrete nodal points.

As adding the surrogate adds computational cost and design complexity, a trade was performed in which a set of test cases were optimized using three different optimization methods. It was shown that, while not as fast as the Interior-Point method, SQP converged to better optima, and converged in fewer iterations than SLP. For these reasons it was selected as the optimization algorithm to be used with the surrogate model.

The plate with a hole test case was reintroduced, this time with a variable inner electrode. It was optimized for stiffness and sensing performance using the epsilon-constraint method. Ten stiffness epsilon-constraint values and three global volume fraction constraint values were selected. Results were compared against the same optimization in Section 5.3.1, which was performed for the fixed-electrode design.

It was shown that tailoring the electrode leads to significant improvements in sensing performance, so long as the stiffness constraint is relaxed enough to not require high volume fractions of CNT in the sensing region. The designed electrode allows the optimizer to place material along portions of the hole edge without forming a sub-optimal conductive path. This allows for the design to satisfy the stiffness constraint, even with an enlarged cutout in the right half of the topology, which aids in sensing. This feature is common across volume fraction constraints, and leads to a near doubling in the sensing performance for designs with low stiffness requirements. The overall optimal design pairs a small electrode along the lower right edge of the hole with a topology that puts the best sensing volume fractions in this location, and then grows a cutout region of low volume fraction material on the right half of the design. The fact that the optimal topologies intelligently react and morph along with the designed electrode is evidence that the method is functional. The fact that adding electrode optimization with the topology nearly doubled the sensing performance for some of the cases shown is evidence that the method is necessary.

Chapter 7

Conclusions and Extensions

7.1 Conclusions

This dissertation presents a multifunctional topology optimization algorithm that seeks to maximize measures of structural, electrical, and piezoresistive performance through the placement of limited amounts of CNTs in a polymer matrix. The algorithm is used to design a set of distributed CNT composite structures in which local volume fractions of CNT in a polymer matrix are allowed to vary. Euler-Bernoulli equations and finite element models were used to perform the mechanical and electrostatic analyses, and the necessary micromechanics models, objective functions, and related sensitivities were presented. The algorithm was applied to three different cases. In the first case 1D beam cross-sections were subjected to either prescribed twist or prescribed bending curvature. The cross-sections were optimized for stiffness, conductivity, and strain sensing. In the second case 2D plane-stress structures were optimized for stiffness and sensing. Plate with a hole and a compact tension samples were both investigated. In the third case the plate with a hole was optimized again, this time with a variable electrode. This was accomplished via the development and implementation of a continuous quadratic surrogate model, which interpolates performance across discrete nodal boundary conditions.

1. Optimization of Beam Cross-Sections.

    - For a beam in torsion, the optimal cross-section places stiff material such that it forms a circular cylinder, maximizing the GJ.
    - Without piezoresistive coupling, maximizing conductivity between electrodes results in the placement of highest CNT concentrations in a direct conductive path.
    - For a beam in torsion, the trade-off between optimizing both rigidity and conductivity results in a design that begins to deviate from the torsional circular cylinder to a structure that prefers more CNT in the conductive path. This trade-off was

seen to be nonlinear, with relatively high (80 % of max) amounts of conductivity for equally high rigidity, but with only 40 % of max conductivity for a design with the max attainable rigidity. Obtaining the last twenty percent of the mechanical stiffness is increasingly costly to the conductive performance.

- For a beam in bending, the stiffest cross-section places the highest concentration of CNT as far from the bending axis as possible. This corresponds with maximizing the effective EI of the structure. Relaxing the global volume fraction constraint directly led to increased stiffness, as adding material always increases local modulus. However, this effect is diminished as the locations far from the bending axis reach max allowable CNT. As bending rigidity scales with local modulus multiplied by distance from the bending axis, the addition of material close to the central axis, while still beneficial, is not as significant as adding it near the edge of the structure.
- For a beam in bending, the existence of both tension and compression in the cross-section complicates the optimization of the sensing performance. As it is necessary to form a conductive path between electrodes, some elements in the path may have different signs of strain than others, leading to a reduction in the strain sensing performance. This reduction can be minimized by placing the electrodes in a way that does not require formation of a conductive path across the bending axis, thus partially decoupling the sensing and stiffness performance. This helped to motivate the investigation of including the electrode location in the design process, which was later carried out in Chapter 6.
- In terms of maximized sensing in the bending cross-section, relaxing the global volume fraction constraint beyond 4 % showed no increase in performance, with the optimal cross-sections using between 3 and 4 percent CNT.
- The coupled stiffness and sensing problem was shown to have many local minima, and a Pareto-Based Restart Method in Section 3.2.1 was used to help better define the multiobjective optimal performance and associated topologies. This method was shown to be on the order of three times faster than using a pure random multi-start method with comparable number of starting conditions. It was also able to find better minima and provide a more well-defined Pareto Front for the presented test case.

2. Optimization of 2D Plane-Stress Structures.

   - For the plate with a hole case the stress concentrations around the hole result in highly contested local areas. The stiffness maximization seeks to place large amounts of CNT near the stress concentrations, and thus reduce the overall strain energy. The sensing maximization seeks to instead place highly piezoresistive elements in this region.
   - For the plate with a hole case, the stiffness maximization is relatively insensitive to topology changes in regions far from the hole, as the stress concentration

dominates the mechanical performance. There are diminishing returns in stiffness performance when relaxing the volume fraction constraint.

- For the plate with a hole case, the sensing maximization seeks to again remove competing tension/compression regions from the conductive path by placing high sensing (2 percent CNT) regions around the right side of the hole and relatively low sensing (low percent CNT) around the top side of the hole, reducing the effect of one of the regions on the sensing performance while boosting the other.
- Sensing is also influenced by manipulating the strain field via development of a cutout region in the right half of the topology. This feature does not develop when an optimization is performed without the coupled mechanics included. Including the coupling in the plate with a hole optimization results in a design that is over twice as good in sensing.
- Similar to the stiffness performance, sensing maximization experiences diminishing returns when relaxing the volume fraction constraint. As sensing is dominated by the location around the right edge of the hole, the optimal design does not require all available CNT to obtain the maximum sensing performance.
- For the compact tension case, the stiffness is maximized by connecting the notch tip to the pinholes via stiff CNT. The stiffness performance is dominated by the strain concentration at the notch tip. Similar to the plate with a hole case, away from this localized region of high strains the design is somewhat insensitive to changed in volume fraction.
- For the compact tension case, the sensing is maximized by placing highly piezoresistive elements at the notch and then using highly conductive elements to connect this region to the electrodes. The compact tension sensing results do not improve when relaxing the volume fraction constraint beyond 5%. Again, including coupling in the optimization leads to an improved sensing performance.

3. Simultaneous Optimization of Topology and Electrode.

    - A surrogate model was used to approximate the discrete nature of the boundary electrode location. The quadratic response surface (QRS) model was chosen, and was validated against nodal outputs of a refined mesh.
    - A trade study showed that the QRS surrogate model worked best with a second order optimization algorithm. While slower than the Interior-Point method, sequential quadratic programming (SQP) was able to obtain feasible designs that were overall better in sensing, and it was determined that the better objective outweighed the increased computational cost. SQP was chosen as the optimization routine for the simultaneous design of topology and electrode.
    - Across all three volume fraction constraints the designs that included the variable electrode dominated the fixed electrode counterparts, so long as the stiffness

epsilon-constraint was relaxed enough to allow for placement of piezoresistive material on the right side of the hole. Overall, designs with the electrode included improved maximum sensing performance by between sixty and ninety percent.

- With a variable electrode the optimal topology is allowed to place stiff material near the hole without forming sub-optimal conductive paths. This both helps satisfy intermediate stiffness epsilon-constraints and moves the effective electrode closer to the highly piezoresistive region. Additionally, the electrode restricted itself to only covering this highly piezoresistive region, forcing all of the current to flow through this area.

These results are the major takeaways from the research conducted on optimizing a CNT doped polymer structure for maximum mechanical, electrical, and peizoresistive performance. The development of the analysis models and sensitivity equations themselves may also be considered important outputs, for without them none of the optimization results would exist.

7.2 Extensions and Future Work

While the presented work establishes an algorithm for optimizing multifunctional composite structures and their associated boundary conditions, it could benefit from several further avenues of research.

First, extending the method to arbitrary three dimensional structures will add to the amount of realistic problems that can be solved via this optimization routine. While cross-sections and 2D structures are representative for a wide range of problems, one of the benefits of topology optimization as a whole is being able to arrive at complex designs not uncovered by conventional shape and sizing optimizations. The third dimension adds such complexity, and thus it is possible that the optimization will prove even more beneficial there.

Second, the research presented here assumes that the manufacturing method used to fabricate the optimized structures uses randomly oriented, well dispersed CNTs. In practice, depending on the manufacturing method used, this may not be the case. In fact, it may be desirable to control some measure of CNT bundle orientation as well as volume fraction. It may also be of interest to add more than one filler phase i.e. boron nitride nanospheres for added capability in thermal environments. Both the case of controlling fiber angle and adding additional phases increases the number of design variables per element, but it is a worthy consideration if there exist manufacturing methods that can actually control these properties. While the processes mentioned here are all controlled via design variables, it may also be of interest to do a processing-conscious design algorithm. This algorithm would implement finely tailored filtering methods to match the resolution of the topology features to the capabilities of the available processing methods. It may also include some form of

uncertainty in either the constraints, objectives, or design variables themselves.

Finally, another interesting extension would be to complete an experimental parallel of the presented work. No doubt this would be a large undertaking, as there are a myriad of obstacles to overcome in printing and testing one of these optimized structures. But the future of design, especially with topology optimization, is closely linked to additive manufacturing with advanced materials. Coupling this optimization method with a printing process for rapid design and testing of multifunctional composite structures is a logical progression from the theoretical to the tangible.

In any case, what exists in this dissertation is a strong jumping off point toward these options and many more. Structural requirements are evolving, and it is up to research like this to leap out away from conventional methods in materials and design and meet that evolution head on.

Bibliography

[1] N. Aage, E. Andreassen, B. S. Lazarov, and O. Sigmund, "Giga-voxel computational morphogenesis for structural design," *Nature*, vol. 550, no. 7674, pp. 84–86, Oct. 2017. [Online]. Available: http://www.nature.com/doifinder/10.1038/nature23911

[2] M. P. Bendse and O. Sigmund, *Topology Optimization*. Berlin, Heidelberg: Springer Berlin Heidelberg, 2004. [Online]. Available: http://link.springer.com/10.1007/978-3-662-05086-6

[3] S. Iijima, "Helical microtubules of graphitic carbon," *Nature*, vol. 354, no. 6348, p. 56, Nov 07 1991, copyright - Copyright Macmillan Journals Ltd. Nov 7, 1991; Last updated - 2017-10-31; CODEN - NATUAS. [Online]. Available: http://login.ezproxy.lib.vt.edu/login?url=https://search-proquest-com.ezproxy.lib.vt.edu/docview/204423867?accountid=14826

[4] "Single-shell carbon nanotubes of 1-nm diameter," *Nature*, vol. 363, no. 6430, p. 603, Jun 17 1993, copyright - Copyright Macmillan Journals Ltd. Jun 17, 1993; Last updated - 2017-10-31; CODEN - NATUAS. [Online]. Available: http://login.ezproxy.lib.vt.edu/login?url=https://search-proquest-com.ezproxy.lib.vt.edu/docview/204455055?accountid=14826

[5] M. Dresselhaus, G. Dresselhaus, and R. Saito, *Physics of carbon nanotubes*, 1995, vol. 33, no. 7, pp. 883 – 891, nanotubes. [Online]. Available: http://www.sciencedirect.com/science/article/pii/0008622395000178

[6] B. Yakobson, "Fullerene nanotubes: C1,000,000 and beyond," *American Scientist*, vol. 85, no. 4, p. 324, Nov 07 1997.

[7] J.-P. Salvetat-Delmotte and A. Rubio, "Mechanical properties of carbon nanotubes: a fiber digest for beginners," *Carbon*, vol. 40, no. 10, pp. 1729 – 1734, 2002, carbon Nanotubes:The Present State. [Online]. Available: http://www.sciencedirect.com/science/article/pii/S000862230200012X

[8] M. Terrones, "Science and technology of the twenty-first century: Synthesis, properties, and applications of carbon nanotubes," *Annual Review of Materials Research*, vol. 33,

p. 419, 2003, copyright - Copyright Annual Reviews, Inc. 2003; Last updated - 2014-05-26. [Online]. Available: http://login.ezproxy.lib.vt.edu/login?url=https://search-proquest-com.ezproxy.lib.vt.edu/docview/221137221?accountid=14826

[9] V. N. Popov, "Carbon nanotubes: properties and application," *Materials Science and Engineering: R: Reports*, vol. 43, no. 3, pp. 61 – 102, 2004. [Online]. Available: http://www.sciencedirect.com/science/article/pii/S0927796X03001268

[10] A. K. Chaurasia and G. D. Seidel, "Computational micromechanics analysis of electron-hopping-induced conductive paths and associated macroscale piezoresistive response in carbon nanotubepolymer nanocomposites," *Journal of Intelligent Material Systems and Structures*, vol. 25, no. 17, pp. 2141–2164, Nov. 2014. [Online]. Available: http://journals.sagepub.com/doi/10.1177/1045389X13517314

[11] Gang Yin, Ning Hu, Y. Karube, Yaolu Liu, Yuan Li, and H. Fukunaga, "A carbon nanotube/polymer strain sensor with linear and anti-symmetric piezoresistivity," *Journal of Composite Materials*, vol. 45, no. 12, pp. 1315–1323, Jun. 2011. [Online]. Available: http://journals.sagepub.com/doi/10.1177/0021998310393296

[12] Alamusi, N. Hu, H. Fukunaga, S. Atobe, Y. Liu, and J. Li, "Piezoresistive Strain Sensors Made from Carbon Nanotubes Based Polymer Nanocomposites," *Sensors*, vol. 11, no. 12, pp. 10 691–10 723, Nov. 2011. [Online]. Available: http://www.mdpi.com/1424-8220/11/11/10691/

[13] R. Haj-Ali, H. Zemer, R. El-Hajjar, and J. Aboudi, "Piezoresistive fiber-reinforced composites: A coupled nonlinear micromechanicalmicroelectrical modeling approach," *International Journal of Solids and Structures*, vol. 51, no. 2, pp. 491–503, Jan. 2014. [Online]. Available: http://linkinghub.elsevier.com/retrieve/pii/S0020768313004113

[14] W. Obitayo and T. Liu, "A Review: Carbon Nanotube-Based Piezoresistive Strain Sensors," *Journal of Sensors*, vol. 2012, pp. 1–15, 2012. [Online]. Available: http://www.hindawi.com/journals/js/2012/652438/

[15] W. A. Curtin and B. W. Sheldon, "CNT-reinforced ceramics and metals," *Materials Today*, vol. 7, no. 11, pp. 44–49, 2004.

[16] K. Chawla, "Ceramic matrix materials," in *Ceramic Matrix Composites*. Springer, 2003, pp. 11–46.

[17] S. Bakshi, D. Lahiri, and A. Agarwal, "Carbon nanotube reinforced metal matrix composites-a review," *International Materials Reviews*, vol. 55, no. 1, pp. 41–64, 2010.

[18] S. I. Cha, K. T. Kim, S. N. Arshad, C. B. Mo, and S. H. Hong, "Extraordinary strengthening effect of carbon nanotubes in metal-matrix nanocomposites processed by molecular-level mixing," *Advanced Materials*, vol. 17, no. 11, pp. 1377–1381, 2005.

[19] A. K. Chaurasia, E. C. Sengezer, K. K. Talamadupula, S. Povolny, and G. D. Seidel, "Experimental characterization and computational modeling of deformation and damage sensing through the piezoresistive response of nanocomposite bonded surrogate energetic materials," *Journal of Multifunctional Composites*, vol. 2, no. 4, 2014.

[20] E. Sengezer and G. D. Seidel, "Experimental characterization of damage evolution in carbon nanotube-polymer nanocomposites," in *56th AIAA/ASCE/AHS/ASC Structures, Structural Dynamics, and Materials Conference*, 2015, p. 0126.

[21] F. H. Gojny, J. Nastalczyk, Z. Roslaniec, and K. Schulte, "Surface modified multi-walled carbon nanotubes in cnt/epoxy-composites," *Chemical physics letters*, vol. 370, no. 5-6, pp. 820–824, 2003.

[22] M. H. G. Wichmann, S. T. Buschhorn, J. Gehrmann, and K. Schulte, "Piezoresistive response of epoxy composites with carbon nanoparticles under tensile load," *Physical Review B*, vol. 80, no. 24, Dec. 2009. [Online]. Available: https://link.aps.org/doi/10.1103/PhysRevB.80.245437

[23] H.-Z. Geng, K. K. Kim, and K. P. So, "Effect of acid treatment on carbon nanotube-based flexible transparent conducting films," *Journal of the American Chemical Society*, vol. 129, no. 25, pp. 7758–7759, 2007.

[24] S. J. Tans, A. R. Verschueren, and C. Dekker, "Room-temperature transistor based on a single carbon nanotube," *Nature*, vol. 393, no. 6680, p. 49, 1998.

[25] R. Khare, S. L. Mielke, J. T. Paci, S. Zhang, R. Ballarini, G. C. Schatz, and T. Belytschko, "Coupled quantum mechanical/molecular mechanical modeling of the fracture of defective carbon nanotubes and graphene sheets," *Physical Review B*, vol. 75, no. 7, p. 075412, 2007.

[26] Y. Han and J. Elliott, "Molecular dynamics simulations of the elastic properties of polymer/carbon nanotube composites," *Computational Materials Science*, vol. 39, no. 2, pp. 315–323, 2007.

[27] G. D. Seidel and D. C. Lagoudas, "Micromechanical analysis of the effective elastic properties of carbon nanotube reinforced composites," *Mechanics of Materials*, vol. 38, no. 8, pp. 884 – 907, 2006, advances in Disordered Materials. [Online]. Available: http://www.sciencedirect.com/science/article/pii/S0167663605001699

[28] D. C. Hammerand, G. D. Seidel, and D. C. Lagoudas, "Computational micromechanics of clustering and interphase effects in carbon nanotube composites," *Mechanics of Advanced Materials and Structures*, vol. 14, no. 4, pp. 277–294, 2007. [Online]. Available: https://doi.org/10.1080/15376490600817370

[29] K. Tserpes and P. Papanikos, "Finite element modeling of single-walled carbon nanotubes," *Composites Part B: Engineering*, vol. 36, no. 5, pp. 468–477, 2005.

[30] W. Voigt, "Ueber die beziehung zwischen den beiden elasticitätsconstanten isotroper körper," *Annalen der physik*, vol. 274, no. 12, pp. 573–587, 1889.

[31] A. Reuss, "Berechnung der fließgrenze von mischkristallen auf grund der plastizitätsbedingung für einkristalle." *ZAMM-Journal of Applied Mathematics and Mechanics/Zeitschrift für Angewandte Mathematik und Mechanik*, vol. 9, no. 1, pp. 49–58, 1929.

[32] Z. Hashin and S. Shtrikman, "A variational approach to the theory of the elastic behaviour of polycrystals," *Journal of the Mechanics and Physics of Solids*, vol. 10, no. 4, pp. 343–352, 1962.

[33] J. D. Eshelby, "The determination of the elastic field of an ellipsoidal inclusion, and related problems," in *Proc. R. Soc. Lond. A*, vol. 241, no. 1226. The Royal Society, 1957, pp. 376–396.

[34] J. Eshelby, "The elastic field outside an ellipsoidal inclusion," in *Proc. R. Soc. Lond. A*, vol. 252, no. 1271. The Royal Society, 1959, pp. 561–569.

[35] T. Mori and K. Tanaka, "Average stress in matrix and average elastic energy of materials with misfitting inclusions," *Acta metallurgica*, vol. 21, no. 5, pp. 571–574, 1973.

[36] J. Affdl and J. Kardos, "The halpin-tsai equations: a review," *Polymer Engineering & Science*, vol. 16, no. 5, pp. 344–352, 1976.

[37] Y. Benveniste, "A new approach to the application of mori-tanaka's theory in composite materials," *Mechanics of materials*, vol. 6, no. 2, pp. 147–157, 1987.

[38] M. Kim, F. Mirza, and J. Song, "Micromechanics modeling for the stiffness and strength properties of glass fibers/cnts/epoxy composites," *WIT Transactions on the Built Environment*, vol. 112, pp. 279–290, 2010.

[39] X. Ren and G. D. Seidel, "Computational micromechanics modeling of piezoresistivity in carbon nanotubepolymer nanocomposites," *Composite Interfaces*, vol. 20, no. 9, pp. 693–720, Dec. 2013. [Online]. Available: https://www.tandfonline.com/doi/full/10.1080/15685543.2013.813199

[40] M. P. Bendsøe and N. Kikuchi, "Generating optimal topologies in structural design using a homogenization method," *Computer methods in applied mechanics and engineering*, vol. 71, no. 2, pp. 197–224, 1988.

[41] J. Sokolowski and J.-P. Zolesio, "Introduction to shape optimization," in *Introduction to Shape Optimization*. Springer, 1992, pp. 5–12.

[42] P. W. Christensen and A. Klarbring, *An introduction to structural optimization*. Springer Science & Business Media, 2008, vol. 153.

[43] M. P. Bendsøe and O. Sigmund, "Material interpolation schemes in topology optimization," *Archive of applied mechanics*, vol. 69, no. 9-10, pp. 635–654, 1999.

[44] O. Sigmund and J. Petersson, "Numerical instabilities in topology optimization: a survey on procedures dealing with checkerboards, mesh-dependencies and local minima," *Structural optimization*, vol. 16, no. 1, pp. 68–75, 1998.

[45] T. Bruns, "A reevaluation of the simp method with filtering and an alternative formulation for solid–void topology optimization," *Structural and Multidisciplinary Optimization*, vol. 30, no. 6, pp. 428–436, 2005.

[46] L. Hurwicz, "Optimality criteria for decision making under ignorance," Cowles Commission Discussion Paper, Statistics, Tech. Rep., 1951.

[47] G. I. Rozvany, *Structural design via optimality criteria: the Prager approach to structural optimization*. Springer Science & Business Media, 2012, vol. 8.

[48] K. Svanberg, "The method of moving asymptotesa new method for structural optimization," *International Journal for Numerical Methods in Engineering*, vol. 24, no. 2, pp. 359–373, 1987. [Online]. Available: http://dx.doi.org/10.1002/nme.1620240207

[49] P. E. Gill and E. Wong, "Sequential quadratic programming methods," in *Mixed integer nonlinear programming*. Springer, 2012, pp. 147–224.

[50] J. Nocedal and S. J. Wright, *Sequential quadratic programming*. Springer, 2006.

[51] M. Zhou, Y. Shyy, and H. Thomas, "Checkerboard and minimum member size control in topology optimization," *Structural and Multidisciplinary Optimization*, vol. 21, no. 2, pp. 152–158, 2001.

[52] O. Sigmund, "A 99 line topology optimization code written in Matlab," *Structural and multidisciplinary optimization*, vol. 21, no. 2, pp. 120–127, 2001.

[53] E. Andreassen, A. Clausen, M. Schevenels, B. S. Lazarov, and O. Sigmund, "Efficient topology optimization in matlab using 88 lines of code," *Structural and Multidisciplinary Optimization*, vol. 43, no. 1, pp. 1–16, 2011.

[54] J. D. Deaton and R. V. Grandhi, "A survey of structural and multidisciplinary continuum topology optimization: post 2000," *Structural and Multidisciplinary Optimization*, vol. 49, no. 1, pp. 1–38, 2014.

[55] O. Sigmund and K. Maute, "Topology optimization approaches," *Structural and Multidisciplinary Optimization*, vol. 48, no. 6, pp. 1031–1055, 2013.

[56] G. Paulino, "Where are we in topology opimization," *10th World Congress on Structural and Multidisciplinary Optimization*, 2013.

[57] S. Torquato, S. Hyun, and A. Donev, "Optimal design of manufacturable three-dimensional composites with multifunctional characteristics," *Journal of Applied Physics*, vol. 94, no. 9, pp. 5748–5755, Nov. 2003. [Online]. Available: http://aip.scitation.org/doi/10.1063/1.1611631

[58] B. Stanford, P. Beran, and M. Kobayashi, "Aeroelastic Optimization of Flapping Wing Venation: a Cellular Division Approach." American Institute of Aeronautics and Astronautics, Apr. 2011. [Online]. Available: http://arc.aiaa.org/doi/10.2514/6.2011-2094

[59] N. de Kruijf, S. Zhou, Q. Li, and Y.-W. Mai, "Topological design of structures and composite materials with multiobjectives," *International Journal of Solids and Structures*, vol. 44, no. 22-23, pp. 7092–7109, Nov. 2007. [Online]. Available: http://linkinghub.elsevier.com/retrieve/pii/S0020768307001825

[60] K. Maute, A. Tkachuk, J. Wu, H. J. Qi, Z. Ding, and M. L. Dunn, "Level set topology optimization of printed active composites," *Journal of Mechanical Design*, vol. 137, no. 11, p. 111402, 2015.

[61] T. Zegard and G. H. Paulino, "Bridging topology optimization and additive manufacturing," *Structural and Multidisciplinary Optimization*, vol. 53, no. 1, pp. 175–192, 2016.

[62] W. M. Rubio, E. C. N. Silva, and S. Nishiwaki, "Piezoresistive sensor design using topology optimization," *Structural and Multidisciplinary Optimization*, vol. 36, no. 6, pp. 571–583, Nov. 2008. [Online]. Available: http://link.springer.com/10.1007/s00158-007-0191-6

[63] S. Giusti, L. Mello, and E. Silva, "Piezoresistive device optimization using topological derivative concepts," *Structural and Multidisciplinary Optimization*, vol. 50, no. 3, pp. 453–464, 2014.

[64] M. P. Bendsøe and O. Sigmund, *Optimization of structural topology, shape, and material*. Springer, 1995, vol. 414.

[65] G. Marck, M. Nemer, J.-L. Harion, S. Russeil, and D. Bougeard, "Topology optimization using the simp method for multiobjective conductive problems," *Numerical Heat Transfer, Part B: Fundamentals*, vol. 61, no. 6, pp. 439–470, 2012.

[66] H. Maurer and J. Zowe, "First and second-order necessary and sufficient optimality conditions for infinite-dimensional programming problems," *Mathematical Programming*, vol. 16, no. 1, pp. 98–110, 1979.

[67] D. P. Bertsekas, *Nonlinear programming*. Athena scientific Belmont, 1999.

[68] A. Diaz and O. Sigmund, "Checkerboard patterns in layout optimization," *Structural optimization*, vol. 10, no. 1, pp. 40–45, 1995.

[69] R. B. Haber, C. S. Jog, and M. Bendsøe, "Variable-topology shape optimization with a control on perimeter," *Advances in design automation*, vol. 69, no. 2, 1994.

[70] C. Jog, "A robust dual algorithm for topology design of structures in discrete variables," *International Journal for Numerical Methods in Engineering*, vol. 50, no. 7, pp. 1607–1618, 2001.

[71] D. Brackett, I. Ashcroft, and R. Hague, "Topology optimization for additive manufacturing," in *Proceedings of the solid freeform fabrication symposium, Austin, TX*, vol. 1. S, 2011, pp. 348–362.

[72] K. Svanberg and H. Svärd, "Density filters for topology optimization based on the pythagorean means," *Structural and Multidisciplinary Optimization*, vol. 48, no. 5, pp. 859–875, 2013.

[73] J. K. Guest, J. H. Prévost, and T. Belytschko, "Achieving minimum length scale in topology optimization using nodal design variables and projection functions," *International journal for numerical methods in engineering*, vol. 61, no. 2, pp. 238–254, 2004.

[74] S. Xu, Y. Cai, and G. Cheng, "Volume preserving nonlinear density filter based on heaviside functions," *Structural and Multidisciplinary Optimization*, vol. 41, no. 4, pp. 495–505, 2010.

[75] O. Sigmund, "Morphology-based black and white filters for topology optimization," *Structural and Multidisciplinary Optimization*, vol. 33, no. 4-5, pp. 401–424, 2007.

[76] C.-L. Hwang and A. S. M. Masud, "Methods for multiple objective decision making," in *Multiple Objective Decision MakingMethods and Applications*. Springer, 1979, pp. 21–283.

[77] M. Ehrgott and X. Gandibleux, "A survey and annotated bibliography of multiobjective combinatorial optimization," *OR-Spektrum*, vol. 22, no. 4, pp. 425–460, 2000.

[78] A. Oskouyi, U. Sundararaj, and P. Mertiny, "Tunneling Conductivity and Piezoresistivity of Composites Containing Randomly Dispersed Conductive Nano-Platelets," *Materials*, vol. 7, no. 12, pp. 2501–2521, Mar. 2014. [Online]. Available: http://www.mdpi.com/1996-1944/7/4/2501

[79] W. Bauhofer and J. Z. Kovacs, "A review and analysis of electrical percolation in carbon nanotube polymer composites," *Composites Science and Technology*, vol. 69, no. 10, pp. 1486–1498, 2009.

[80] G. Keulemans, F. Ceyssens, M. De Volder, J. W. Seo, and R. Puers, "Fabrication and characterisation of carbon nanotube composites for strain sensor applications," in *Proceedings of the 21st Micromechanics and Micro systems Europe Workshop*, vol. 21, 2010, pp. 231–234.

[81] J. Sandler, J. Kirk, I. Kinloch, M. Shaffer, and A. Windle, "Ultra-low electrical percolation threshold in carbon-nanotube-epoxy composites," *Polymer*, vol. 44, no. 19, pp. 5893–5899, 2003.

[82] R. Schueler, J. Petermann, K. Schulte, and H.-P. Wentzel, "Agglomeration and electrical percolation behavior of carbon black dispersed in epoxy resin," *Journal of Applied Polymer Science*, vol. 63, no. 13, pp. 1741–1746, 1997.

[83] Y. Y. Kim and T. S. Kim, "Topology optimization of beam cross sections," *International Journal of Solids and Structures*, vol. 37, no. 3, pp. 477–493, 2000.

[84] T. S. Kim and Y. Y. Kim, "Multiobjective Topology Optimization of a Beam Under Torsion and Distortion," *AIAA Journal*, vol. 40, no. 2, pp. 376–381, Feb. 2002. [Online]. Available: http://arc.aiaa.org/doi/10.2514/2.1656

[85] J. L. Krahula and G. F. Lauterbach, "A finite element solution for Saint-Venant torsion," *AIAA Journal*, vol. 7, no. 12, pp. 2200–2203, Dec. 1969. [Online]. Available: http://arc.aiaa.org/doi/10.2514/3.5516

[86] J.-M. Jin, *The finite element method in electromagnetics*. John Wiley & Sons, 2015.

[87] R. S. Barsoum and R. H. Gallagher, "Finite element analysis of torsional and torsional–flexural stability problems," *International Journal for Numerical Methods in Engineering*, vol. 2, no. 3, pp. 335–352, 1970.

[88] J. Xiao, Y. Li, and W. Fan, "A laminate theory of piezoresistance for composite laminates," *Composites science and technology*, vol. 59, no. 9, pp. 1369–1373, 1999.

[89] L. Q. Cortes, S. Racagel, A. Lonjon, E. Dantras, and C. Lacabanne, "Electrically conductive carbon fiber / PEKK / silver nanowires multifunctional composites," *Composites Science and Technology*, vol. 137, pp. 159–166, Dec. 2016. [Online]. Available: http://linkinghub.elsevier.com/retrieve/pii/S0266353816307680

[90] N. Hansen and G. Hansen, "From inception to insertion: successful products and applications using nickel nanostrands," *SAMPE Journal*, vol. 47, no. 3, pp. 6–13, 2011.

[91] I. Y. Kim and O. L. de Weck, "Adaptive weighted-sum method for bi-objective optimization: Pareto front generation," *Structural and multidisciplinary optimization*, vol. 29, no. 2, pp. 149–158, 2005.

[92] M. D. Center, "Optimization toolbox, constrained optimization, fmincon." [Online]. Available: https://www.mathworks.com/help/optim/ug/choosing-the-algorithm.html

[93] J. Zhu, H. Peng, F. Rodriguez-Macias, J. L. Margrave, V. N. Khabashesku, A. M. Imam, K. Lozano, and E. V. Barrera, "Reinforcing epoxy polymer composites through covalent integration of functionalized nanotubes," *Advanced Functional Materials*, vol. 14, no. 7, pp. 643–648, 2004.

[94] G. Mavrotas, "Effective implementation of the ε-constraint method in multi-objective mathematical programming problems," *Applied mathematics and computation*, vol. 213, no. 2, pp. 455–465, 2009.

[95] M. Negahban, "Hookes law and volumetric strain for plane stress," 2018. [Online]. Available: http://emweb.unl.edu/NEGAHBAN/Em325/17-Hooke's-law-for-plane-stress/Hooke's%20law%20for%20plane%20stress.htm

[96] E. Fundamentals, "Hookes law for plane stress," 2018. [Online]. Available: http://www.efunda.com/formulae/solid_mechanics/mat_mechanics/hooke_plane_stress.cfm

[97] P. I. Kattan, *MATLAB guide to finite elements: an interactive approach*, 2nd ed. Berlin ; New York: Springer, 2007.

[98] "14: The plane stress problem," accessed: 2018-03-13. [Online]. Available: https://www.colorado.edu/engineering/CAS/courses.d/IFEM.d/IFEM.Ch14.d

[99] J. R. R. A. Martins and J. T. Hwang, "Review and Unification of Methods for Computing Derivatives of Multidisciplinary Computational Models," *AIAA Journal*, vol. 51, no. 11, pp. 2582–2599, Nov. 2013. [Online]. Available: http://arc.aiaa.org/doi/10.2514/1.J052184

[100] R. Lazimy, "Mixed-integer quadratic programming," *Mathematical Programming*, vol. 22, no. 1, pp. 332–349, 1982.

[101] M. R. Bussieck and A. Pruessner, "Mixed-integer nonlinear programming," *SIAG/OPT Newsletter: Views & News*, vol. 14, no. 1, pp. 19–22, 2003.

[102] I. E. Grossmann, "Review of nonlinear mixed-integer and disjunctive programming techniques," *Optimization and engineering*, vol. 3, no. 3, pp. 227–252, 2002.

[103] L. P. Swiler, *Surrogate Models for Mixed Discrete-Continuous Variables*. Springer International Publishing, 2014, pp. 181–202.

[104] G. B. Dantzig, "Linear programming and extensions. princeton landmarks in mathematics and physics," 1963.

[105] F. Palacios-Gomez, L. Lasdon, and M. Engquist, "Nonlinear optimization by successive linear programming," *Management science*, vol. 28, no. 10, pp. 1106–1120, 1982.

[106] "Slp-trust," 2017. [Online]. Available: https://www.mathworks.com/matlabcentral/fileexchange/53331-slp-trust-sqp

[107] S. J. Wright, *Primal-dual interior-point methods*. Siam, 1997, vol. 54.

[108] F. A. Potra and S. J. Wright, "Interior point methods," *Journal of Computational and Applied Mathematics*, vol. 124, no. 1-2, pp. 281–302, 2000.

[109] C. G. Broyden, "The convergence of a class of double-rank minimization algorithms," *IMA Journal of Applied Mathematics*, vol. 6, no. 1, pp. 76–90, 1970.

[110] D. C. Liu and J. Nocedal, "On the limited memory bfgs method for large scale optimization," *Mathematical programming*, vol. 45, no. 1-3, pp. 503–528, 1989.

Appendix A

Additional Surrogate Model Trade Studies

The quadratic surrogate model from Chapter 6 was subjected to several trade studies in order to validate its ability to represent the electrostatic boundary condition between nodes. Two finite element meshes were used in the validation study, both modeling the same quadrant of the plate with hole structure from Section 5.3.1. Analysis was first performed on a coarse mesh where the boundary condition location is set to a non-integer, requiring the surrogate model to approximate the performance. The negative electrode is fixed along the length of the right vertical edge, but the start and end points of the positive electrode are varied along the inner curved edge. The trade steps through electrode placements of the coarse mesh at half-element intervals, requiring the surrogate model to interpolate the sensing performance. The variable electrode is bound by element locations $\boldsymbol{b}_{cs} = [1.5 + s, N_c - (s + .5)]$ where N_c is the number of elements along the inner curved edge and the subscript c denotes coarse mesh, and s is an integer counter that indexes the electrode location. As s increases, the edges of the electrode move closer together.

A fine mesh with twice the number of elements along the positive electrode edge is then evaluated at integer electrode values that correspond to the non-integer locations of the coarse mesh. This formulation is convenient in that the maximum deviation from a physical electrode in the coarse mesh case, and thus the location of the continuous electrode that will rely most heavily on the surrogate model, falls directly on a node in the fine mesh case. The positive electrode in the fine mesh is bound by $\boldsymbol{b}_{fs} = [3 + 2s, N_f - 1 - 2s]$.

The same vertical load along the top edge, $F_{mag} = 200$, is applied to all test cases. For this trade $N_c = 16$ and $N_f = 2N_c = 32$. The electrode length parameter is bound by $1 \leq s \leq 6$ to ensure the positive electrode does not close below 2 element lengths, which would result in a 0 length electrode length during the surrogate model formulation.

The results of the trade are shown below in table A for a uniform CNT distribution of 5%

Table A.1: Comparing coarse mesh w/ surrogate model to fine mesh at integer b values, centered electrode. All elements 5% CNT.

Electrode Length (% of edge)	**Coarse b**	**Coarse Mesh Objective**	**Fine b**	**Fine Mesh Objective**
75.00	[2.5,14.5]	-3.536	[5,29]	-3.529
62.50	[3.5,13.5]	-3.534	[7,27]	-3.512
50.00	[4.5,12.5]	-3.530	[9,25]	-3.498
37.50	[5.5,11.5]	-3.520	[11,23]	-3.470
25.00	[6.5,10.5]	-3.504	[13,21]	-3.439
12.50	[7.5,9.5]	-3.492	[15,19]	-3.393

Table A.2: Comparing coarse mesh w/ surrogate model to fine mesh at integer b values, centered electrode. All elements 5% CNT.

Electrode Length (% of edge)	**Coarse b**	**Coarse Mesh Objective**	**Fine b**	**Fine Mesh Objective**
75.00	[2.5,14.5]	-7.794	[5,29]	-7.779
62.50	[3.5,13.5]	-7.789	[7,27]	-7.753
50.00	[4.5,12.5]	-7.804	[9,25]	-7.705
37.50	[5.5,11.5]	-7.758	[11,23]	-7.649
25.00	[6.5,10.5]	-7.723	[13,21]	-7.581
12.50	[7.5,9.5]	-7.698	[15,19]	-7.480

CNT.

These results reflect the trend shown in Figure 6.1. The surrogate model is capturing the relative change in performance as the electrode moves between elements in the coarse mesh. Again, due to the differences in the finite element mesh, it is not expected that the objective values match exactly between coarse and fine meshes. But it is expected, and observed, that the changes in performance versus the location of the electrode follow similar trends for both meshes.

This trade is repeated with all elements being highly piezoresistive (2% CNT) and the results are shown in table A. As it was seen that the optimal designs for the fixed electrode contained at least some regions of 2% CNT around the inner edge, it is important to validate the surrogate model for this highly piezoresistive volume fraction.

Again, the surrogate model captures the change in performance. As a final test, the electrode is traded in a different manner. In this second trade b_1 is fixed and b_2 is decreased, i.e $\boldsymbol{b}_{cs} = [2.5, N_c - (s + .5)]$ and $\boldsymbol{b}_{fs} = [5, N_f - 1 - 2s]$. Physically, this means the bottom right end of the electrode is fixed at a lower bound, and the top left end of the electrode sweeps clockwise down the curved edge.

The above tables are regenerated for this case, and are shown in table A for a uniform

Table A.3: Comparing coarse mesh w/ surrogate model to fine mesh at integer b values, fixed b1. All elements 5% CNT.

Electrode Length (% of edge)	**Coarse b**	**Coarse Mesh Objective**	**Fine b**	**Fine Mesh Objective**
75.00	[2.5,14.5]	-3.536	[5,29]	-3.529
68.75	[2.5,13.5]	-3.549	[5,27]	-3.544
62.50	[2.5,12.5]	-3.578	[5,25]	-3.575
56.25	[2.5,11.5]	-3.633	[5,23]	-3.632
50.00	[2.5,10.5]	-3.716	[5,21]	-3.722
43.75	[2.5,9.5]	-3.831	[5,19]	-3.847
37.50	[2.5,8.5]	-3.984	[5,17]	-4.012
31.25	[2.5,7.5]	-4.185	[5,15]	-4.220
25.00	[2.5,6.5]	-4.418	[5,13]	-4.467
18.75	[2.5,5.5]	-4.693	[5,11]	-4.766
12.50	[2.5,4.5]	-5.024	[5,9]	-5.129

distribution of 5% CNT and in table A for a uniform distribution of 2% CNT.

The surrogate model is able to capture changes in sensing performance for different topologies and different combinations of the boundary electrode variable, validating its use in the simultaneous optimization of Chapter 6.

Table A.4: Comparing coarse mesh w/ surrogate model to fine mesh at integer b values, fixed b1. All elements 2% CNT.

Electrode Length (% of edge)	**Coarse b**	**Coarse Mesh Objective**	**Fine b**	**Fine Mesh Objective**
75.00	[2.5,14.5]	-7.794	[5,29]	-7.779
68.75	[2.5,13.5]	-7.821	[5,27]	-7.810
62.50	[2.5,12.5]	-7.887	[5,25]	-7.880
56.25	[2.5,11.5]	-8.005	[5,23]	-8.007
50.00	[2.5,10.5]	-8.190	[5,21]	-8.204
43.75	[2.5,9.5]	-8.446	[5,19]	-8.480
37.50	[2.5,8.5]	-8.784	[5,17]	-8.846
31.25	[2.5,7.5]	-9.228	[5,15]	-9.306
25.00	[2.5,6.5]	-9.743	[5,13]	-9.852
18.75	[2.5,5.5]	-10.352	[5,11]	-10.511
12.50	[2.5,4.5]	-11.082	[5,9]	-11.313